IMAGE RETRIEVAL IN ASTRONOMICAL INTERFEROMETERS AFFECTED BY ATMOSPHERIC TURBULENCE

A Thesis
Submitted for the Degree of

Doctor of Philosophy (Technology)

Submitted by

ARUN SURYA

Department of Applied Optics and Photonics
University College of Technology
University of Calcutta

June, 2015

Abstract

Single aperture speckle interferometry (Labeyrie, 1970) is a method that deciphers diffraction limited spatial Fourier spectrum and image features of stellar objects by counteracting blurring effect caused by the atmospheric turbulence. Together with pupil-plane techniques, as well as hybrid methods (speckle techniques with non- redundant pupils), it has made impacts in several important fields in astrophysics. The field of research that has benefited the most from such high angular resolution techniques and will still benefit in the future, is the origin and evolution of stellar systems. However, classical speckle interferometry falls short of obtaining phase information of the object, but provides a second-order moment (power spectrum) analysis which is the modulus of the object Fourier transform. Triple Correlation technique and other advanced image retrieval methods has been developed which also allows the reconstruction of the phase information. Such algorithmic techniques allows to retrieve diffraction limited information from the short exposure images. The thesis discusses the development of two image reconstruction algorithms based on triple correlation to be used with direct images from optical interferometers. Direct bispectrum algorithm uses a computationally intensive yet efficient triple correlation technique to reconstruct object information from two dimensional speckle images. Tomographic speckle masking algorithm has been developed to offer a computationally efficient method to reconstruct images from speckle data. It uses one dimensional projections and Radon transform to gain considerable savings in computational time and memory. Both these algorithms were tested with numerical simulations, real data and experimental simulations. Numerical simulations of different optical interferometric techniques was built to understand the possibility of reconstruction using these methods in multi-aperture optical interferometry. In the simulations the advantages of the all-in-one beam combination is over the use of pair-wise combination was also analyzed. We layout a study of the signal advantage we obtain at low light levels through all-in-one beam

combination in cophased and non-cophased speckle mode. The usability of these algorithms with diluted aperture interferometers which use pupil densification (Hypertelescopes) is also explored in this thesis. It is seen from the numerical simulations of image recontructions that the developed algorithms can be used to restore atmospherically degraded images from hypertelescopes with good signal to noise ratio.

Contents

1 Introduction **1**

1.1 History of high resolution imaging. 1

1.2 Basics of Optical Interferometry 5

1.2.1 A simple model for a two telescope interferometer . . . 5

1.2.2 Coherence Function 7

1.2.3 Visibility and Van Cittert–Zernike theorem 8

1.3 Speckle Masking and Speckle Interferometry 9

1.4 Long Baseline Optical Interferometers 12

1.5 Hypertelescope 12

1.6 Motivation 14

1.7 Thesis Overview 15

2 Numerical Simulation of Optical Interferometers **18**

2.1 Importance of phase in signals 18

2.2 Atmospheric phase variations 19

2.2.1 Kolmogorov Turbulence Model 20

2.2.2 Fried's Parameter 21

2.2.3 Simulating Kolmogorov Phase Screen 22

2.3 Earth Rotation Aperture Synthesis 24

2.4 Simulation of techniques in optical interferometry 26

2.4.1 Aperture masking over single aperture telescope 26

2.4.2 Multi-speckle images from long baseline interferometry 27

2.4.2.1 Steps in the simulation of multi-speckles . . . 29

2.4.3 Diluted Aperture Interferometers 29

2.4.4 Different types of beam combinations 30
2.4.4.1 Fizeau beam combination 30
2.4.4.2 Hypertelescope beam combination 31
2.4.4.3 IRAN 32
2.4.5 Comparison of all-in-one and pair-wise beam combination 33
2.4.5.1 One dimensional simulations for non-redundant apertures for cophased beam combinations . . 34
2.4.5.2 Two dimensional simulations of turbulence degraded images 37
2.5 Conclusions 41

3 Triple Correlation Algorithm 43
3.1 Introduction 43
3.2 Speckle interferometry 44
3.2.1 What is a Speckle? 44
3.2.2 Double Correlation and Power Spectrum 44
3.2.3 Stellar speckle interferometry 45
3.3 Triple Correlation 46
3.3.1 Basic Properties of Triple Correlation 47
3.3.2 Limitations of signal retrieval from triple correlation . . 49
3.3.3 The generalized speckle masking transfer function . . . 50
3.4 Image reconstruction from Bispectrum 51
3.4.1 Theory 51
3.4.2 Direct Bispectrum Algorithm 53
3.5 Results 54
3.5.1 Results with real images 54
3.5.2 Results with Aperture Masking Simulations 55
3.5.3 Results with Multispeckle Simulations 58
3.6 Conclusions 60

4 Tomographic Speckle Masking 61
4.1 Introduction 61

4.2 Radon Transform 62
4.2.1 Properties of Radon Transform 63
4.2.2 Inverse Radon Transform 63
4.2.2.1 Filtered Back Projection 64
4.3 Tomographic Speckle Masking Algorithm 64
4.4 Numerical Simulations 67
4.5 Laboratory Simulations 70
4.6 Results with Real Speckle Images 71
4.7 Conclusions 72

5 Speckle Imaging with Hypertelescopes 74
5.1 Introduction 74
5.2 76
5.2.1 Aperture Configuration 79
5.2.2 Speckle Imaging Algorithms 80
5.2.3 Earth Rotation Aperture Synthesis 81
5.3 Results 82
5.3.1 Reconstruction results with sextuple star and extended objects 82
5.3.2 Improvement of Reconstruction with Aperture Rotation 83
5.3.3 Limiting Magnitude 86
5.4 Simulation of imaging science targets with hypertelescope . . . 90
5.4.1 Simulation of imaging Active Galactic Nuclei 90
5.4.2 Imaging exoplanet transits with Hypertelescope 91
5.4.3 Binary Stars and Small Clusters 93
5.5 Conclusions 95

6 Summary and Future Work 96
6.1 Introduction 96
6.2 Summary 97
6.3 Future Prospects 98

6.3.1 Bispectrum algorithm to work on OIFITS data from long baseline interferometers. 98
6.3.2 Laboratory simulations of pupil densification 99
6.3.3 The 57m Hypertelescope in La Moutière 100
6.3.4 The Extremely Large Hypertelescope 102
6.4 Conclusion 102

Publications **105**

Bibliography **118**

List of Figures

1.1 Layout of Michelson Stellar Interferometer. M1, M2, M3 and M4 are mirrors used to form the periscopic arrangement (image courtesy: A. Labeyrie). 3

1.2 I2T Interferometer (Labeyrie et al. 2006). 4

1.3 GI2T Interferometer in Calern (Labeyrie et al. 2006). 4

1.4 A basic model of a two telescope interferometer. The plane wavefronts from the star are incident on the two apertures, A_1 and A_2. The path lengths are adjusted using delaylines, d_1 and d_2, for the beams to coherently combine to form an interference pattern. 6

1.5 The power measured at the detector of the 2 telescope interferometer as a function of optical delay. 8

1.6 The fringes of a point source (blue) and an extended source (red dotted) 9

1.7 Atmospheric degradation in astronomical imaging. a) The phase perturbations across a single aperture telescope. b) The short exposure speckle PSF. c) The ideal diffraction limited PSF. d) The long exposure PSF which is the average of several short exposure PSF. 11

1.8 Layout of a hypertelescope showing the different parts. 13

2.1 Example demonstrating importance of phase in signals 19

2.2 A speckle image (Saha, 1999) 20

2.3 The multilayer model of turbulence used in the simulations. . 23

2.4 Earth Rotation Aperture Synthesis as simulated by the developed software. (Top) The 3 mirror aperture used in the simulation. (Middle and Bottom) Aperture synthesis with different latitudes, source declinations and hours of observation. 25
2.5 A simulated aperture mask with 4 sub-pupils 27
2.6 The simulated multi speckle images with different configurations of large telescope interferometers. (Top) The two telescope aperture configuration similar to LBT and the corresponding multi-speckle image. (Middle) 3 telescope aperture configuration and multi-speckle image. (Bottom) 4 telescope aperture configuration similar to VLTI and the corresponding multi-speckle image. 28
2.7 Layout of Fizeau beam combination and corresponding PSF . 31
2.8 Layout of hypertelescope beam combination and corresponding PSF. The beam combination scheme uses small inverted Galilean telescopes in the exit pupil to densify the input pupil. 32
2.9 Layout of IRAN beam combination and corresponding PSF. The beam combination is done in this case in the image plane. 33
2.10 Three delta functions with non redundant baselines used as the aperture. 34
2.11 Visibity comparison 3 subapertures. (Top) The visibility of the all-in-one combination. The ratio (central-peak/secondary-peak) = n = 3. (Bottom) The visibility of combined pairwise combination, ie visibilities of each pair in aperture added together. The ratio (central-peak/secondary-peak) = n(n-1) = 6. 35
2.12 Four delta functions with non redundant baselines used as the aperture. 35

2.13 Visibility comparison for 4 subapertures. (Top) The visibility of the all-in-one combination. The ratio (central-peak/secondary-peak) = n = 4. (Bottom) The visibility of combined pairwise combination, ie visibilities of each pair in aperture added together. The ratio (central-peak/secondary-peak) = n(n-1) = 12. 36
2.14 Standard deviation of visibility amplitude ratio calculated for 24 photon events per mirror. 37
2.15 Standard deviation of visibility amplitude ratio calculated for 240 photon events per mirror 38
2.16 Standard deviation of visibility amplitude ratio calculated for 2400 photon events per mirror 38
2.17 The point spread functions for all-in-one and pair-wise combination in cophased and non-phased cases. a) all-in-one cophased PSF b) pair-wise- combined cophased PSF c) all-in-one turbulence PSF d) pair-wise combined turbulence PSF. 39
2.18 The speckle image of binary star: a) all-in-one snapshot image from array of 20 sub apertures with different atmospheric piston errors and b) image from co-addding pairwise fringe systems from the same array. The pair wise fringes were recorded same time across a single phase screen. 40
2.19 Autocorrelation of Binary Star with speckle interferometry: a) from all-in-one speckle images and b) from the co-added pairwise-speckle-frames. 41

3.1 Speckle images (above) and corresponding spatial power spectra (below). From left to right, Betelgeuse (resolved disk), Capella (resolved binary) and an unresolved reference star. The power spectra are each the sums of about 250 frames (Labeyrie, 1970). 46

3.2 Speckle interferometry reconstruction simulation of a binary star. The images are autocorrelations of the binary stars retrieved from speckle images from a 17 and 50 mirror array with and without earth rotation aperture synthesis. a) Binary star autocorrelation retrieved from speckles images of 17 mirror array, b) binary star autocorrelation retrieved from speckles images of 17 mirror array with aperture rotation of 8 hours, c) binary autocorrelation retrieved from speckles images of 50 mirror array and d) binary star autocorrelation retrieved from speckles images of 50 mirror array with aperture rotation of 8 hours. 47

3.3 (Left) One dimensional binary star object, (Center) corresponding 2-dimensional bispectrum, (Right) corresponding triple correlation. 49

3.4 (Left) One dimensional extended binary star object, (Center) corresponding 2-dimensional bispectrum, (Right) corresponding triple correlation. 49

3.5 Reconstruction from speckle images of β Coronae Borealis (HR5747): a) one of the speckle images of HR5747, b) the reconstructed image using direct bispectrum algorithm (Surya and Saha, 2014). 55

3.6 The aperture used for the simulation 56

3.7 Speckle Reconstruction using direct bispectrum from simulations of 17-hole aperture masking: a) binary star, b) six star group. 57

3.8 Speckle Reconstruction using direct bispectrum from simulations of 17-hole aperture masking using images taken at equal intervals through the night over 8 hrs: a) binary star. b) six star group. 58

3.9 Multi-speckle reconstruction of binary star: a) cophased image of binary star with single aperture, b) reconstructed image of binary star from speckles images from single aperture, c) cophased image of binary star averaged by earth rotation synthesis in a 2 telescope interferometer, d) reconstructed image of binary star from multi speckles of the same two telescope interferometer using earth rotation. 59

3.10 Multi-speckle reconstruction using direct bispectrum algorithm: (Left) the multispeckle image from a 2-telescope interferometer, (Sidebox Top) the ideal image as obtained by aperture rotation of two telescope interferometer through 8 hrs with out considering atmospheric turbulence, (Sidebox Bottom) the reconstructed image from the multi-speckle images of the 2-telescope interferometer taken at different times during 8 hrs. . 59

4.1 An image function and the projection at an angle. $f(x, y)$ is two dimensional image in the $x - y$ plane. $R(x', \theta)$ is one of the projections in the Radon transform at angle θ. 62

4.2 Process of Radon transform and inverse Radon transform of a 2 dimensional image. (Bottom) The inverse Radon transformed images from different number of projections [18, 36, 90]. . . . 65

4.3 A two dimensionsl speckle image and its sample one dimensional projections obtained at different angles using Radon Transform. 66

4.4 The image recovery results from the tomographic speckle imaging algorithm of a 6 star group using a 17 hole aperture mask: The aperture consists of randomly arranged 10 cm holes inside 1 m radius disk, a) the 6 star object distribution used in the simulation with the corresponding brightness ratio, b) The cophased image from the aperture masked mirror, c) The simulated speckle image of the object by imaging through turbulence, d) The recovered image using Direct Bispectrum with 100 frames, e) The recovered image using tomographic speckle masking from 18 projections with 100 frame and f) the recovered image using tomographic speckle masking from 180 projections with 100 frames. 68

4.5 The image recovery results from the tomographic speckle imaging algorithm of an extended planet object group using a 17 hole aperture mask: The aperture consists of randomly arranged 10 cm holes inside 1 m radius disk, a) the 6 star object distribution used in the simulation with the corresponding brightness ratio, b) The cophased image from the aperture masked mirror, c) The simulated speckle image of the object by imaging through turbulence, d) The recovered image using Direct Bispectrum with 100 frames, e) The recovered image using tomographic speckle masking from 18 projections with 100 frames and f) the recovered image using tomographic speckle masking from 180 projections with 100 frames. 69

4.6 Laboratory setup for simulation of aperture masking in presence of atmospheric turbulence. Laser source is collimated using a lens, and the collimated beam passes through the phase screen and aperture mask of 20 random holes. The beam then passes through an imaging lens to form a speckle image in the detector. 71

4.7 Reconstruction from laboratory simulations of speckle imaging: a) image of the artificial binary star from the experiment with out using turbulence phase screen, b) speckle image of binary star imaged with a Kolmogrov phase screen in laboratory and c) reconstructed image from tomographic speckle masking from 100 speckle frames. 71

4.8 Tomographic image reconstruction of speckle images of β Coronae Borealis (HR5747): a) one of the speckle images of HR5747, b) the bispectrum of a one dimensional projection of the speckle image and c) the reconstructed image using TSM Algorithm. . 72

5.1 Random phase screen across the 17 mirror aperture used for the simulations, following a Kolmogorov distribution. The dots indicate positions of the subapertures in the fully diluted array. 77

5.2 The object distributions used in the simulations (first column) along with their corresponding speckle frames (second column) as imaged by the 17 mirror array: a) six star group b) ten star group c) extended object. Speckle frames in average have 10000 photon events per each exposure. 78

5.3 Pupil densification of the aperture configuration used in the simulations. a) The input pupil of a diluted random 17 mirror array. b) The exit pupil after densification 80

5.4 Speckle imaging results for a six star cluster from turbulence degraded interferograms from a) 17 mirror aperture without aperture rotation, b) 17 mirror aperture with rotation through the night for 8 hrs, c) 50 mirror aperture without rotation and d) 50 mirror aperture with aperture rotation through night for 8 hrs. Each simulated exposure on average had 10,000 photon events. 84

5.5 Speckle imaging results for an extended object from turbulence degraded interferograms from a) 17 mirror aperture without aperture rotation, b) 17 mirror aperture with rotation through the night for 8 hrs, c) 50 mirror aperture without rotation and d) 50 mirror aperture with aperture rotation through night for 8 hrs. Each simulated exposure on average had 10,000 photon events. 85

5.6 Improvement of reconstructed image of star cluster with ten stars (Figure 5.2.b), utilizing aperture rotation through night. a) u-v coverage of 17 mirror array over 1 hr of observation b) u-v coverage of 17 mirror array over 3 hr of observation c) u-v coverage of 17 mirror array over 8 hr of observation. d,e and f are the corresponding reconstructed images obtained by speckle imaging in each case. The latitude of the site was taken as 60^0 North and the declination of the star cluster is considered to be 90^0. The images where reconstructed from 500 speckle frames each with an average of 10,000 photon counts. 86

5.7 Reconstruction of a Binary Star with Brightness ratio 1000:1 at different magnitudes. The aperture used is an array of 50 mirrors with 7 hours of earth roatation aperture synthesis, which increases the spatial frequency coverage. (Top row) The ideal cophased image and speckle image of the binary star. (Bottom three rows) The reconstructed images using the bispectrum technique with the corrosponding photon counts. The region inside the red circle is used to compute the SNR. 87

5.8 Reconstructions of a resolved star with spots at different magnitudes. The aperture used is an array of 50 mirrors with 7 hours of earth roatation aperture synthesis, which increases the spatial frequency coverage. (Top row) The ideal cophased image and speckle image of the resolved star. (Bottom three rows) The reconstructed images using the bispectrum technique with the corrosponding photon counts. 88

5.9 The SNR of the reconstructed images plotted against photon count in the speckle images for both Binary star and the resolved star with spots. The magnitude is calculated corresponding to the parameters used in the simulation as listed in table 5.1 and 5.2. 89

5.10 A schematic distribution of the dust clouds and AGN core model assumed in Schartmann *et al.* (2008) . (Left) The AGN core is the red dot at the center, while the pale blue regions show which clouds have direct lines of sight to the core and hence are heated. (Right) Clumpy torus model. Yellow regions indicate the directly illuminated surfaces of the clumps. i is the inclination angle, θ is the half opening angle of the torus. (Schartmann *et al.*, 2008) 90

5.11 The reconstructed images of the dusty torus around the AGN. The aperture used for imaging and the corresponding u-v coverage is also shown. The 3rd column is of edge-on geometry model and 4th column is of the pole on geometry. (Surya et al., 2015) 92

5.12 Exoplanet transit across a resolved star, as imaged by a 17 mirror cophased diluted Hypertelescope with maximum baseline of 100m. The star disk is 27 resels while the exoplanet is 3 resels in the image. The simulated image is a combination of 3 seperate images at different wavelengths. 93

5.13 Simulated Hypertelescope Image of the Exoplanet Transit in different wavelengths. 93

5.14 Simulated Hypertelescope Images of binary stars and star clusters. 94

6.1 The optical scheme planned in the prototype at Moutiere valley. The light from the star is reflected on to the gondola by the mirrors in the valley, and then the image is observed indirectly through a coude setup. (Labeyrie *et al.*, 2012b) 100

6.2 Driving system built at Ubaye. The gondola is suspended 100 m above ground at a 800 m meridian traversing cable, via a rolling pulley, with oblique wires defining its x,y,z position. The cables attachment points in the cliffs on both valley sides are approximately aligned with C1, the center of curvature of the primary dilute mirror, so that it can pendulate to allow the East-West motion of the gondola. The angle of its chainette sag at the gondola provides a spring-like lifting force which tensions the driving wires. These are controlled by ground winches, computer driven, located at the East side, the West side and the South side at the polar projection of C1. The motors at all three points, spaced about 200m apart, are synchronized by innovative wireless links. The gondola motion is equatorial and allows a Coude focus to be projected toward the South winch. The power need for the winches is minimized by tensioning the wires with counterweights. All the system use solar energy relayed by batteries during the night. (Labeyrie *et al.*, 2012b) 101

List of Tables

3.1 Parameters used in the numerical simulations of aperture masking speckle imaging 57

4.1 Comparison of computational requirements and reconstruction quality parameter, c of direct bispectrum and tomographic algorithms. The values are calculated based on MATLAB 32-bit used in a 32-bit Windows system with 4 GB of RAM. 70

5.1 Parameters associated with aperture configuration. 79

5.2 Parameters used in the simulation of hypertelescope imaging in the presence of atmospheric turbulence 80

5.3 The values of correlation coefficient c corresponding to the reconstruction of sextuple star and extended object from the speckle images with 17 mirror and 50 mirror array. 83

5.4 The correlation coefficient values corresponding to the reconstruction of the star cluster with increasing hours of observation to utilize aperture rotation. The array used is of 17 sub-apertures. 86

Chapter 1

Introduction

1.1 History of high resolution imaging.

Two important methods used in observational astronomy are imaging and spectroscopy. One of the important factors required in astronomical spectroscopy is the light gathering power of the telescope, which is determined mainly by the telescope collecting area and efficiency of the detector and optical subsystems. In imaging the light gathering power of the telescope is important for observing fainter stars, but the other equally important aspect of astronomical imaging is the optical resolution. Resolution determines the smallest details in the image, and is directly proportional to the size of the telescope aperture. Thus, it has been the quest of the mankind to build telescopes of bigger sizes and larger collecting areas. In this quest we have been faced with a number of challenges, including technological limitations with optics and detectors, degradation by atmosphere and other factors. Still, using ingenious workarounds and ideas we have been seeing objects further and further away with increasing detail.

Stellar interferometry was pioneered by H. Fizeau in 1860's. In 1867 Fizeau remarked that interference fringes produced from a source of finite dimensions must necessarily be smeared by an amount depending on the size of the source. He suggested that observation of the smearing, or lack of clarity of the fringes, created by a star through a large telescope, whose aperture was

masked by a pair of well-separated apertures, could be used to put an upper limit on its angular dimensions. Stéphan (1874) worked on the idea and within a few years he masked the aperture of the 30″ telescope at Marseille Observatory. He did it in a manner which gave two identical apertures the largest possible separation and observed fringes crossing the now enlarged image of a star.

Michelson's [1] papers in 1890 and 1891 rejuvenated the idea of stellar interferometry by describing in detail how it should be carried out by measuring the fringe visibility, as a function of aperture separation. The technique he used for these calculations was to understand the superposition of the interference fringes created from each point on the extended disk of the star. The concept of the coherence function, usually used for such calculations today, arose decades later from the work of Zernike in 1938. Michelson pointed out that for useful measurements of stellar diameters to be made, apertures separated by up to $10m$ would be required. Michelson soon applied this technique to resolve the satellites of Jupiter using the 40″ Yerkes refractor with a fizeau mask. This was followed by observations from Schwarzchild and Villiger (1891). In 1920 Anderson placed a fizeau mask on top of 100″ telescope in Mount Wilson and measured separation of binary star Capella. In 1921 Michelson and Pease built what is now called the 'Michelson Stellar Interferometer' (see Figure 1.1). It had two 6″ mirrors mounted in a periscopic fashion and could have baselines up to $20 feet$. Michelson used this instrument to measure the diameter of α-Orionis. Pease followed up this work with the measurement of 6 more stars (Pease, 1931). In 1946 a radio analog of the Michelson Interferometer was built (Ryle and Vonberg, 1946) to study radio

[1]

> "If now it be possible to find a relation between the size of the object, and clearness of the interference fringes, an independent method of measuring such minute objects will be furnished; and the purpose of this paper is to show that such a method is not only feasible but in all probability gives results far more accurate than micro metric measurements of image" –Michelson (1891)

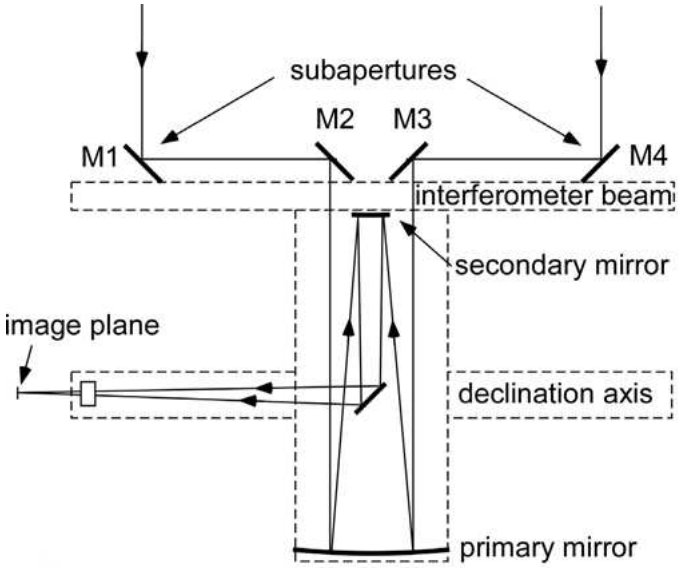

Figure 1.1: Layout of Michelson Stellar Interferometer. M1, M2, M3 and M4 are mirrors used to form the periscopic arrangement (image courtesy: A. Labeyrie).

emissions. This led to the development of aperture synthesis, which is the technique of synthesizing large telescopes using movable apertures. The next big step in high resolution imaging was the invention of intensity interferometry by Brown and Twiss in 1956. An intensity interferometer measures the correlations between intensities at two points observing the same source. The principle of intensity interferometry was used to build the Narrabi intensity interferometer (Brown et al., 1974) which had two separate telescopes with separations up to $188m$. Tolerance to mechanical precision and immunity to atmospheric scintillation are remarkable properties of such an interferometer. An intensity interferometer measures correlations in light intensity, which gives the modulus of complex degree of coherence. Another break through in the quest for high resolution was made by Antoine Labeyrie in 1970 with invention of speckle interferometry. It takes advantage of the randomness of atmospheric fluctuations to obtain the Fourier amplitude of the object. This was a milestone in observational astronomy using single aperture telescopes. In 1975, Labeyrie constructed the first two telescope interferometer called I2T (interferometer a deux telescope) with $12m$ base line (see Figure 1.2). He

Figure 1.2: I2T Interferometer (Labeyrie et al. 2006).

Figure 1.3: GI2T Interferometer in Calern (Labeyrie et al. 2006).

obtained interferometric fringes of Vega this interferometer. Following the success he moved to a better site, at Centre d'Étude et de Recherches en Géodynamique et Astronomie (CERGA) (Labeyrie, 1978). Soon followed the construction of the GI2T (Grand Interféromètre à 2 telescopes) interferometer with two boule telescopes each with $1.5m$ telescopes that run on North South Tracks (see Figure 1.3). The first fringes with GI2T were obtained in There was also a great deal of development in the active and adaptive systems used for atmospheric correction during the 1980's, though this concept was already developed earlier in 1953 by Babcock.

One of the remarkable fields that developed together with high reso-

lution optical interferometry is image restoration algorithms. Deconvolution schemes like MEM (Maximum Entropy Method; Frieden (1972); Ponsonby (1973); Ables (1974)) and CLEAN (Högbom, 1974) together with phase restoration schemes, like closure of phase by Jennison (1958), supplemented the technological advancements in radio interferometry. In speckle interferometry Knox-Thompson and Weigelt led the development of Knox-Thompson Technique (Knox and Thompson, 1974) and Triple Correlation (Weigelt, 1977) respectively. Several new image reconstruction algorithms have been developed since to particularly work with the long baseline optical interferometric data. MIRA (Multi Aperture Image Reconstruction Algorithm) (Thiébaut, 2008) seeks for image restoration based on direct minimization technique. The MEM based techniques has been exploited in optical interferometry algorithm developed at Cavendish Laboratory called BSMEM (Bispectrum Maximum Entropy Method) by Buscher (1994). The Building Block Method developed by Hofmann and Weigelt (1993) uses principles close to CLEAN. WISARD (Weak-phase Interferometric Sample Alternating Reconstruction Device), an algorithm developed by Meimon et al. (2009) at ONERA (Office National d' Etudes et de Recherches Aerospatiales) with JMMC (Jean-Marie Mariotti Center) uses the method of self calibration. The Interferometric Imaging Beauty Contest (Lawson *et al.*, 2004; Baron *et al.*, 2012) conducted by International Astronomical Union's Working Group on Optical/Infrared Interferometry allows a very good platform to compare the reconstruction capabilities of these algorithms.

1.2 Basics of Optical Interferometry

1.2.1 A simple model for a two telescope interferometer

Consider a basic two aperture interferometer as shown in Figure 1.4 with apertures A_1 and A_2 located at positions $\mathbf{x_1}$ and $\mathbf{x_2}$ respectively. The dis-

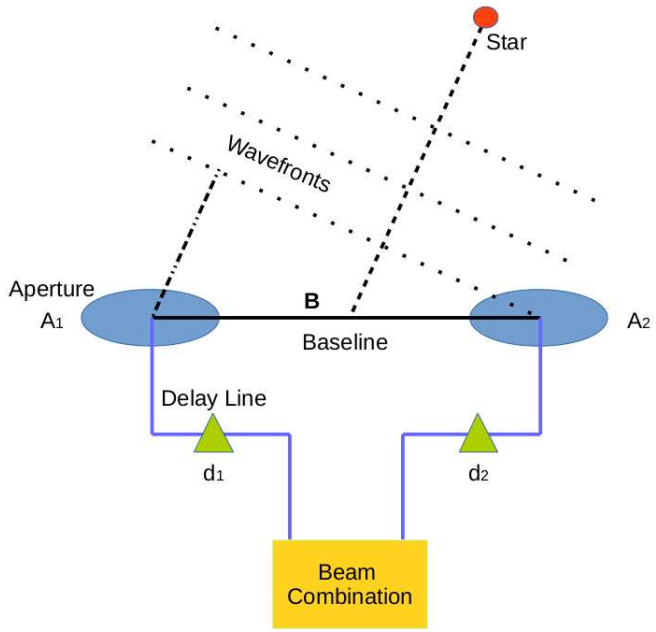

Figure 1.4: A basic model of a two telescope interferometer. The plane wavefronts from the star are incident on the two apertures, A_1 and A_2. The path lengths are adjusted using delaylines, d_1 and d_2, for the beams to coherently combine to form an interference pattern.

placement vector for such a baseline is $\mathbf{B}$ equal to $\mathbf{x_2} - \mathbf{x_1}$. The unit vector, $\widehat{\mathbf{s}}$, gives the direction of the baseline to a single point source. Consider for simplicity that the astronomical source is monochromatic with wavelength λ. The optical fields at positions $\mathbf{x_1}$ and $\mathbf{x_2}$ are given by,

$$\phi_1 = e^{-ik\widehat{\mathbf{s}}.\mathbf{x_1}} e^{-i\omega t}, \tag{1.1}$$

$$\phi_2 = e^{-ik\widehat{\mathbf{s}}.\mathbf{x_2}} e^{-i\omega t} \tag{1.2}$$

ϕ_2 can be also written as,

$$\phi_2 = e^{-ik\widehat{\mathbf{s}}.\mathbf{x_1}} e^{-ik\widehat{\mathbf{s}}.\mathbf{B}} e^{-i\omega t}. \tag{1.3}$$

After normalization we can write,

$$\begin{aligned} \phi_1 &= e^{-i\omega t}, \\ \phi_2 &= e^{-ik\widehat{\mathbf{s}}.\mathbf{B}} e^{-i\omega t}. \end{aligned} \tag{1.4}$$

After arrival at A_1 and A_2 the fields travel distances d_1 and d_2 incurring additional phase.

$$\begin{aligned} \phi_1 &= e^{-ikd_1}e^{-i\omega t}, \\ \phi_2 &= e^{-ikd_2}e^{-ik\hat{\mathbf{s}}.\mathbf{B}}e^{-i\omega t}. \end{aligned} \tag{1.5}$$

The combined field at the detector is given by,

$$\phi_{com} = \phi_1 + \phi_2 = e^{-i\omega t}(e^{-ikd_1} + e^{-ikd_2}e^{-ik\hat{\mathbf{s}}.\mathbf{B}}). \tag{1.6}$$

From this we can deduce the time averaged power at the detector,

$$P \propto \phi^*_{com}\phi_{com} = 2\Big[1 + cos\, k(\hat{\mathbf{s}}.\mathbf{B} + d_1 - d_2)\Big]. \tag{1.7}$$

If the incident source flux power is F and collecting area of Apertures is A then

$$\begin{aligned} P &= 2AF\Big[(1 + cos\, k(\hat{\mathbf{s}}.\mathbf{B} + d_1 - d_2)\Big], \\ &= 2AF\Big[1 + cos\, kD\Big]. \end{aligned} \tag{1.8}$$

The equation 1.8 has the form of interference fringes with power as a function of optical delay D. This is shown in Figure 1.5. The adjacent fringe crests are separated by an angle,

$$\Delta s = \frac{\lambda}{B}. \tag{1.9}$$

1.2.2 Coherence Function

The coherence function or complex degree of coherence is a normalized correlation function between the complex wave fields $\phi(x,t)$ at two points x_1 and x_2.

$$\nu(x_1, x_2) = \frac{\langle \phi(x_1,t)\phi^*(x_2,t)\rangle}{\sqrt{\langle|\phi(x_1,t)|^2\rangle\langle|\phi(x_2,t)|^2\rangle}}, \tag{1.10}$$

where $\langle..\rangle$ is average taken in time. Physically the coherence function tells you how good the interference pattern between the points will be.

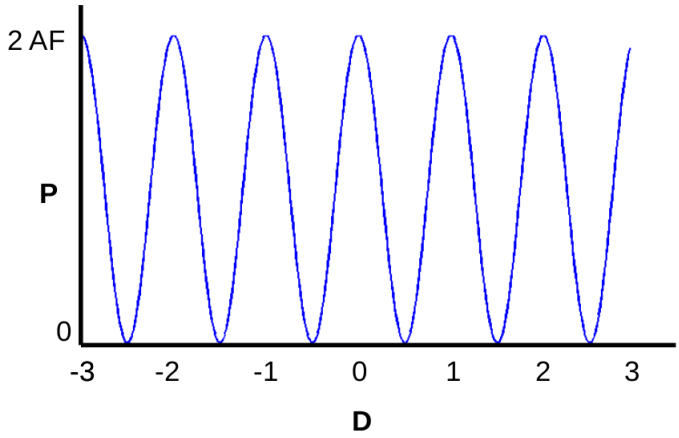

Figure 1.5: The power measured at the detector of the 2 telescope interferometer as a function of optical delay.

1.2.3 Visibility and Van Cittert–Zernike theorem

Visibility, V of the fringes is defined as the contrast between light and dark areas (P_{max} and P_{min}) of the observed fringes. This is a dimensionless quantity given by the equation,

$$V = \frac{P_{max} - P_{min}}{P_{max} + P_{min}}. \tag{1.11}$$

An important property of visibility is that it is dependent on source size and resolution of interferometer. When the sources are unresolved, the fringe visibility is 1. As the sources becomes more and more extended and thus resolved by the interferometer the fringes decrease in amplitude and the visibility becomes less than 1. An example of the two sources with different visibilities is given in Figure 1.6.

The fringe visibility V is directly related to coherence function ν. If P_1^2 and P_2^2 are mean intensities of optical fields at A_1 and A_2 respectievely. The visibility of the fringes V at the detector is given by

$$V = \frac{2P_1P_2}{P_1^2 + P_2^2}.|\nu(A_1, A_2)|. \tag{1.12}$$

The Van Cittert–Zernike theorem (Van Cittert, 1934; Zernike, 1938) gives the relationship between the interferometer response and the brightness distribution of the target. It states that, for a monochromatic incoherent source,

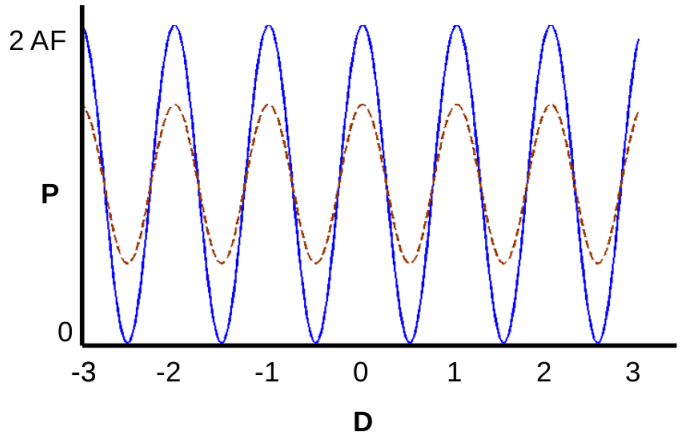

Figure 1.6: The fringes of a point source (blue) and an extended source (red dotted)

the Fourier transform of the complex spatial coherence function is the angular intensity distribution of the source. This theorem is the spatial analog of the Wiener–Khinchin theorem (Wiener, 1930; Khintchine, 1934) for a time-dependent wave, which states that power spectrum is the Fourier transform of its temporal autocorrelation function. The Van Cittert–Zernike theorem gives us the ability to find out the details about the observed object from measuring fringe visibilities. This is a fundamental theorem of astronomical interferometry.

1.3 Speckle Masking and Speckle Interferometry

If an ideal infinite aperture telescope is used to observe a monochromatic point star, the image would be a single peak $\delta(\mathbf{r}_0)$ in the focal plane $\mathbf{r}$. But because of both the atmosphere and the limited telescope aperture, the image recorded is $S(\mathbf{r};t)$, which is the instantaneous atmospherically degraded monochromatic, point spread function (PSF) of the telescope, at time t. This is called a "speckle pattern". The image of a source object observed by a telescope, $I(x,y)$ is the convolution between this PSF, $S(x,y)$ and the ideal

image of the source, $O(x, y)$.

$$I(x, y) = S(x, y) * O(x, y). \tag{1.13}$$

The above equation represents the intensity of the image. For large telescopes the phase distortions across the aperture gives rise to speckle patterns rather than airy diffraction pattern. Because atmospheric turbulence results in changes of the PSF in the order of milli-seconds, the speckle pattern needs to be recorded using a short exposure detector. These speckle images can be recorded directly using an image intensifier and a video camera recorder, or with the newer Electron Multiplying Charge Coupled Device (EMCCD) systems (Saha,2015 and references therein). In long exposure images these speckle patterns gets averaged out in the image plane and results in a blurred image. This effect is shown in Figure 1.7. This atmospheric degradation is the major challenge in astronomical imaging. In 1970 A.Labeyrie found out a way to get around atmosphere through the ingenious method of speckle interferometry (Labeyrie, 1970). The technique is to take a two-dimensional Fourier transform of the images and to sum the square modulus of the Fourier transforms. From this one can obtain the spatial power spectrum of the object. Details of this are explained in Section 3.2.3. From the spatial power spectrum function one can calculate by Fourier transform, the spatial autocorrelation, but not the actual star image. Thus, since the spatial autocorrelation function cannot uniquely be translated to an image, the application of speckle interferometry seems to be limited even though it does provide a wealth of information about simple stellar objects. For example, a binary pair can easily be recognized, and the separation of the elements, their relative intensities and their orientation deduced; but one cannot distinguish between two centro-symmetric possibilities for the image (e.g. brighter element on the left or on the right).

Again, limb darkening or other intensity variations as a function of radius of the star determined this way must also be assumed to be centro-symmetric. On the other hand, if one looks at the speckle images of a binary star for

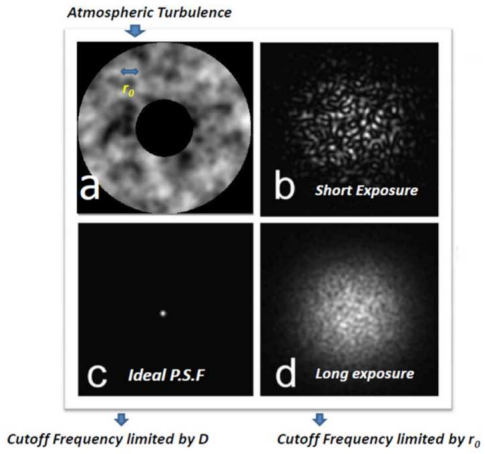

Figure 1.7: Atmospheric degradation in astronomical imaging. a) The phase perturbations across a single aperture telescope. b) The short exposure speckle PSF. c) The ideal diffraction limited PSF. d) The long exposure PSF which is the average of several short exposure PSF.

example, one can identify with manual observation, which component is on the left and which on the right. This happens because the individual speckles are like diffraction-limited PSF patterns. Thus it was clear that the technique should not really be limited by the spatial autocorrelation function; and after publication of the first speckle results it quickly became a challenge to find algorithmic methods to extract image information directly.

The first successful method of deducing the phases of the Fourier components was by Knox and Thompson (1974). The algorithm involved transforming the image in frequency plane and then correlating it with a shifted version of itself. The shift vector is chosen very small and the correlation is summed over many frames to obtain diffraction limited image.

Another method of determining the phase of the transform $S(\mathbf{u})$ is to use the ideas behind phase closure. The idea was proposed by Weigelt and Hoffman (1977). It has the advantage that larger discrete steps in spatial frequency $\mathbf{u}$ can be used, so that it is less error prone than the Knox–Thompson algorithm. Despite the large computation times involved in processing speckle sequences by this method, it has produced excellent quality images of quite complicated scenes. Till now this remains one of the better methods of image

reconstruction.

1.4 Long Baseline Optical Interferometers

The success of GI2T prompted the development of many new optical interferometers. These interferometers has contributed in understanding and discovering new science in high resolution. VLTI (Very Large Telescope Interferometer) is an optical interferometer at ESO (European Southern Observatory). It consists of four 8 m telescopes and four small 1.4 m telescopes. The telescopes are used individually or used in interferometric mode using different instruments like MIDI (Mid Infrared Instrument) and AMBER (near-infrared/red focal instrument for the VLTI). Keck Interferometer, located in Mauna Kea in Hawaii, consists of two large 10 m segmented mirrors separated at baseline of 85 m. Like VLTI, the telescopes can work individually or in interferometric mode. The CHARA (Center for High Angular Resolution Astronomy) array is maintained by Georgia State University. It has six 1 m telescopes with a maximum separation of 330 m.

These current interferometers use 2-4 telescopes and can only sample a small part of the spatial frequency space at once. Techniques like aperture synthesis allows compensation of this drawback and helps to produce usefule results with these interferometers. But snapshot imaging with these interferometers are difficult owing to their poor spatial frequency coverage. Diluted aperture interferometers like Hypertelescopes offer an innovative way to obtain snapshot images of stellar objects.

1.5 Hypertelescope

Multi-aperture interferometric arrays could provide direct snapshot images. Such arrays can be of diluted design, with a large number of smaller mirrors spread over a large area. A problem with such type of direct imaging is that the PSF will contain a broad halo of diffracted light surrounding the

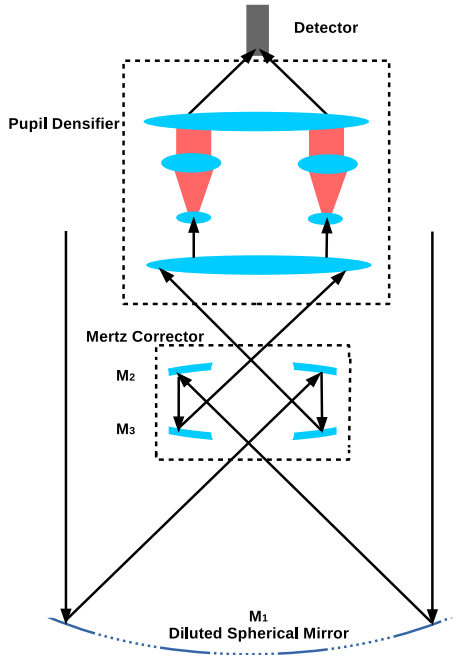

Figure 1.8: Layout of a hypertelescope showing the different parts.

central interference peak. A considerable amount of energy is diffracted in to this side halo and leaves only a smaller part of energy in the central peak. De-convolving the complex speckle structure in the halo also will be a difficult problem. A solution to this is an innovative beam combination scheme called densified pupil imaging or 'hypertelescope imaging'. The hypertelescope is essentially a multi-aperture Fizeau interferometer which is equipped with auxiliary optics to "densify " the exit pupil (see Figure 1.8). This intensifies the central peak and makes it usable, with the diluted array. Most of the light received from an on-axis star is concentrated in to the central peak if the diluted array is phased accurately. This peak also moves corresponding to the star motion within a limited field of view. These properties have been already verified by numerical simulations, laboratory experiments and prototypes.

1.6 Motivation

Interferometric imaging through aperture synthesis with many baselines have been highly successful at radio wavelengths and has also given significant results in optical wavelengths. But it has been only recently that it was realized that many-aperture optical arrays can provide snapshot images, with arbitrarily diluted apertures using hypertelescope imaging. This "hypertelescope" (Labeyrie, 1996) approach to imaging may be viewed as a simple modification of the classical Fizeau interferometer employing pupil densification. It has a vast potential, particularly in space where large arrays of relatively small apertures may become easy to implement with forthcoming techniques of formation flying. Prototypes of such systems already have been developed (Le Coroller *et al.*, 2012a, 2015) and tested. Large scale prototype versions like Ubaye Hypertelescope are under development (Labeyrie *et al.*, 2012b).

A major challenge for these type of hypertelescopes is the adaptive phasing system. Modified wave sensing techniques such as dispersed speckle analysis (Borkowski *et al.*, 2005) are planned to be used with these systems. But development and installation of such advanced techniques will take time. In such a scenario speckle mode observations with hypertelescopes becomes a viable alternative. Even in the initial versions of hypertelescopes (Pedretti *et al.*, 2000) phase variations resulted in speckle images. In this thesis we aimed to study imaging with such diluted aperture interferometers in speckle mode with techniques like speckle interferometry (Labeyrie, 1970) and speckle masking (Weigelt, 1977; Lohmann *et al.*, 1983).

For adaptively phased imaging and speckle imaging, the incomplete output pupil filling provides a serious challenge for perfect imaging. Even after densification of the input diluted aperture, the PSF will have a dominant speckle halo surrounding the central peak, due to partial filling of the output pupil. Similar to a study by Reinheimer *et al.* (1993) for VLTI (Very Large Telescope Interferometer) and Reinheimer *et al.* (1997) for LBT (Large

Binocular Telescope), it is shown in this thesis work with the help of numerical simulations that even with smaller pupil filling rate in output pupil, high resolution imaging can be done with these interferometers by utilizing aperture rotation through the night. Techniques for using aperture rotation with speckle techniques for better reconstruction are discussed in the thesis.

The study of speckle reconstruction algorithms with hypertelescopes is important for two main reasons. The imaging equation of hypertelescopes are different from normal imaging system due to use of pupil densification. Unlike normal imaging systems, the pseudo-convolution equation of the hypertelescope imposes a field of view restrictions. Also in a pupil densified system the PSF is not anymore space-invariant. Secondly gaps in spatial frequency sampling due to the large baselines of diluted apertures are a problem for imaging and reconstruction and use of aperture rotation through night is required to fill the gaps in u-v plane. How this can be achieved in speckle imaging, is probed in this thesis.

The imaging properties of hypertelescope in cophased mode have been studied extensively before by Lardière *et al.* (2007) and Patru *et al.* (2009). In this thesis we try to develop our own image reconstruction algorithms using triple correlation and try to understand its applications to diluted arrays with speckle imaging simulations.

1.7 Thesis Overview

This thesis mainly concentrates on the development of speckle interferometric and speckle masking code for obtaining diffraction limited images from optical telescopes and its applications to direct imaging optical interferometers. The algorithms developed have been tested with real speckle images, experimental simulations and numerical simulations. The image processing techniques developed can be used with data of any type of optical telescope, but the application of the code in this thesis is mainly concentrated on long-baseline interferometer and hypertelescope simulations. Hypertelescope and

long-baseline interferometer simulation software was also developed as part of the thesis which simulates both cophased and speckle imaging.

Chapter two discusses the details of the numerical algorithms used to simulate different optical interferometers and their images. We have developed a numerical simulation code to simulate imaging of different direct imaging optical interferometers. Different beam combination schemes and different array configurations could be simulated using this software. The codes are used extensively in our study of different image reconstruction algorithms. The details of these numerical simulation code are described in the Chapter.

Chapter three describes the technique of triple correlation and direct bispectrum based image reconstruction from speckle images. The algorithm uses four dimensional bispectrum of short exposure speckle images to reconstruct the phase of the observed object. We have developed a direct bispectrum based image reconstruction code to retrieve stellar images. This algorithm with the technique is explained with details and results.

Chapter four explains the Tomographic Speckle masking algorithm. The direct bispectrum algorithms are computationally expensive and a significant gain in running time and computational resources can be achieved by utilizing tomographic techniques. We have also developed such a technique called Tomographic speckle masking using Radon Transform that used one dimensional projections of speckle images to retrieve object information. This technique achieves savings in computational time and memory. The results of the developed algorithm with real and experimentally simulated speckle data are also discussed in this Chapter. Also the algorithm is compared with Direct bispectrum code to understand its usability.

Chapter five concentrates on speckle imaging with hypertelescopes. Developed algorithms of bispectrum based reconstruction has been used with simulations of hypertelescope imaging to obtain reconstructed images of significant Signal to Noise Ratio (SNR). In the absence of adaptive optics for such diluted aperture telescopes, speckle imaging could be a real alternative to obtain high resolution stellar images. The Chapter discusses the details

of the simulations with the prospects of using the developed algorithms with future hypertelescopes.

The sixth chapter concludes the thesis with brief discussion of the results that has been achieved and the important lessons that has been learned during the study. The chapter also discusses the future prospects of the algorithms that have been developed and its application to the upcoming large optical interferometers.

Chapter 2

Numerical Simulation of Optical Interferometers

2.1 Importance of phase in signals

Phase variations in the incident wavefront effects the image formation. The complex field distribution at focal plane of a telescope is related to that at the image plane through a Fourier transform. The intensity of a point source recorded at the image plane is the spatial power spectrum of the complex field at the entrance aperture (Goodman, 2005). By the autocorrelation theorem (Wiener Khinchin theorem; Wiener (1930); Khintchine (1934)), the inverse Fourier transform of the intensity image is then equivalent to the autocorrelation of the complex field distribution at the entrance aperture. Thus the presence of any degradation in the phase of the wavefront at the aperture plane would mean degradation of the Fourier transform at the image plane. In this context it is important to probe the influence of phase in a signal. The importance of phase in signals have been studied in detail by papers by Oppenheim and Lim (1981) [1] and Roddier (1987). We have done our own

[1]

> "In the Fourier representation of signals spectral magnitude and phase tends to play different roles and in some situations,many of the important features of signals are preserved if only the phase is retained." - Oppenheim and Lim

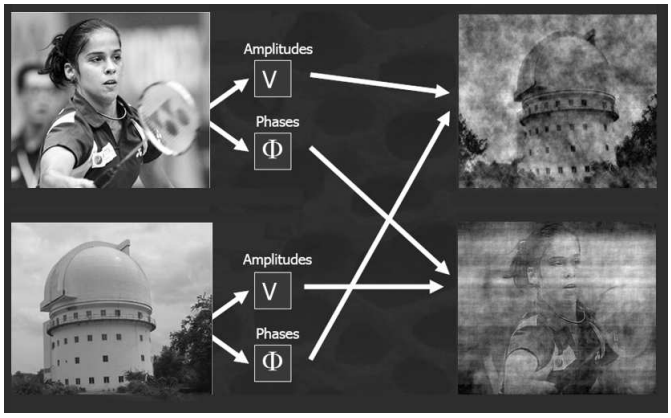

Figure 2.1: Example demonstrating importance of phase in signals

numerical experiments to better understand the importance of phase. The results are shown in Figure 2.1. It is seen that from phase information most of the signal can be recovered. Two images, one the portrait of a sports women, and the other, an image of VBT (Vainu Bappu Telecope) dome were used in the experiment. When each other's Fourier phase and amplitudes where exchanged, it was observed that the resultant image showed dominance of the phase part that was used. This experiment clearly shows the dominance of phase in signals.

2.2 Atmospheric phase variations

The atmosphere behaves like a very thick bad piece of glass in front of your telescope, a piece which is constantly changing[2]. This essentially is a bad

(1981)

[2] "Doubtless this rather unexpected result may be explained as follows: The confusion of the image in poor seeing is due to the integrated effect of elements of the incident light waves, elements which are not in constant phase relation in consequence of inequalities in the atmosphere due to temperature differences; the optical result being a "boiling" of the image, closely resembling the appearances of objects viewed over a heated surface." – Michelson.A.A, 'Studies of Optics' (1927)

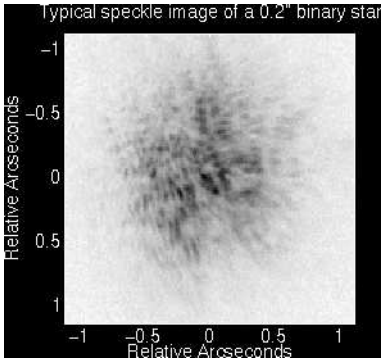

Figure 2.2: A speckle image (Saha, 1999)

optical element in the imaging process of the telescope. The result of this bad optical element is that the image of a point star is not the diffraction pattern of the geometrical entrance aperture, but a much more complicated and diffused image. The image has two properties: an envelope, which is the image recorded in a long-exposure photograph ($> 1\ s$) and, within it, an internal speckle structure which is continuously and rapidly changing and can only be photographed using a very short-exposure($< 100\ ms$). On the other hand, even if the speckle structure is continuously changing, the angular diameter of its smallest distinguishable features correspond to the diffraction limit of the complete telescope aperture. Figure 2.2 shows a real speckle image by the speckle interferometer developed by Saha et al. (1997).

2.2.1 Kolmogorov Turbulence Model

The history of turbulence analysis begins with two famous papers by Kolmogorov (Kolmogorov, 1941; Kolmogorov, 1991) called as K41 which described for the first time a simple model for the spatial and temporal behavior of turbulent motion of a fluid. Turbulent motion arises when motion is dominated by inertial rather than viscous effects, so that kinetic energy of flow may be transferred from one direction to another, or from one scale to another, but is not damped out and converted to heat by viscosity.

Correlation functions are widely used to describe statistically varying

fields, so we might find it natural to express the fluctuations in such terms. Kolmogorov (1941) devised a slightly different way of expressing measures of turbulence. He defined a structure function to relate the values of a function $f(r)$ at neighboring points $\boldsymbol{r_1}$ and $\boldsymbol{r_2}$,

$$D_f(\boldsymbol{r_1}, \boldsymbol{r_2}) = \left\langle [f(\boldsymbol{r_1}) - f(\boldsymbol{r_2})]^2 \right\rangle , \tag{2.1}$$

where $\langle\rangle >$ indicates a time-averaged value. In a homogeneous region, this is a function only of $\boldsymbol{r} = \boldsymbol{r_1} - \boldsymbol{r_2}$ and not of their individual values, so that we can write

$$D_f(\boldsymbol{r}) = \left\langle [f(\boldsymbol{r} + \boldsymbol{r_1}) - f(\boldsymbol{r_1})]^2 \right\rangle . \tag{2.2}$$

For such a structure function a correlation function can also be related.

$$B_f(\boldsymbol{r}) = \left\langle \left[f(\boldsymbol{r} + \boldsymbol{r_1}) - \overline{f}\right] \left[f(\boldsymbol{r_1}) - \overline{f}\right] \right\rangle , \tag{2.3}$$

where $\overline{f}$ is the mean value.

The structure function $D_n(\boldsymbol{r})$ for the refractive index fluctuations contains enough information to build up a good representation of the atmospheric degradation of an optical telescope, which can also be confirmed experimentally. The main effect of the turbulence is to disturb the relative phases of the incident wave at different points in the aperture. Following the methods used in an important review by Roddier (1981), we can calculate the integrated effect of the whole atmosphere at the ground plane. We assume that the phase fluctuations are relatively small, so that when a plane wave is incident from outside the atmosphere, we can calculate its phase properties. This is done by integrating along columns of air, determined by the geometrical path it would have if the atmosphere were completely uniform.

2.2.2 Fried's Parameter

If a telescope has an aperture diameter d, which is small enough that the atmospherically distorted phase wavefront from a point star is well correlated

over the whole of it, the resolution of the telescope is determined by d, as if the atmosphere had no effect. On the other hand, if d is very large, the resolution is determined by the atmospheric properties ('the seeing'), and the large telescope diameter is only important in collecting more light. A physically intuitive parameter which describes the phase correlations was defined by Fried (1966). Fried's parameter r_0 is the value of d for which the two limitations are equivalent.

$$D_\phi(r) = 6.88\Big(\frac{r}{r_0}\Big)^{\frac{5}{3}} \tag{2.4}$$

Fried's parameter can be expressed in terms of refractive index structure constant by the following equation

$$r_0 = 0.185\lambda^{\frac{6}{5}} cos^{\frac{3}{5}} z[\int C_N^2(h)dh]^{-\frac{3}{5}}, \tag{2.5}$$

where λ is the wavelength, z is the zenith angle, $C_N^2(h)$ is the atmospheric turbulence strength which is a function of height h.

2.2.3 Simulating Kolmogorov Phase Screen

The atmospheric fluctuations are modeled by representing the phase $\phi(r)$ as a random function which changes by amounts in the range of $[-\pi, \pi]$ from point to point on the distance scale of Fried's parameter r_0. The modeling of atmosphere in simulation allows any wavefront structure function to be used, although it appears that the differences between the results for the Kolmogorov structure function and a random Gaussian approximation are very minor. The speckle PSF is an image of a point source degraded by the phase distortions produced by the atmosphere. Assuming that the amplitude variations are relatively insignificant, we can describe the image as the Fraunhofer diffraction pattern (i.e. Fourier transform, $F(\boldsymbol{u})$) of the function $f(\boldsymbol{r}) = S_0(\boldsymbol{r})e^{i\phi(\boldsymbol{r})}$. Here, $S_0(\boldsymbol{r})$ describes the telescope aperture, i.e. has value 1 within it and 0 outside, and would generally be $circ(\boldsymbol{r}/R)$, where R is the radius, or maybe an annular function to allow for a central obscuration

(secondary mirror). We describe here a simple model which has the right features and illustrates the physics. The technique used by us to simulate the atmospheric turbulence is the FFT (Fast Fourier Transform) technique (Lane *et al.*, 1992). It is computationally very fast. A major disadvantage of this technique is its inability to represent tilt based shifts due to turbulence. This is due to the problems of the technique with low frequencies. To avoid this effect, we create very large phase screens using the FFT method, but use only a smaller portion of it. This simple process allows to simulate phase screens where the lower frequencies are well represented. Random wavefronts with turbulence parameters are generated for different layers and they are superposed to simulate the resultant wavefront which simulates the effect of the whole column of the atmosphere. The temporal evolution of individual phase screens is obtained by moving the phase screens at each layer at a certain wind velocity obtained from the wind profile. A representation of the model of atmosphere is shown in Figure 2.3.

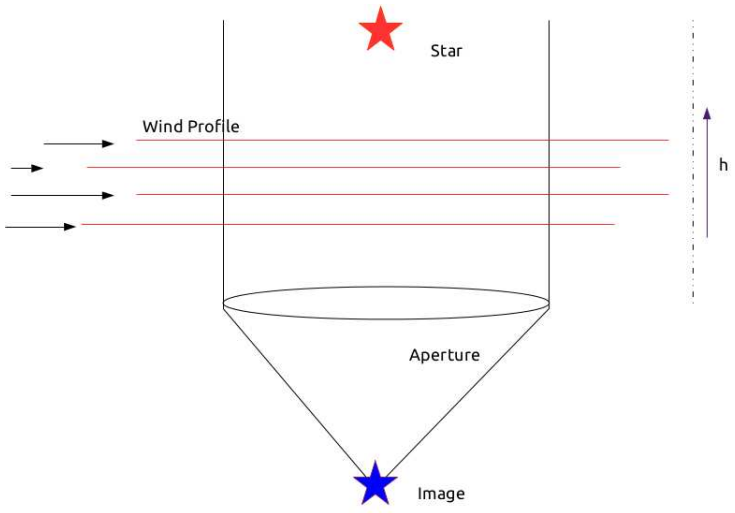

Figure 2.3: The multilayer model of turbulence used in the simulations.

The start of the process is to generate the power spectral density. The power spectral density in case of Kolmogorov phase screen is given by,

$$\Phi_N(\kappa, h) = 0.033 C_N^2(h) \kappa^{-\frac{11}{3}}, \tag{2.6}$$

where κ is the scalar wave number and h is the distance from the aperture. A

random process of known power spectrum can be simulated by applying an inverse Fourier transform on the square root of the power spectrum filtered with Gaussian noise. This principle is used to create different atmosphere layers. There are two important parameters required for such a simulation, they are the wind velocity model $v_w(h)$ and the turbulence strength $C_N^2(h)$. The wind velocity is dependent usually on site measurements, but a general model can be assumed to be a triangular function. We have obtained the wind velocity measurements from the following studies, Gentry *et al.* (2004); Roopashree *et al.* (2010) and García-Lorenzo *et al.* (2011).

The $C_N^2(z)$ profile is site dependent and choice of a standard model is very difficult. We have adopted the modified Hufnagel-Valley turbulence profile (Parenti and Sasiela, 1994) given by

$$\begin{aligned} C_N^2(h) &= 8.16 \times 10^{-5} h^{10} e^{-h/1000} + 3.02 \times 10^{-}17 e^{-h/1500} \\ &\quad +1.90 \times 10^{-}15 e^{-h/100} \end{aligned} \tag{2.7}$$

Subsequently the phase screens are generated using the two models and the entire atmosphere column is simulated. The structure function and other statistics are verified to closely represent Kolmogorov turbulence. We then constrain this phase screen by the bounding aperture S_0. Finally, we transform this back to the image plane u to see the speckle image or the atmospherically degraded point spread function.

2.3 Earth Rotation Aperture Synthesis

A very important development in the field of interferometry was the utilization of projected array baseline with earth's rotation. The rotation of earth enables an interferometer to sample visibilities at various spatial frequencies with the same ground baseline. This phenomenon has been exploited to increase the spatial frequencies sampled by the interferometer. We have incorporated the simulation of this time variance of baselines with time of observation. The detailed study of synthesis mapping has been done by Ryle

and Vonberg (1946); Thompson *et al.* (2001). If we consider a right-handed coordinate system (X, Y, Z) where X and Y are measured parallel to earth's equator. Y is measured towards east and Z towards the north pole. The (u, v, w) coordinates are defined for observation in the direction of point S, which has hour-angle and declination H and δ respectively. The coordinate

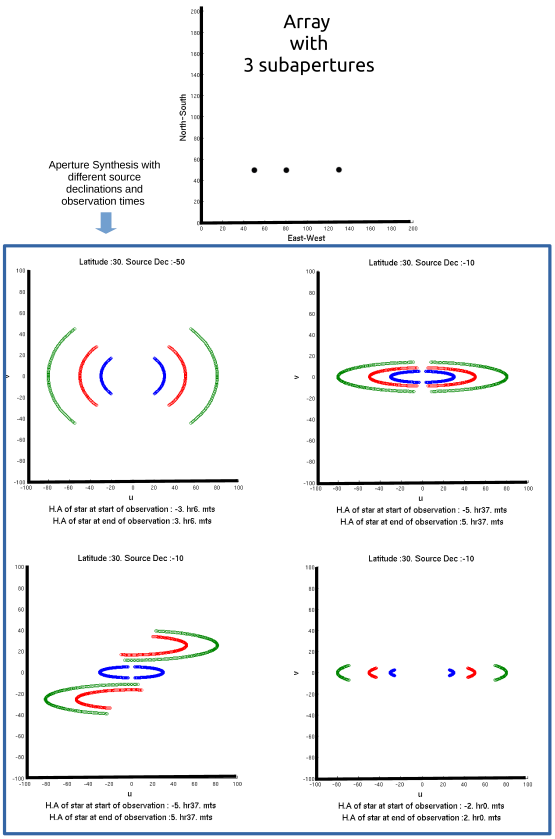

Figure 2.4: Earth Rotation Aperture Synthesis as simulated by the developed software. (Top) The 3 mirror aperture used in the simulation. (Middle and Bottom) Aperture synthesis with different latitudes, source declinations and hours of observation.

system (u, v, w) can be obtained from the array coordinates (X, Y, Z) by the following transformation.

$$\begin{bmatrix} u \\ v \\ w \end{bmatrix} = \begin{bmatrix} \sin H & \cos H & 0 \\ -\sin\delta\cos H & \sin\delta\sin H & \cos\delta \\ \cos\delta\cos H & -\cos\delta\sin H & \sin\delta \end{bmatrix} \begin{bmatrix} X \\ Y \\ Z \end{bmatrix} \tag{2.8}$$

The array rotation as simulated by the software using such a transformation is shown in figure 2.4.

2.4 Simulation of techniques in optical interferometry

For our study of image reconstructions from optical interferometers we have concentrated on direct imaging. For such simulations we have build a software package in MATLAB called IMAGIN which produces realistic images of different optical interferometers under atmospheric turbulence. The different types of optical interferometric techniques simulated by us are

- Aperture masking over single aperture telescope
- Long base line optical interferometers with large mirrors
- Diluted Optical interferometers

2.4.1 Aperture masking over single aperture telescope

Aperture masking is a technique of using masked apertures on a single aperture telescope (Baldwin *et al.*, 1986; Haniff *et al.*, 1987) and to process the fringe systems thus obtained to reconstruct the image. Aperture masking has been used together with speckle imaging to obtain results with better SNR (Saha, 2007). For aperture masking simulations we consider the equation of the PSF as

$$I(x,y) = A(x,y) \cdot \left| \sum_{j=1}^{N} e^{-\frac{2\pi i}{\lambda}(xu_j + yv_j)} \cdot e^{i\phi_j} \right|^2 , \tag{2.9}$$

with u_j and v_j the positions of the j^{th} subaperture, ϕ_j the corresponding atmospheric piston error and with $A(x,y)$ being the Diffraction Function corresponding to subaperture give by,

$$A(x,y) = \left| \frac{2J_1(\rho R)}{\rho R} \right|^2 , \tag{2.10}$$

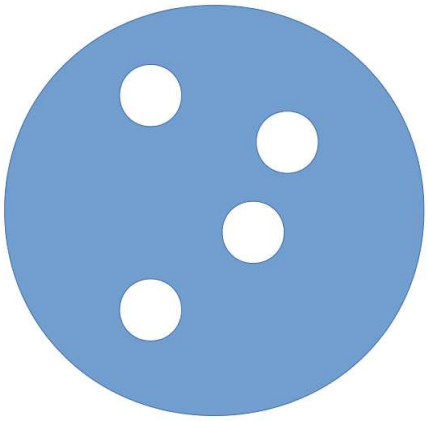

Figure 2.5: A simulated aperture mask with 4 sub-pupils

where $\rho = \frac{2\pi}{\lambda}\sqrt{x^2 + y^2}$ is the radial distance in reciprocal space and R is the radius of subaperture.

2.4.2 Multi-speckle images from long baseline interferometry

We have simulated imaging with pupil configurations similar to VLTI and LBT (see Section 1.4), which are optical interferometers in which sub-apertures are large in size ($1\ m - 10\ m$) and small in number ($2-6$). Such interferometers rely mainly on earth rotation synthesis to sample visibilities at different spatial frequencies. The simulations also include atmospheric degradation, earth rotation and photon noise. For such interferometric systems, with Fried's parameter r_0 is less than the sub-pupil aperture size, we will obtain 'multi-speckles' in the image plane. Multi-speckles are speckle images with the interference fringes inside each speckle. These fine interference fringes correspond to the larger baselines. The first long baseline interferometer to obtain such multi-speckle images is the GI2T interferometer at CERGA. We have developed simulations that closely resemble the observations of multi-speckles that can be obtained from interferometers like VLTI and LBT. Some of the data that was simulated are shown in Figure 2.6. These data were used for speckle masking reconstruction with the direct bispectrum code we developed

(Surya and Saha, 2014). The results are discussed in Section 3.5.3. A major advantage of using multi-speckle data with speckle masking is that the baselines need not be non-redundant.

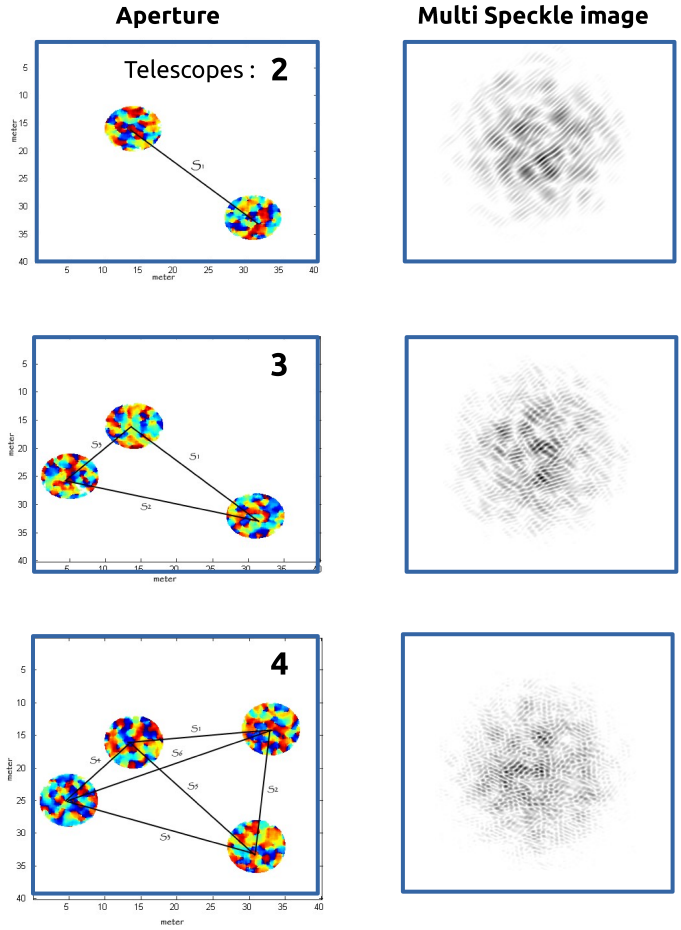

Figure 2.6: The simulated multi speckle images with different configurations of large telescope interferometers. (Top) The two telescope aperture configuration similar to LBT and the corresponding multi-speckle image. (Middle) 3 telescope aperture configuration and multi-speckle image. (Bottom) 4 telescope aperture configuration similar to VLTI and the corresponding multi-speckle image.

2.4.2.1 Steps in the simulation of multi-speckles

The procedure for the simulation of multi-speckles is as follows:

- First step is the simulation of the turbulent atmosphere phase distortions. Using the FFT method, discussed in the Section 2.3, we obtain the degraded phase screen across the interferometer aperture.
- Next we create the interferometer aperture, which are bounding masks that will be multiplied with the phase screen to obtain the phase distortions across the interferometer.
- The simulation of earth rotation aperture synthesis is also a key element of the process. The instantaneous projection of the interferometer pupil function as seen from the target object is simulated.
- A Fourier transform and modulus square operation of the pupil plane provides us the multi-speckled image.
- Photon noise is added to the obtained images from the simulation.

The simulated images of multi-speckles from different aperture configurations are shown in Figure 2.6.

2.4.3 Diluted Aperture Interferometers

Current optical interferometers are of 3-4 individual telescopes. Such interferometers use aperture synthesis and image reconstructions to obtain useful informations regarding the target object using fringe visibility and closure of phase measurements. A more useful step in future would be to achieve the capability of direct imaging. This requires the interferometer beams combined together coherently. One of the proposed models of achieving this is to use a large number of smaller mirror elements to built a dilute aperture interferometer. This will allow to increase the resolution drastically while keeping the mirrors small and easy to manufacture. The main issue with dilute aperture interferometers is the beam combination. If the light from

all the subpupils are combined in a normal Fizeau mode, it results in a PSF with a peak in the center but also has a dominant halo outside. A lot of the energy is dissipated in to these side lobes. This limits the usability of diluted aperture interferometers to image fainter stars. Several new beam combination schemes have been devised to go around this limitation. It has been an important aspect of our study to simulate these beam combination schemes for imaging interferometry. This is discussed in the next section.

2.4.4 Different types of beam combinations

The beam combination schemes directly affect the field of view in direct imaging interferometers. We have mainly studied 3 types of beam combination schemes which are expected to be used in the upcoming direct imaging interferometers.

- Fizeau beam combination
- Hypertelescope beam combination
- Interferometric Remapping Array Nulling (IRAN)

We have incorporated all these beam combinations in the simulation of optical interferometers. A detailed analysis of the three beam combination schemes have been done already by Lardière *et al.* (2007), Saha (2010) and Glindemann (2011). We would in the following section explain briefly about these beam combination schemes and the results of simulation of these beam combination schemes with our software.

2.4.4.1 Fizeau beam combination

Fizeau beam combination is a strict homothetic mapping beam combination where the ratio of baselines to subaperture diameter in the input baselines is same as the ratio in the output pupil. The entrance pupil of the interferometer is mapped on the exit pupil conserving the scale ratios, orientations and directions. This is the most natural form of beam combination. One of the

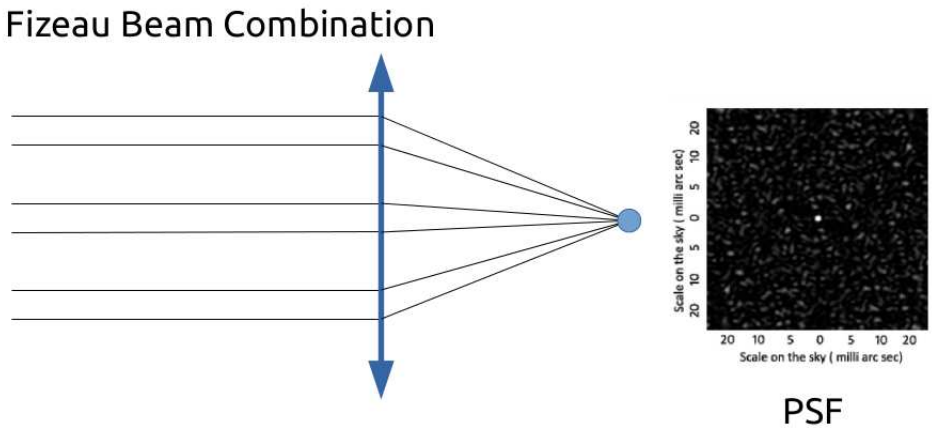

Figure 2.7: Layout of Fizeau beam combination and corresponding PSF

main advantages of a Fizeau beam combination is that it can be described by the incoherent space-invariant imaging equation

$$I(\boldsymbol{x}) = O(\boldsymbol{x}) * S(\boldsymbol{x}). \tag{2.11}$$

The PSF corresponding to the Fizeau beam combination is shown in Figure 2.7.

2.4.4.2 Hypertelescope beam combination

This type of beam combination was introduced by Labeyrie (1996). In such type of beam combination the exit-pupil is a densified copy of the entrance aperture. The centers of the exit pupil subapertures is same relative to input pupil but the size of the sub pupils are magnified. We define a parameter called 'pupil concentration coefficient' γ_d given by

$$\gamma_d = [d_o/D_o]/[d_i/D_i], \tag{2.12}$$

where D_i and d_i are entrance pupil diameters of array and the subaperture respectively. D_o and d_o are the corresponding diameters in the exit pupil. In a hypertelescope there is no position invariant PSF. The classical convolution is replaced by a 'pseudo-convolution' given below.

$$I(x) = \gamma_d^2.A(x).[O(x/\gamma_d) * I_0(x)], \tag{2.13}$$

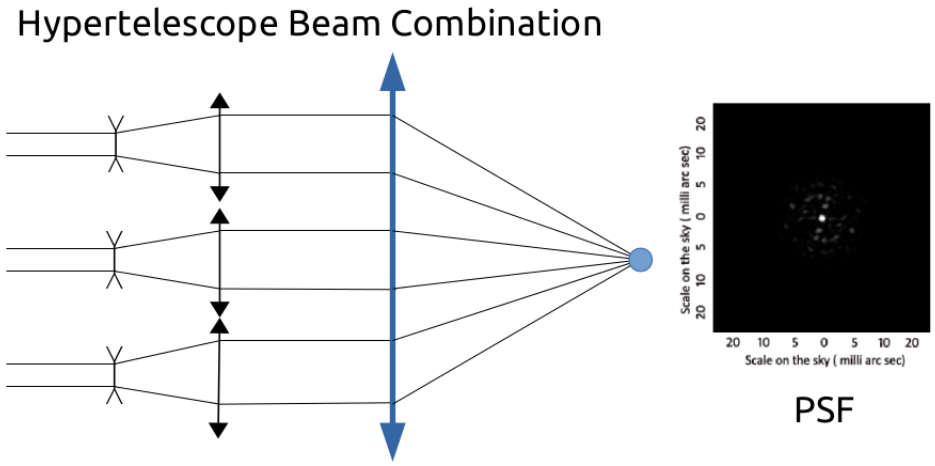

Figure 2.8: Layout of hypertelescope beam combination and corresponding PSF. The beam combination scheme uses small inverted Galilean telescopes in the exit pupil to densify the input pupil.

where $A(x)$ is the Airy diffraction envelope of the sub-pupil and I_0x is the interference function corresponding to the array. Figure 2.8 depicts the technique of hypertelescope beam combination. A detailed discussion regarding this is done in Chapter 5.

2.4.4.3 IRAN

The IRAN (Interferometric Remapped Array Nulling) beam combination was introduced by F. Vakili *et al.* (2004). This type of beam combination proposes, recording the interference in the pupil plane and not in the image plane. IRAN beam combination performs a non-pure homothetic remapping. An advantage of such a beam combination is that the moving Airy diffraction envelope is replaced by a top-hat envelope. The position of this envelope is independent of the position of the source. The PSF itself is translation invariant inside the top-hat. The imaging equation can be written as

$$I(x) = T(x).[O(x) * I_0(x)], \tag{2.14}$$

where $T(x)$ is the tophat envelope, $O(x)$ the object function and $I_0(x)$ the interference function. Figure 2.9 depicts the IRAN beam combination and

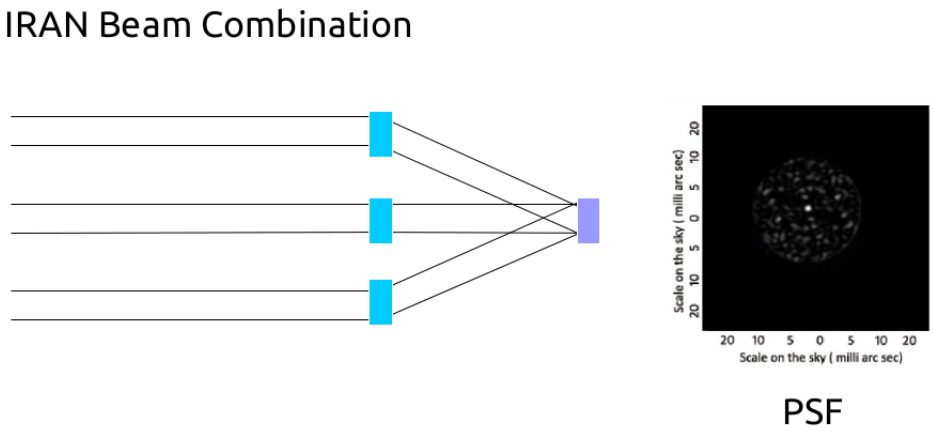

Figure 2.9: Layout of IRAN beam combination and corresponding PSF. The beam combination is done in this case in the image plane.

the corresponding PSF.

2.4.5 Comparison of all-in-one and pair-wise beam combination

At present most of the optical interferometric facilities follow the setup of several large telescopes $(1 - 8\ m)$ with few baselines. Aperture synthesis is used to cover the spatial frequency range. Beam combination geometry is also a major issue in determining the sensitivity of an interferometer. On one side we can have the pair-wise beam combination, in which, for an interferometer with n mirrors, beams are divided in to $n(n-1)$ sub-beams and pair-wise combined at $n(n-1)/2$ detectors. This is a common beam combination method used in todays interferometers. In such a setup there is one detector for each baseline. In the other side all the n beams can be combined in one detector. Such type of beam combination is called all-in-one beam combination. With the newer optical interferometers like hypertelescopes, which will use all-in-one beam combination, it is important to understand the gain in sensitivity that can be obtained from an all-in-one beam combination.

A basic idea in optical interferometry is that the co-addition of different

interferometric fringes obtained for different baselines should generate the image of the source (Menut *et al.*, 2008). The addition need not be done in Fourier space but can also be in image space. This process can give a lot of insights in to the problem of choice of all-in-one or pair-wise beam combination in future interferometers. It is well known that all-in-one combination gives an advantage over pair-wise beam combination because of the advantage it gives in terms of Signal to Noise Ratio due to lower photon noise effect. This is discussed in detail by Prasad and Kulkarni (1989); Roddier and Ridgway (1999); Nakajima (2001) and Labeyrie (2007). But we have done further basic simulations of our own to understand the results better.

2.4.5.1 One dimensional simulations for non-redundant apertures for cophased beam combinations

For this type of simulations we considered 1-dimensional array of δ functions with non-redundant baselines as our aperture. The visibility of the Point Spread Function from such an aperture in all-in-one combination will be the autocorrelation of the aperture itself. Thus visibility will have a central-peak, which is n times the secondary peaks. But if we take pair-wise fringes of each baseline in the aperture and add their visibilities we will have a central peak which is $n(n-1)$ times the secondary peaks. This is because each pairwise visibility will have a central peak which is 2 times the secondary. And we will add $\frac{n(n-1)}{2}$ such visibilities corresponding to each baseline. Thus finally our central peak will be $\frac{2.n.(n-1)}{2} = n(n-1)$ times the secondary peak.

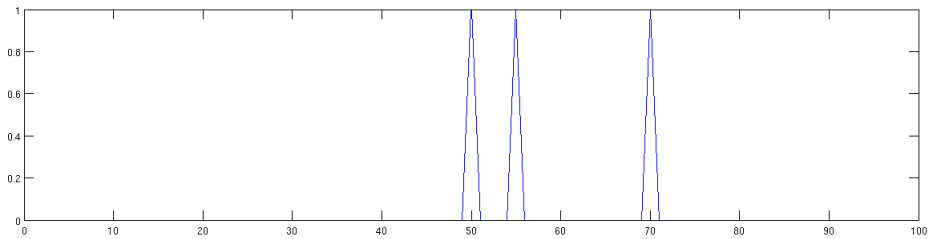

Figure 2.10: Three delta functions with non redundant baselines used as the aperture.

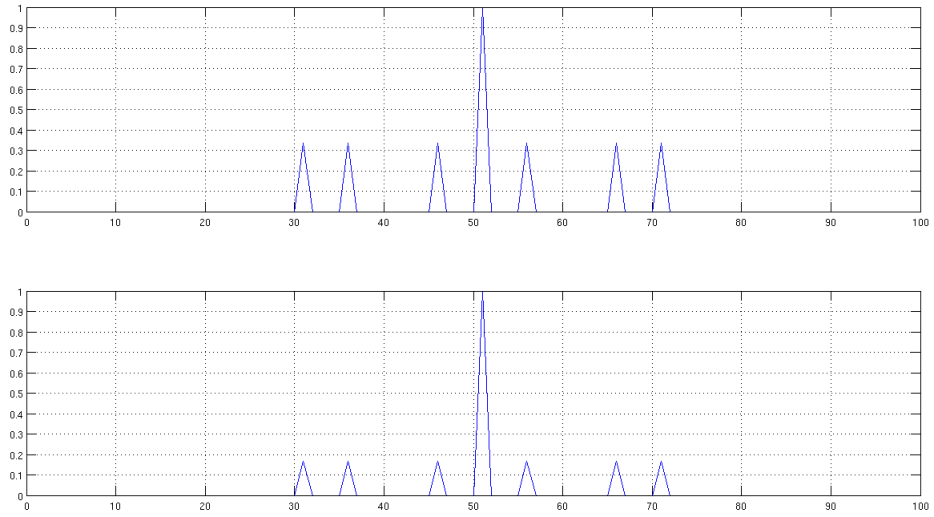

Figure 2.11: Visibity comparison 3 subapertures. (Top) The visibility of the all-in-one combination. The ratio (central-peak/secondary-peak) = n = 3. (Bottom) The visibility of combined pairwise combination, ie visibilities of each pair in aperture added together. The ratio (central-peak/secondary-peak) = n(n-1) = 6.

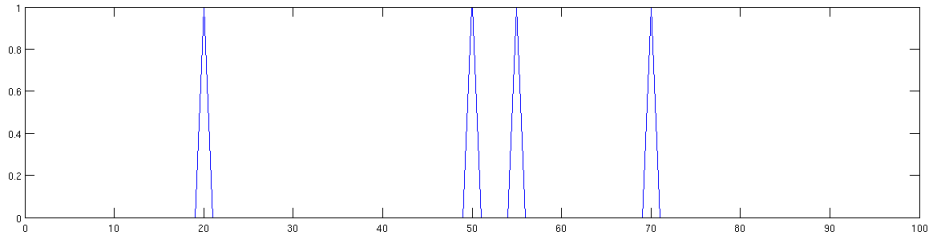

Figure 2.12: Four delta functions with non redundant baselines used as the aperture.

Consider $A(x, y)$, an interferometric array of δ-functions. The square of the Fourier transform will give the fringe system of the aperture if all-in-one beam combination is used.

$$I = |F(A)|^2. \tag{2.15}$$

Similarly if pairwise beam combination is considered,

$$I_k = |F(A_{ij})|^2 \tag{2.16}$$

is the equation of the k^{th} pair fringe from subapertures i and j. The pair-wise

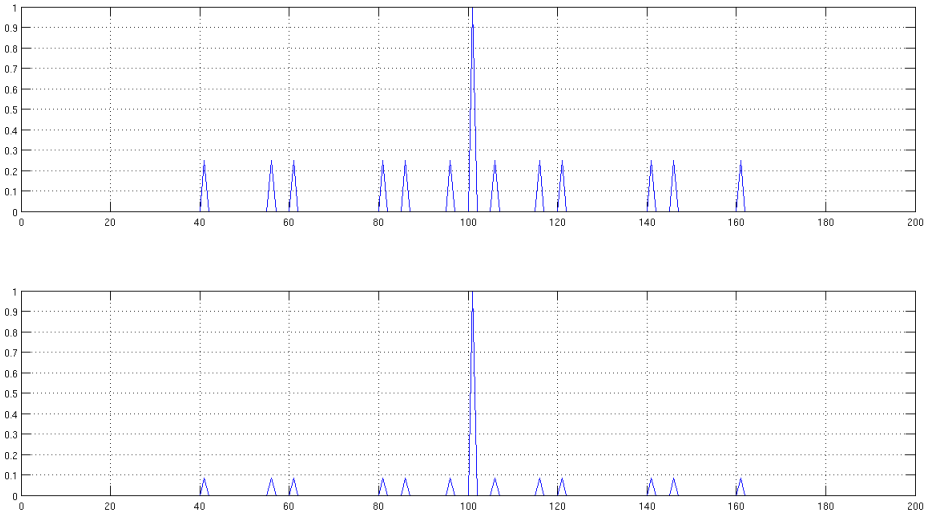

Figure 2.13: Visibility comparison for 4 subapertures. (Top) The visibility of the all-in-one combination. The ratio (central-peak/secondary-peak) = n = 4. (Bottom) The visibility of combined pairwise combination, ie visibilities of each pair in aperture added together. The ratio (central-peak/secondary-peak) = n(n-1) = 12.

combined image will be,

$$I = \sum_{k=1}^{n(n-1)/2} I_k. \tag{2.17}$$

We will then take the Fourier Transform of I to get the visibility.

$$V = F(I). \tag{2.18}$$

It can be proved that the ratio of central visibility to secondary peaks in a non redundant aperture will be as follows. For all-in-one beam combination,

$$\frac{CentralPeak}{SecondaryPeak} = n. \tag{2.19}$$

For pair-wise beam combination,

$$\frac{CentralPeak}{SecondaryPeak} = n(n-1). \tag{2.20}$$

For these simulations we used n= 3 to 10 with three different photon counts [240, 2400, 24000]. Photon noise was also added to the final fringes. For both the beam combination schemes the visibility was calculated and

visibility amplitude ratio was calculated. For all-in-one beam combination,

$$VisibilityRatio = \frac{SecondaryPeak \cdot n}{CentralPeak}. \tag{2.21}$$

For pair-wise beam combination,

$$VisibilityRatio = \frac{SecondaryPeak \cdot n(n-1)}{CentralPeak}. \tag{2.22}$$

We then compared the standard deviation of visibility ratio for all-in-one and pair-wise beam combination with different photon-count/mirror over 100 frames. The results are shown in the Figures 2.14, 2.15 and 2.16.

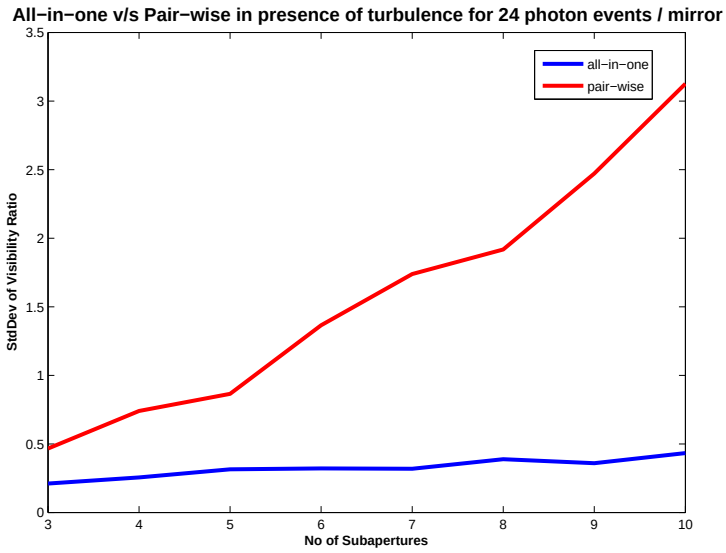

Figure 2.14: Standard deviation of visibility amplitude ratio calculated for 24 photon events per mirror.

From these basic 1-dimensional simulations it is easy to understand that all-in-one beam combination offers a greater signal to noise ratio compared to pair-wise recombination especially at low photon levels.

2.4.5.2 Two dimensional simulations of turbulence degraded images

We consider the 2 dimensional optical interferometer with N sub-apertures spread in a 2 dimensional plane. We also consider the effect of turbulence

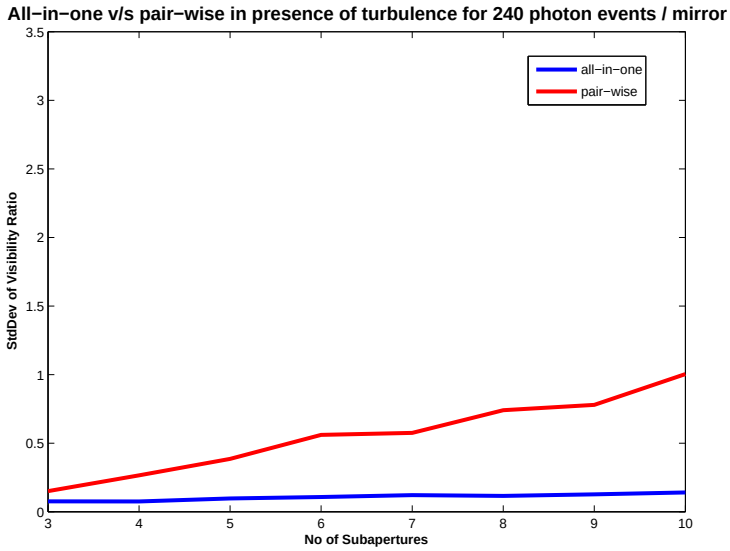

Figure 2.15: Standard deviation of visibility amplitude ratio calculated for 240 photon events per mirror

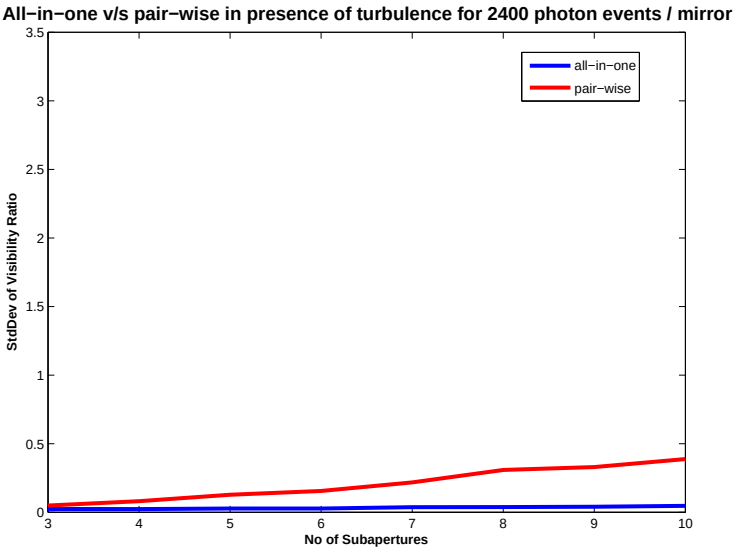

Figure 2.16: Standard deviation of visibility amplitude ratio calculated for 2400 photon events per mirror

across the subapertures. For the current study we consider the mirrors to be of size lesser than the r_0. In this type of setup we need to consider only piston errors introduced at each sub-aperture. One of the non phased fringe system for subapertures with positions (u_j, v_j) and (u_k, v_k) with corresponding piston

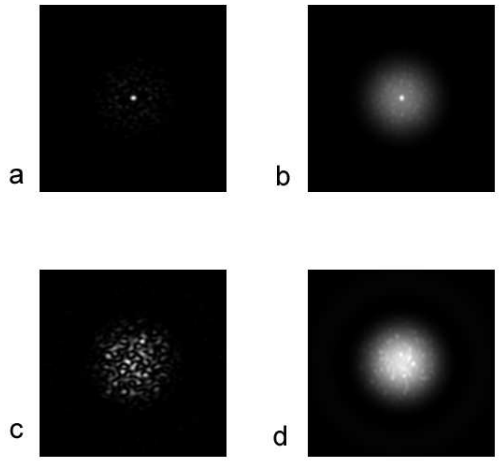

Figure 2.17: The point spread functions for all-in-one and pair-wise combination in cophased and non-phased cases. a) all-in-one cophased PSF b) pair-wise- combined cophased PSF c) all-in-one turbulence PSF d) pair-wise combined turbulence PSF.

errors ϕ_j and ϕ_k extracted from their corresponding positions in phase screen is given by,

$$I_{jk}(x,y) = A(x,y) \cdot \left| e^{-\frac{2\pi i}{\lambda z}(xu_j+yv_j)} \cdot e^{i\phi_j} + e^{-\frac{2\pi i}{\lambda z}(xu_k+yv_k)} \cdot e^{i\phi_k} \right|^2 . \tag{2.23}$$

with $A(x,y)$ being the Diffraction Function corresponding to subaperture give by,

$$A(x,y) = \left| \frac{2J_1(\rho R)}{\rho R} \right|^2 . \tag{2.24}$$

where $\rho = \frac{2\pi}{\lambda z}\sqrt{x^2+y^2}$ is the radial distance in reciprocal space,R is the radius of subaperture and z is the distance to image plane.

The pair-wise speckle PSF can be obtained by adding the individual fringe patterns of each baseline.

Pair-wise Combined Turbulence PSF : The summed non-cophased pairwise fringe systems which is curiously showing the speckles.

$$I(x,y) = \sum_{j=1}^{N}\sum_{k=1}^{N} A(x,y) \cdot \left| e^{-\frac{2\pi i}{\lambda z}(xu_j+yv_j)} \cdot e^{i\phi_j} + e^{-\frac{2\pi i}{\lambda z}(xu_k+yv_k)} \cdot e^{i\phi_k} \right|^2 \tag{2.25}$$

with $j \neq k$.

All-in-one Turbulence PSF: Normal speckle PSF with all-in-one beam combination is given by,

$$I(x,y) = A(x,y) \cdot \sum_{j=1}^{N} \left| e^{-\frac{2\pi i}{\lambda z}(xu_j + yv_j)} \cdot e^{i\phi_j} \right|^2 . \tag{2.26}$$

Figure 2.17 shows the cophased and speckle PSF's for pair-wise and all-in-one beam combination. As it is visible from the figure the pair-wise-combined PSF in both cases have less contrast.

Speckle Interferometry results with all-in-one and pair-wise beam combination : We used the all-in-one and pair-wise speckle PSF's generated by simulation as shown in Figure 2.17 to simulate the image of a binary star in both cases. One of the speckle image in each case is shown in Figure 2.18. We then used speckle interferometry to retrieve the auto-correlation of the binary star for each beam combination. The results are shown in Figure 2.19. We clearly observe from the Figure 2.19, that the correlation peaks

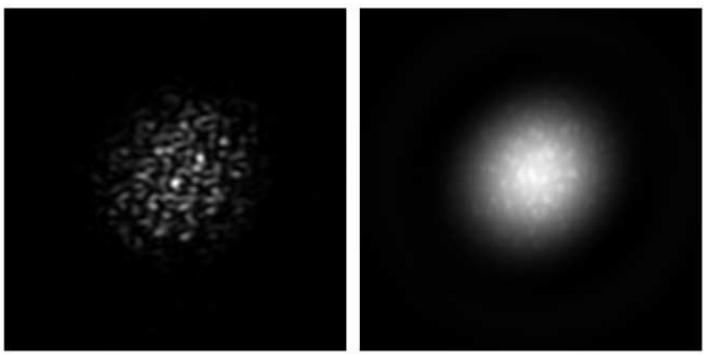

(a) All-in-one (b) Pair-wise

Figure 2.18: The speckle image of binary star: a) all-in-one snapshot image from array of 20 sub apertures with different atmospheric piston errors and b) image from co-addding pairwise fringe systems from the same array. The pair wise fringes were recorded same time across a single phase screen.

in pair-wise beam combination is very difficult to isolate from the background.

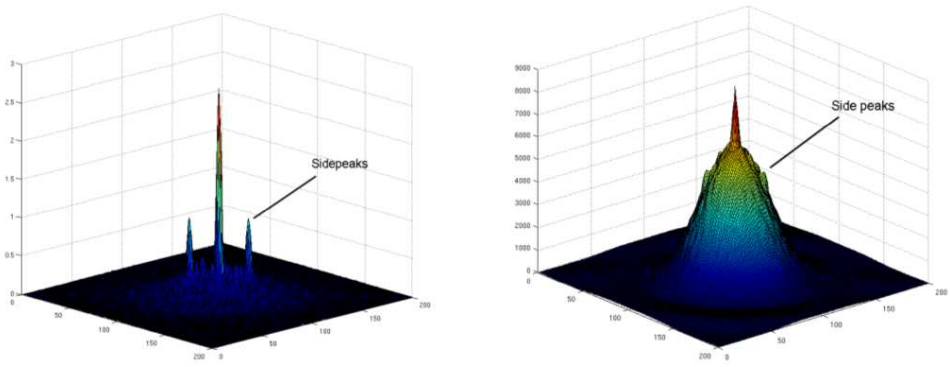

(a) All-in-one (b) Pair-wise

Figure 2.19: Autocorrelation of Binary Star with speckle interferometry: a) from all-in-one speckle images and b) from the co-added pair-wise-speckle-frames.

This clearly demonstrates that all-in-one is a clear choice for beam combination even in turbulence degraded imaging.

2.5 Conclusions

In this Chapter we have discussed the numerical algorithms to simulate different optical interferometers which use different techniques under various conditions. The methods to simulate atmospheric turbulence is very important in our study. The layer based model of the atmosphere and the methods to simulate it has been discussed in the first sections of the Chapter. Also the use of earth rotation aperture synthesis, to sample more of the spatial frequencies, is also studied and used in the simulations. Different types of interferometers are simulated in our study. These include large telescope optical interferometers with few baselines, masking the aperture of a single aperture telescope and diluted aperture interferometers called 'Hypertelescopes'.

In the case of optical interferometers the beam combination scheme also plays a very important role in determining the properties of imaging in terms of sensitivity. Two approaches of combining the beams in an optical interferometer is pair-wise combination and all-in-one combination. The simulations done by us indicate that all-in-one beam combination is superior in terms of

sensitivity both in cophased and non-cophased imaging.

In all-in-one beam combination there are different ways of beam combination methods used. The main beam combination methods that were simulated are Fizeau, IRAN and pupil densification. The simulation of different optical interferometers used with different beam combination schemes and under various atmospheric turbulence profiles gives the opportunity to undertake and analyze novel interferometric methods numerically.

Chapter 3

Triple Correlation Algorithm

3.1 Introduction

As we have already seen the resolution of a conventional telescope is not limited by diffraction. The affect of turbulent aperture is worse than diffraction. Typically the size of a turbulence cell is 10 cm. With this kind of turbulence we usually end up with an angular blur of 1 sec of arc. In spite of this we try to achieve diffraction limited imaging through various interferometric methods. One of the importent method is using speckle interferometry and triple correlation reconstruction. Speckle interferometry depends on short exposure images to freeze the phase perturbations over telescope aperture due to atmospheric turbulence. Such images consist of fine structures called speckles, each of which are of size of diffraction limit. They have high resolution object information, but the information itself is convolved with these random speckle spread functions. Triple correlation and speckle interferometry allows us to retrieve the high resolution information. In this chapter we try to understand the method of triple correlation and its use in retrieving turbulence degraded speckle images. The algorithm developed by Surya *et al.* (2014) will be also discussed with the results obtained with it on numerical simulations and real data.

3.2 Speckle interferometry

3.2.1 What is a Speckle?

The term 'speckle' refers to the grainy pattern observed when an uneven surface of an object is illuminated by a coherent source. A good example of speckle is in a swimming pool when many swimmers are present. Each swimmer creates water wavefronts and interference between these random wavefronts causes a speckled wave field on the water surface. Depending on the randomness of the source, spatial or temporal, speckles appear. Spatial speckles may be observed when all parts of the source vibrate at same constant frequency but with different amplitude and phase. With a non-monochromatic vibration spectrum, in the case of random sources of light, spatio-temporal speckles are produced.

3.2.2 Double Correlation and Power Spectrum

Double correlation analysis has been used in signal processing for a long time. We will analyze how such a second order analysis is advantageous in understanding key properties of the signal. Some of the interesting reasons for using ordinary double correlation are as follows.

Sometimes the original signal itself is not visible, but its autocorrelation is. For example the complex wave amplitude of light cannot be recorded since the frequencies are really high (10^{15} Hertz). But it is easy to perform a Fourier transform optically and to measure its modulus square.

A major application of auto correlation is in relation to speckle interferometry in astronomy. The signal in this case is the intensity in the image plane of the telescope. This signal fluctuates due to turbulence in atmosphere. The long time average of the image only contains lower frequencies while average power spectrum has bandwidth up to diffraction limit of the primary mirror, as we will see in the next sections. It must be admitted that we cannot infer everything about the signal from the autocorrelation.

3.2.3 Stellar speckle interferometry

Stellar speckle interferometry consists of taking many short exposure images of an object. Each such image will be the convolution of the instantaneous PSF of telescope and atmosphere, $S(\mathbf{x})$ with the actual object, $O(\mathbf{x})$. The intensity distribution $I(\mathbf{x})$ of the speckle interferograms, in the case of quasi-monochromatic incoherent source can be described by the following space-invariant imaging equation.

$$I(\mathbf{x}) = O(\mathbf{x}) * S(\mathbf{x}) \tag{3.1}$$

In a seminal paper in 1970 Antoine Labeyrie found out that diffraction limited amplitude information could be obtained from a series of speckle frames. In this paper he discussed the technique of averaging Fourier transformed images to obtain the object power spectrum, which runs as follows. The general imaging equation of a classical telescope in frequency domain is given by

$$\hat{I}(\mathbf{u}) = \hat{O}(\mathbf{u}).\hat{P}(\mathbf{u}), \tag{3.2}$$

where $\hat{P}(\mathbf{u})$ is the transfer function of the telescope. In speckle interferometry the image, $I(\mathbf{x})$ is Fourier transformed and its mod-square, $\left|\hat{I}(\mathbf{u})\right|^2$ is averaged over all frames. This averaged value can be written as

$$\langle\left|\hat{I}(\mathbf{u})\right|^2\rangle = \left|\hat{O}(\mathbf{u})\right|^2.\langle\left|\hat{P}(\mathbf{u})\right|^2\rangle \tag{3.3}$$

The function $\langle\left|\hat{P}(\mathbf{u})\right|^2\rangle$ is called the speckle interferometry transfer function and has a real non zero value up to the cutoff frequency of the telescope. By using a reference point star or modeling the atmosphere this function is estimated. Thus we can find out the object power spectrum

$$\left|\hat{O}(\mathbf{u})\right|^2 = \frac{\langle\left|\hat{I}(\mathbf{u})\right|^2\rangle}{\langle\left|\hat{P}(\mathbf{u})\right|^2\rangle} \tag{3.4}$$

And by inverse Fourier transform we obtain the object auto correlation. Figure 3.1 depicts the speckle images of 3 stars and their averaged powerspectrum. It was soon realized that the object phase information can be also

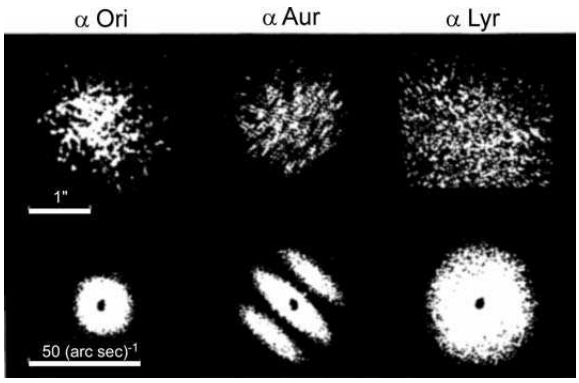

Figure 3.1: Speckle images (above) and corresponding spatial power spectra (below). From left to right, Betelgeuse (resolved disk), Capella (resolved binary) and an unresolved reference star. The power spectra are each the sums of about 250 frames (Labeyrie, 1970).

obtained from the speckle images. In the binary star speckle images the alignment of the binary stars was almost visible. But the techniques to extract phase information from these images was not yet developed then. It was later in 1974 that the Knox-Thompson technique was developed which really gave the ability to extract phase information. But a btter method was discovered even later by Weigelt (1977) called speckle masking or speckle imaging, which was an image plane version of phase closure method (Jennison, 1958) used in radio astronomy. Speckle masking still remains the best method to date for phase recovery. Several variations of the method has been developed which decreased computational time and improved the reconstruction.

We have simulated numerically speckle interferometric observations with diluted aperture arrays. These results are shown in Figure 3.2. The apertures used were diluted apertures with 17 and 50 mirrors.

3.3 Triple Correlation

While second order correlation has several advantages over third order correlation, one being that it takes very less storage space and computing time to handle, it does come with the handicap of missing out on phase reconstruc-

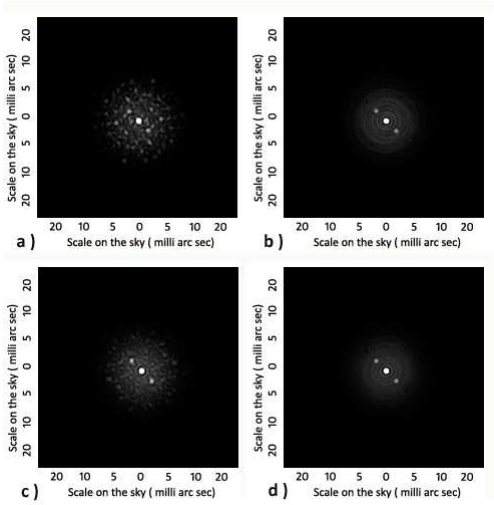

Figure 3.2: Speckle interferometry reconstruction simulation of a binary star. The images are autocorrelations of the binary stars retrieved from speckle images from a 17 and 50 mirror array with and without earth rotation aperture synthesis. a) Binary star autocorrelation retrieved from speckles images of 17 mirror array, b) binary star autocorrelation retrieved from speckles images of 17 mirror array with aperture rotation of 8 hours, c) binary autocorrelation retrieved from speckles images of 50 mirror array and d) binary star autocorrelation retrieved from speckles images of 50 mirror array with aperture rotation of 8 hours.

tion. Thus, the next step in speckle based reconstruction was to use triple correlation based reconstructions.

An importent property of triple-correlation that gives it its advantage is that it is possible to deduce the signal, $I(\boldsymbol{x})$ uniquely from its triple correlation, $I^{(3)}(\boldsymbol{x_1}, \boldsymbol{x_2})$.

3.3.1 Basic Properties of Triple Correlation

One of the earliest references on Triple correlation is Brillinger (1975). A lot of the properties of triple correlation has also been discussed by Lohmann and Wirnitzer (1984). Some of the main properties of triple correlation is given below.

- The auto triple correlation is defined as

$$I^{(3)}(\mathbf{x}_1, \mathbf{x}_2) = \int_{-\infty}^{+\infty} I(\mathbf{x})I(\mathbf{x}+\mathbf{x}_1)I(\mathbf{x}+\mathbf{x}_2)d\mathbf{x}. \tag{3.5}$$

- The Fourier transform of triple correlation is bispectrum and is related to the signal spectrum as

$$\widehat{I}^{(3)}(\mathbf{u}_1, \mathbf{u}_2) = \widehat{I}(\mathbf{u}_1)\widehat{I}^*(\mathbf{u}_1+\mathbf{u}_2)\widehat{I}(\mathbf{u}_2). \tag{3.6}$$

- The bispectrum is 3/4 redundant due to the two inherent symmetries

$$\widehat{I}^{(3)}(\mathbf{u}_1, \mathbf{u}_2) = \widehat{I}^{(3)}(\mathbf{u}_2, \mathbf{u}_1) = \widehat{I}^{(3)}(-\mathbf{u}_1-\mathbf{u}_2, \mathbf{u}_1). \tag{3.7}$$

- If the signal is real both signal spectrum and bispectrum are Hermitian.

$$\widehat{I}(\mathbf{u}) = \widehat{I}^*(-\mathbf{u}). \tag{3.8}$$

$$\widehat{I}^{(3)}(\mathbf{u}_1, \mathbf{u}_2) = \widehat{I}^{(3)*}(-\mathbf{u}_1, -\mathbf{u}_2). \tag{3.9}$$

  In which case only one angular octant of the bispectrum is non redundant.

- If a system acts linear and time invariant upon the signal $I(\boldsymbol{x})$, then it also acts linear and time invariant for the triple correlation $I^{(3)}(\boldsymbol{x}_1, \boldsymbol{x}_2)$.

$$I_o(\mathbf{x}) = \mathbf{I_i}(\mathbf{x}) * \mathbf{S}(\mathbf{x}). \tag{3.10}$$

$$\widehat{I}_o(\mathbf{u}) = \widehat{\mathbf{I}}_\mathbf{i}(\mathbf{u}).\widehat{\mathbf{S}}(\mathbf{u}). \tag{3.11}$$

$$\widehat{I}_o^{(3)}(\mathbf{u}_1, \mathbf{u}_2) = \widehat{I}_i^{(3)}(\mathbf{u}_1, \mathbf{u}_2).\widehat{S}_i^{(3)}(\mathbf{u}_1, \mathbf{u}_2). \tag{3.12}$$

  Multiplication in Fourier domain corresponds to convolution in time domain. Thus we can also write the equaion in time domain as,

$$I_o^{(3)}(\mathbf{x}_1, \mathbf{x}_2) = I_i^{(3)}(\mathbf{x}_1, \mathbf{x}_2) * S_i^{(3)}(\mathbf{x}_1, \mathbf{x}_2). \tag{3.13}$$

The bispectrum and triple correlation of two simple objects are shown in Figure 3.3 and Figure 3.4.

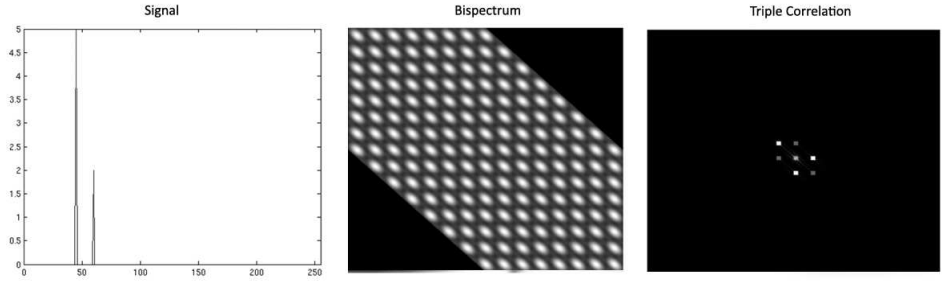

Figure 3.3: (Left) One dimensional binary star object, (Center) corresponding 2-dimensional bispectrum, (Right) corresponding triple correlation.

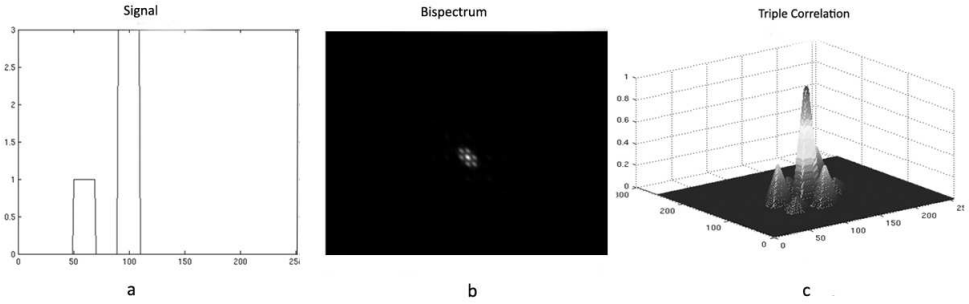

Figure 3.4: (Left) One dimensional extended binary star object, (Center) corresponding 2-dimensional bispectrum, (Right) corresponding triple correlation.

3.3.2 Limitations of signal retrieval from triple correlation

Using the definition of bispectrum we find that bispectrum is immune to a factor of $e^{\beta.\mathbf{u}}$, i.e. for

$$\widehat{I}_F(\mathbf{u}) = \widehat{I}(\mathbf{u}).e^{\boldsymbol{\beta.u}}, \tag{3.14}$$

$$\widehat{I}_F^{(3)}(\mathbf{u}_1, \mathbf{u}_2) = \widehat{I}(\mathbf{u}_1)\widehat{I}^*(\mathbf{u}_1 + \mathbf{u}_2)\widehat{I}(\mathbf{u}_2).e^{\mathbf{fi}.[\mathbf{u_1}+\mathbf{u_2}-\mathbf{u_1}-\mathbf{u_2}]} = \widehat{I}^{(3)}(\mathbf{u}_1, \mathbf{u}_2). \tag{3.15}$$

Another class of signals that cannot be reconstructed from triple correlation are those with skewness of zero. Or in other words signals whose triple correlation is zero.

3.3.3 The generalized speckle masking transfer function

We now try to formulate the speckle masking transfer function in triple correlation. For the following analysis consider the signal to be one-dimensional. Transfer function $\widehat{S}_n(u)$ of the incoherent image forming system is the autocorrelation of the pupil function $\widehat{H}(\xi)$.

$$\widehat{S}_n(u) = \int \widehat{H}(\xi)\widehat{H}^*(\xi' + \xi)d\xi' = \int \widehat{H}(\lambda f u')\widehat{H}^*(\lambda f u' + \lambda f u)d\xi', \quad (3.16)$$

where the variable ξ denotes the coordinate in the telescope pupil and is related to the spatial frequency by $\xi = \lambda f u$. With the scaled pupil function $H(u') = \widehat{H}(\lambda f u')$,

$$\widehat{S}_n(u) = \int H(u')H^*(u'' + u)du'. \quad (3.17)$$

In astronomical imaging the function $H(u')$ can be split in to one representing pupil function and one representing effect of random media.

$$H(u') = H_0(u').A(u), \quad (3.18)$$

where $A(u)$ can be considered to be a stationary random variable. Substitution of equation 3.18 to equation 3.17 gives,

$$\widehat{S}_n(u) = \int A(u').A^*(u'' + u).H_0(u')H_0{}^*(u'' + u)du'. \quad (3.19)$$

The transfer function of long exposure can be found out using ensemble average of $\widehat{S}_n(u)$. In case of large telescopes $\langle\widehat{S}_n(u)\rangle$ falls to zero much lower frequencies than the telecope cutoff frequencies. For triple correlation, the transfer function concerned is,

$$\widehat{S}_n^{(3)}(u,v) = \int\int\int H_0(u')H_0{}^*(u''+u)H_0(v')H_0{}^*(v''+v)H_0(w)H_0{}^*(w-u-v) \langle A(u')A^*(u''+u)A(v')A^*(v''+v)A(w)A^*(w-u-v)\rangle du'dv'dw. \quad (3.20)$$

In order to calculate the sixth order moment, we assume that real and imaginary parts of $A(w)$ have zero mean Gaussian distribution. For a complex Gaussian process the momentum theorem can be used to show that,

$$\begin{aligned}\langle A_1 A_2^* A_3 A_4^* A_5 A_6^* \rangle = \langle A_1 A_2^* \rangle \langle A_3 A_4^* A_5 A_6^* \rangle + \langle A_1 A_2^* A_3 A_4^* \rangle \langle A_5 A_6^* \rangle + \\ \langle A_1 A_2^* A_5 A_6^* \rangle \langle A_3 A_4^* \rangle - 2\langle A_1 A_2^* \rangle \langle A_3 A_4^* \rangle \langle A_5 A_6^* \rangle + \\ \langle A_1 A_4^* \rangle \langle A_3 A_6^* \rangle \langle A_5 A_2^* \rangle + \langle A_1 A_6^* \rangle \langle A_3 A_2^* \rangle \langle A_5 A_4^* \rangle.\end{aligned} \tag{3.21}$$

Since the complex amplitude is $A(u)$ is stationary random variable, its autocorrelation function may be defined by,

$$\langle A(u') A^*(u'' + u) \rangle = C_A(u). \tag{3.22}$$

Since for usual seeing conditions the complex amplitude $A(u)$ can be a fine structure compared to telescope aperture, $A(u)$ can be assumed to be δ correlated, i.e. $C_A(u) = const.\delta(u)$. Substitution yields,

$$\begin{aligned}\langle \widehat{S}_n^{(3)}(u,v) \rangle = \langle \widehat{S}_n(u). \rangle \langle \widehat{S}_n(v) \widehat{S}_n(-u-v) \rangle + \\ \langle \widehat{S}_n(u). \widehat{S}_n(v) \rangle \langle\ \widehat{S}_n(-u-v) \rangle + \\ \langle \widehat{S}_n(u) \rangle \langle \widehat{S}_n(v). \widehat{S}_n(-u-v) \rangle - \\ 2\langle \widehat{S}_n(u) \rangle . \langle \widehat{S}_n(v) \rangle \langle\ \widehat{S}_n(-u-v) \rangle + \\ const. \widehat{B}^{(3)}(u,v),\end{aligned} \tag{3.23}$$

where,

$$\widehat{B}^{(3)}(u,v) = \int |H_0(w)|^2 . |H_0(w+u+v)|^2 x [|H_0(w+u)|^2 + |H_0(w+v)|^2]^2 dw. \tag{3.24}$$

The term $\widehat{B}^{(3)}(u,v)$ depends on the modulus square of the pupil function. Thus it is independent of image degradation and telescopic aberrations. It is also positive and non zero for all frequencies up to diffraction limit of the telescope.

3.4 Image reconstruction from Bispectrum

3.4.1 Theory

The triple correlation technique developed by Lohmann *et al.* (1983) runs as follows. The object speckle pattern $I(\mathbf{x})$, is multiplied with an appropriately

shifted version of it, i.e. $I(\mathbf{x}+\mathbf{x}_1)$. The result is then correlated with $I(\mathbf{x})$.

$$I^{(3)}(\mathbf{x}_1,\mathbf{x}_2) = \langle \int_{-\infty}^{+\infty} I(\mathbf{x})I(\mathbf{x}+\mathbf{x}_1)I(\mathbf{x}+\mathbf{x}_2)d\mathbf{x}\rangle, \tag{3.25}$$

where, $\mathbf{x}_j = x_{jx} + x_{jy}$ is the 2-dimensional spatial co-ordinate vector. $\langle\rangle$ stands for ensemble average. The Fourier transform of the triple correlation is called bispectrum and its ensemble average is given by,

$$\langle \widehat{I}^{(3)}(\mathbf{u}_1,\mathbf{u}_2)\rangle = \langle \widehat{I}(\mathbf{u}_1)\widehat{I}^*(\mathbf{u}_1+\mathbf{u}_2)\widehat{I}(\mathbf{u}_2)\rangle \tag{3.26}$$

where, $\widehat{I}(\mathbf{u}) = \int I(\mathbf{x})e^{-i2\pi\mathbf{u}.\mathbf{x}}d\mathbf{x}$, $\widehat{I}^*(\mathbf{u}_1+\mathbf{u}_2) = \int I(\mathbf{x})e^{i2\pi(\mathbf{u}_1+\mathbf{u}_2).\mathbf{x}}d\mathbf{x}$, $\mathbf{u}_j = u_{jx} + u_{jy}$. In the second order moment, phase of the object's Fourier transform is lost. But in the third order moment or in the bispectrum, it is preserved. The argument of equation 3.26 can be expressed as,

$$arg \mid \widehat{I}^{(3)}(\mathbf{u}_1,\mathbf{u}_2) \mid = \phi_b(\mathbf{u}_1,\mathbf{u}_2) = \phi(\mathbf{u}_1) - \phi(\mathbf{u}_1+\mathbf{u}_2) + \phi(\mathbf{u}_2) \tag{3.27}$$

Equation 3.27 gives the phase of the bispectrum. Observed image is the convolution of the object and the point spread function (PSF) of the combination of telescope and the atmosphere. Its Fourier transform is the product of the Fourier transform of the object and the transfer function of the telescope and the atmosphere.

$$\widehat{I} = \widehat{O}(\mathbf{u}) \cdot \widehat{S}(\mathbf{u}) \tag{3.28}$$

Using equations 3.28 into equation 3.26 we can write,

$$\langle \widehat{I}^{(3)}(\mathbf{u}_1,\mathbf{u}_2)\rangle = \widehat{O}(\mathbf{u}_1)\widehat{O}^*(\mathbf{u}_1+\mathbf{u}_2)\widehat{O}(\mathbf{u}_2)\langle \widehat{S}(\mathbf{u}_1)\widehat{S}^*(\mathbf{u}_1+\mathbf{u}_2)\widehat{S}(\mathbf{u}_2)\rangle. \tag{3.29}$$

Thus the image bispectrum is the product of object bispectrum and bispectrum transfer function, $\langle \widehat{S}(\mathbf{u}_1)\widehat{S}^*(\mathbf{u}_1+\mathbf{u}_2)\widehat{S}(\mathbf{u}_2)\rangle$. It has been proved elsewhere (Lohmann *et al.*, 1983) that this transfer function is real. Thus the phase values of the averaged image bispectrum are equal to that of the object bispectrum. This allows the opportunity to extract real phase information from the object bispectrum. The modulus $\mid \widehat{O}(\mathbf{u}) \mid$ and phase $\phi(\mathbf{u})$ of the object Fourier transform $\widehat{O}(\mathbf{u})$ can be derived from the object bispectrum $\widehat{I}_O^{(3)}(\mathbf{u}_1,\mathbf{u}_2)$. The object phase-spectrum is thus encoded in the term $e^{i\phi_b(\mathbf{u}_1,\mathbf{u}_2)} = e^{i[\phi(\mathbf{u}_1)-\phi(\mathbf{u}_1+\mathbf{u}_2)+\phi(\mathbf{u}_2)]}$.

Equation 3.27 is a recursive equation for evaluating the phase of the object Fourier transform at coordinate $\mathbf{u} = \mathbf{u}_1 + \mathbf{u}_2$. The phase of the bispectrum is recursive in nature and the object phase-spectrum at $(\mathbf{u}_1 + \mathbf{u}_2)$ can be expressed as,

$$\phi(\mathbf{u}_1 + \mathbf{u}_2) = \phi(\mathbf{u}) = \phi(\mathbf{u}_1) + \phi(\mathbf{u}_2) - \phi_b(\mathbf{u}_1, \mathbf{u}_2) \tag{3.30}$$

If the object spectrum at $\mathbf{u}_1$ and $\mathbf{u}_2$ are known, the object phase-spectrum at $(\mathbf{u}_1 + \mathbf{u}_2)$ can be computed. Thus Triple correlation technique provides a very good method of obtaining the Fourier phase of the object distribution. Modified version of the same technique is also applied to extract information from closure of phase measurements.

3.4.2 Direct Bispectrum Algorithm

Using triple correlation based recursive technique we have developed a code in MATLAB to process images degraded by atmospheric turbulence. The code works on 2-dimensional images and uses its corresponding 4-dimensional bispectrum to recover the Fourier phase information of the object. The direct bispectrum code can process 200 x 200 pixels images of 300 frames in 15 minutes in an Intel i5 computer with 4 GB of RAM. The unit amplitude phasor method, used in algorithms by Sridharan (2000), is applied in the code for phase reconstruction. The code uses direct computation of the 4-dimensional bispectrum $I^{(3)}(u, v, u^{'}, v^{'})$, which demands large amount of computer memory. The 4-D bispectrum is computed and averaged out for all the speckle frames. The retrieved Fourier phase from bispectrum is then combined with Fourier amplitude from speckle interferometry to reconstruct the object. The steps in the developed algorithm is as follows

1. Convert each of the speckle image $I_1(x, y), I_2(x, y), I_3(x, y)..$ in to its Fourier Transform $\widehat{I}_1(u, v), \widehat{I}_2(u, v), \widehat{I}_3(u, v)..$

2. Find the averaged bispectrum $\langle \hat{I}^{(3)}(u_1, u_2, u_3, u_4) \rangle$ over all frames.

3. Retrieve the Fourier phase $\phi(u)$ of the object projection from the averaged bispectrum using recursion formula used in equation 3.30.

4. Retrieve the Fourier amplitude of the object from the averaged power spectrum $\langle \hat{I}^{(2)}(u_1, u_2) \rangle$ using classical speckle interferometry.

5. Combine the Fourier phase and amplitude to recreate the true object image.

3.5 Results

In this section we will discuss some of the results we have obtained from the direct bispectrum algorithm reconstruction of real speckle images and numerical simulations.

3.5.1 Results with real images

The developed algorithm was used with images of β Coronae Borealis (HR5747) taken on 16 and 17 March 1990 from the 2.34 meter Vainu Bappu Telescope (VBT) in Kavalur using a speckle camera system developed by Saha et al. 1997, the description of which is given below. VBT has two accessible foci for backend instrumentation, such as a prime focus (f/3.25 beam) and a cassegranian focus (f/13 beam). The latter has an image scale of 6.7 arcseconds per mm, which was further slowed down to ∼1.21 arcseconds per mm, using a Barlow lens arrangement. This enlarged image was recorded through a 5nm filter centered on H using an EEV uncooled intensified CCD (ICCD) (Chinnappan et al.,1991) camera with exposure times of 20 ms (Saha *et al.*, 1999). The interface between the intensifier screen and the CCD chip is a fiber-optic bundle which reduces the image size by a factor of 1.69. A Data Translation^{TM} frame-grabber card DT-2851 digitizes the video signal. This digitizer re-samples the pixels of each row (385 CCD columns to 512 digitized samples) and introduces a net reduction in the row direction of a factor of 1.27. The video frame grabber cards digitize and store the images in the

memory buffer of the card. The available frame grabber could store upto two interlaced frames images on its onboard memory. These images are then written onto the hard disc of a personal computer. The observing conditions were fair with an average seeing of 2 arcseconds during the nights of 16/17 March 1990. The binary star was earlier resolved using Blind Iterative Deconvolution (BID) technique (Saha & Venkatakrishnan, 1997) and the seperation was found to be 0.20 arcsecond and magnitude difference of 1.65. The results of direct bispectrum on the same speckle images gave results that show a separation of 0.21 arcseconds. This is shown in Figure 3.5. The position angles and separations of the binary components were seen to be consistent with results of the auto-correlation technique and with the published observations of the binary orbit of HR5747 (Labeyrie *et al.*, 1974).

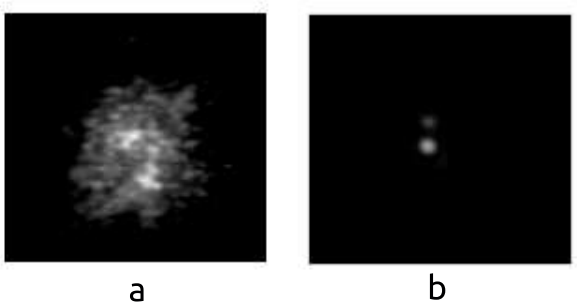

Figure 3.5: Reconstruction from speckle images of β Coronae Borealis (HR5747): a) one of the speckle images of HR5747, b) the reconstructed image using direct bispectrum algorithm (Surya and Saha, 2014).

3.5.2 Results with Aperture Masking Simulations

In Chapter 2 we have discussed the process of simulating aperture masking. It is an important technique used quite often with speckle based reconstruction techniques. It is also easy to implement with the current single aperture telescopes. In our study of triple correlation based reconstructions, we have carried out numerical simulations of speckle imaging with aperture masks, having randomly arranged subapertures. The baselines used in the simula-

tions were non-redundant. For this simulation we considered a mask with non redundant aperture of 17 holes. The aperture is shown in Figure 3.6.

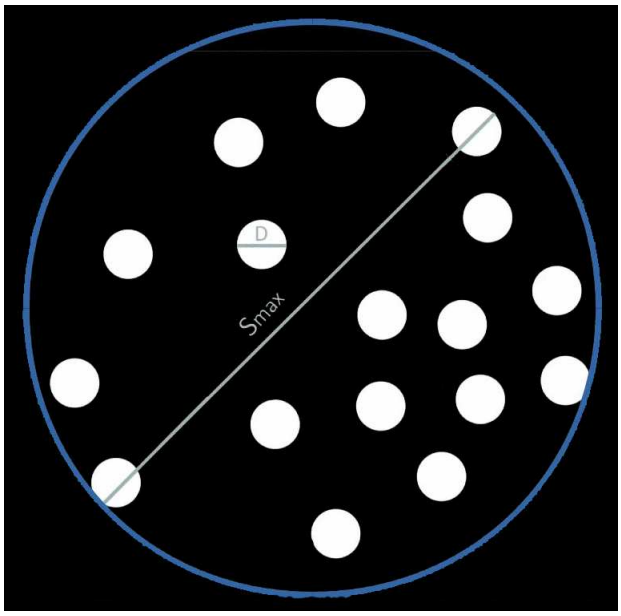

Figure 3.6: The aperture used for the simulation

For the numerical simulations we considered the maximum baseline of the mask S_{max} to be 1 m and the minimum baseline between the subapertures as 20 cm. The diameter of the subaperture D is 10 cm. The atmospheric piston errors of subapertures were taken from the Kolmogorov phase screen of Fried parameter 20 cm which was been simulated using the Fast Fourier Transform based power density method (Lane *et al.*, 1992). This algorithm is discussed in Section 2.2.3. The phase screens were moved with a wind velocity of 10 m/s between successive speckle frames to simulate seeing changes in real conditions. All the major parameters of the simulation are shown in Table 3.1.

The results of the speckle simulations from such an aperture for a binary star and a sextuple star group is shown in Figure 3.7 and Figure 3.8. As seen from the figure we were able to reconstruct the binary star and sextuple star with good signal. A detailed study of the quality of reconstruction is done in chapter 4. The sparse nature of the aperture affects the reconstruction. The same aperture with earth rotation aperture synthesis is used to produce speckle imaging reconstructions as shown in figure 3.8. When

Frames used in speckle masking	100
Plate scale for each frame	0.2 arc sec /pixel
Wavelength	500 nm
Fried Parameter	0.2 m
Wind Velocity	10 m/s
Maximum Baseline	1 m
Minimum Baseline (between subapertures)	20 cm
Diameter of subaperture	10 cm

Table 3.1: Parameters used in the numerical simulations of aperture masking speckle imaging

speckle frames from different time of the night were used, the time-dependent bispectrum, $I_i^{(3)}(u, v, u', v', t_i)$, of each frame was computed and averaged. From the averaged bispectrum, $\sum I_i^{(3)}(u, v, u', v', t_i)$, the image of the object was reconstructed. The averaged bispectrum contains the u-v coverage as sampled through the night by earth rotation and hence provides a better reconstruction of object phase.

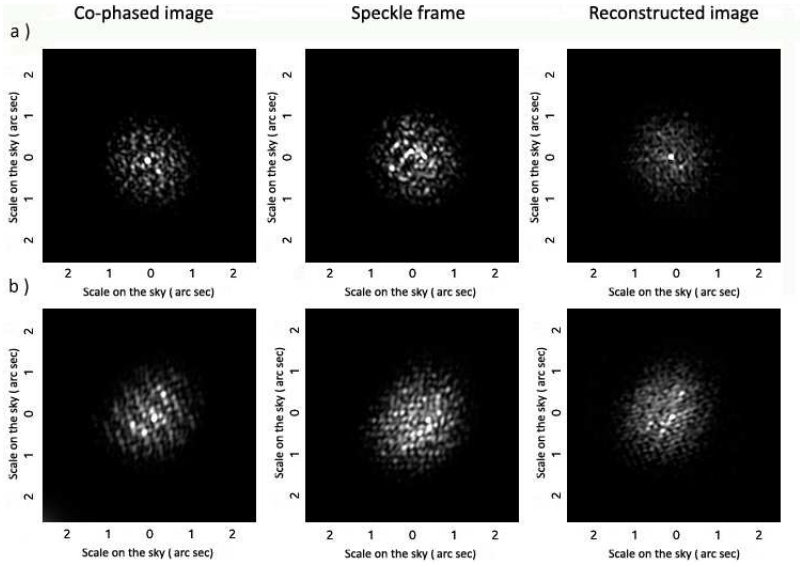

Figure 3.7: Speckle Reconstruction using direct bispectrum from simulations of 17-hole aperture masking: a) binary star, b) six star group.

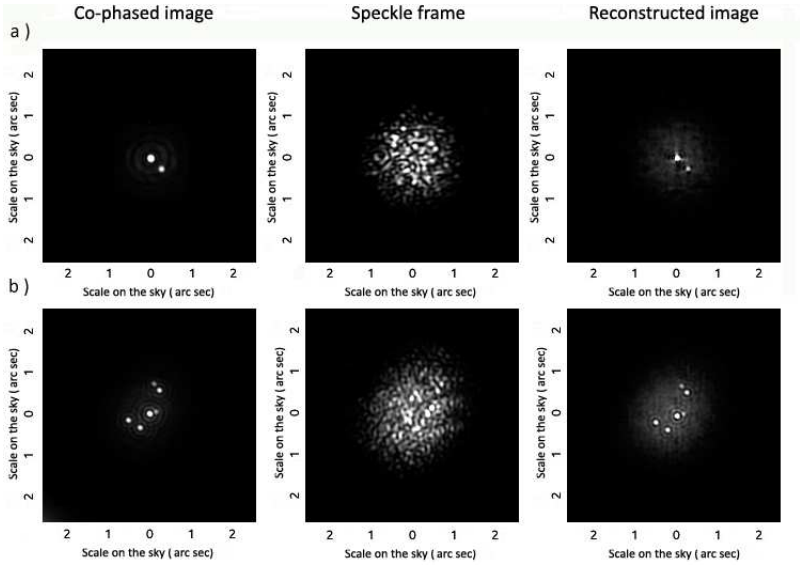

Figure 3.8: Speckle Reconstruction using direct bispectrum from simulations of 17-hole aperture masking using images taken at equal intervals through the night over 8 hrs: a) binary star. b) six star group.

3.5.3 Results with Multispeckle Simulations

We have discussed about simulations of multi-speckle observations in long baseline interferometers like VLTI and LBT in Section 2.4.2. We have also shown the multispeckle images produced from different configurations of large interferometers in Figure 2.6. These images were processed by the direct bispectrum algorithm to obtain reconstructions. Just as in aperture masking simulations, when speckle frames from different time of the night were used, the time-dependent bispectrum, $I_i^{(3)}(u, v, u', v', t_i)$, of each frame was computed and averaged before reconstruction. In Figure 3.9 it is clearly shown that such use of earth rotation with speckle imaging can work sucessfully even with multi speckles. The binary star which is unresolved by a single aperture speckle imaging gets resolved by using multi-speckle reconstruction with two apertures. Figure 3.10 shows the reconstructions together with the multi-speckle image.

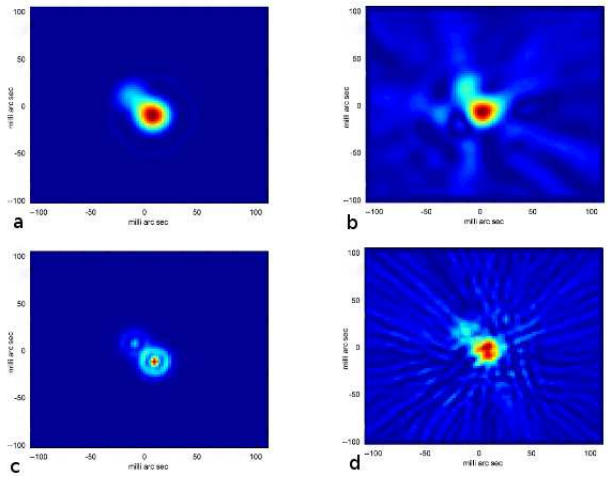

Figure 3.9: Multi-speckle reconstruction of binary star: a) cophased image of binary star with single aperture, b) reconstructed image of binary star from speckles images from single aperture, c) cophased image of binary star averaged by earth rotation synthesis in a 2 telescope interferometer, d) reconstructed image of binary star from multi speckles of the same two telescope interferometer using earth rotation.

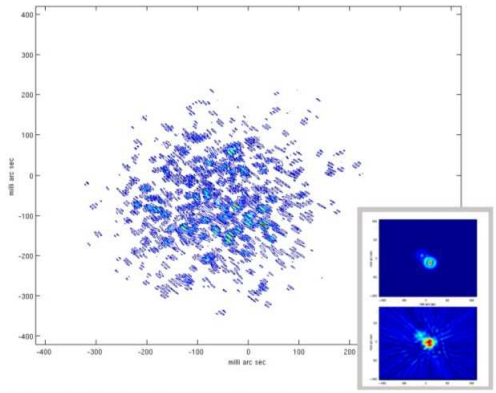

Figure 3.10: Multi-speckle reconstruction using direct bispectrum algorithm: (Left) the multispeckle image from a 2-telescope interferometer, (Sidebox Top) the ideal image as obtained by aperture rotation of two telescope interferometer through 8 hrs with out considering atmospheric turbulence, (Sidebox Bottom) the reconstructed image from the multi-speckle images of the 2-telescope interferometer taken at different times during 8 hrs.

3.6 Conclusions

Triple correlation based speckle reconstruction is a very useful technique in high resolution astronomy. We have developed our own direct bispectrum algorithm to reconstruct object from speckle images. The algorithm uses the phase-retaining properties of triple correlation. The developed algorithm has been used with reconstruction of Coronae Borealis. The code has been also used together with aperture masking simulations and with the multi speckle simulations. It has given fruitful results with these simulations and is also able to reconstruct images utilizing earth rotation aperture synthesis. The rotation of the earth is used in such a technique to fill the gaps in the spatial frequency coverage of an interferometer. The direct bispectrum code developed is computationally very expensive. It uses a lot of memory and computational time. In the next chapter we discuss about the Radon transform based tomographic speckle masking algorithm, which has reduced the computational time considerably.

Chapter 4

Tomographic Speckle Masking

4.1 Introduction

Triple Correlation technique and other advanced image retrieval methods have been developed to allow the reconstruction of the Fourier phase information. Such algorithmic techniques retrieve diffraction limited information from the short exposure images. The advantages of this technique is in providing information about the object phases with better signal to noise ratio (SNR). The disadvantage of this technique is that it demands very large computational resources with 2-dimensional data since the calculations are 4-dimensional. It requires extensive evaluation-time and data storage requirements, even if the correlations are performed by using digitized images on a computer.

Tomographic methods using Radon transform (Radon, 1986) offers a better alternative since they are computationally efficient. We have developed a tomographic technique which reduces the memory and processing requirements in bispectrum technique. The tomographic technique transforms the images in to a set of projections and applies bispectrum based reconstruction on these one dimensional projections. By transforming two dimensional speckle images in to its one dimensional speckle projections, huge savings in memory and processing time have been achieved. The developed algorithm combines two powerful mathematical techniques, Triple Correlation and Radon Transformation. The results obtained from the developed code

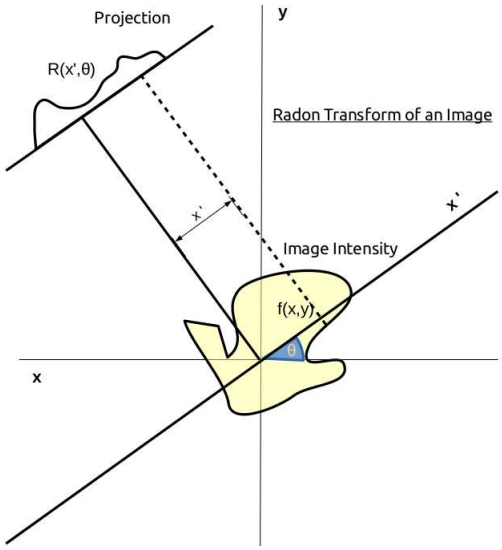

Figure 4.1: An image function and the projection at an angle. $f(x, y)$ is two dimensional image in the $x - y$ plane. $R(x', \theta)$ is one of the projections in the Radon transform at angle θ.

with numerical simulations, laboratory simulations and real speckle images of binary stars are presented in this chapter.

4.2 Radon Transform

A basic problem encountered in Tomography is given a set of one dimensional projections and the angles at which these projections were taken, how to reconstruct the two dimensional image from this given data. Lets define $R(x', \theta)$ as a 1-D projection at an angle θ. $R(x', \theta)$ is the line integral of image intensity, $f(x, y)$, along the line l that is x' distance away from the origin at an angle θ of the x-axis.

$$R(x', \theta) = \int_l f(x, y) dl \tag{4.1}$$

This collection of $R(x', \theta)$ at all θ is called the Radon transform of image $f(x, y)$. We can also define Radon Transformation as a method by which a one dimensional image is transformed in to a set of projections. This transformation essentially allows us with the capability of dealing with a set of one dimensional signals for a two dimensional signal. Radon transform for

function $f(x, y)$ is described mathematically as,

$$R(x', \theta) = \int_{-\infty}^{+\infty} f(x'cos\theta - y'sin\theta + x'sin\theta - y'cos\theta)dy', \tag{4.2}$$

where,

$$\begin{bmatrix} x' \\ y' \end{bmatrix} = \begin{bmatrix} \cos\theta & \sin\theta \\ -\sin\theta & \cos\theta \end{bmatrix} \begin{bmatrix} x \\ y \end{bmatrix} \tag{4.3}$$

Figure 4.1 shows a sample projection of a two dimensional image.

4.2.1 Properties of Radon Transform

Symmetry

The parameter set of $x' \in [0, \infty]$ and $\theta \in [0, 2\pi]$ describes every element of Radon Transform since

$$R(x', \theta) = R(-x', \theta + \pi) \tag{4.4}$$

Linearity

For α_i constants and f_i functions

$$R(\alpha_i.f_i) = \sum_i \alpha_i.R(f_i) \tag{4.5}$$

Fourier Slice Theorem

The Fourier Slice theorem states that the 1-dimensional Fourier transform of the projection function $R(x', \theta)$ is equal to the 2-dimensional Fourier transform of the image evaluated on the line the projection was taken.

4.2.2 Inverse Radon Transform

Just like Radon transform converts a two dimensional signal into a set of projections taken at different angles, inverse Radon transform aims at constructing the two dimensional signal from this set of projections. There are several algorithms that perfoms an inverse Radon transform. But the most commonly used algorithm is filtered back projection.

4.2.2.1 Filtered Back Projection

By Fourier slice theorem discussed earlier, if we know the projections functions at several angles of the image, we can get a sample of lines in the Fourier transform of the image. In filtered back projection we sum all the Fourier slices obtained this way creating a sampled Fourier map of the object. This Fourier map can be inverse Fourier transformed to obtain the object image. This is called back projection. The simple back projected image is blurry since the lower frequencies would be added multiple times, since they are sampled by each Fourier slice. To counter act this blur effect, we multiply each Fourier slice with a ramp function. This technique is called filtered back projection. Thus the image is obtained as follows,

$$f(x,y) = \frac{1}{4\pi^2} \iint \widehat{R}(u,\phi) e^{iu(xsin\phi - ycos\phi)} |u| du d\phi, \tag{4.6}$$

where, $\widehat{R}(u,\phi)$ is the Fourier transform of projection function $R(x',\theta)$. Note that the Fourier slices are multiplied by $|u|$ in the Fourier domain. An example of Radon transformation of an image and its inverse transformation using filtered back projections is shown in Figure 4.2.

4.3 Tomographic Speckle Masking Algorithm

In radon transform based triple correlation method, we will perform radon transformation on each two dimensional speckle frame, to produce set of projections $I_1, I_2, ..I_n$. Then we compute the averaged triple correlation for each projection over all frames

$$\langle I^{(3)}(x_1,x_2)\rangle = \langle \int_{-\infty}^{+\infty} I(x)\cdot I(x+x_1)\cdot I(x+x_2)dx\rangle \tag{4.7}$$

or compute the averaged bispectrum

$$\langle \hat{I}^{(3)}(u_1,u_2)\rangle = \langle \hat{I}(u_1)\cdot \hat{I}(u_2)\cdot \hat{I}^{\star}(u_1+u_2)\rangle \tag{4.8}$$

From this averaged bispectrum the real projections are reconstructed and they are inverse radon transformed to recover the original signal. Radon transform

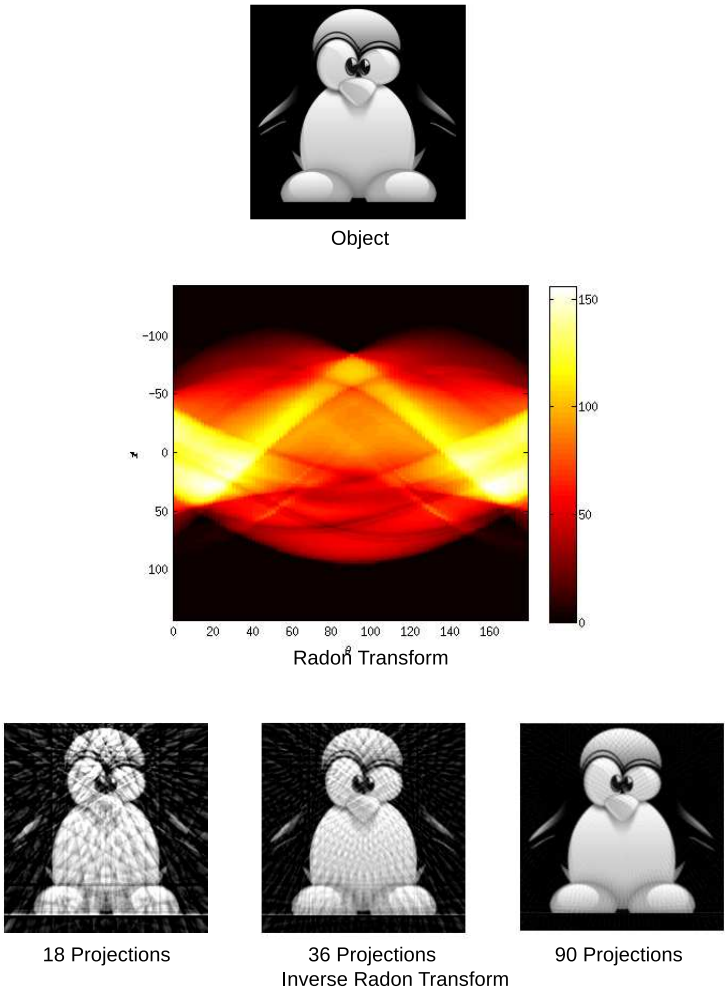

Figure 4.2: Process of Radon transform and inverse Radon transform of a 2 dimensional image. (Bottom) The inverse Radon transformed images from different number of projections [18, 36, 90].

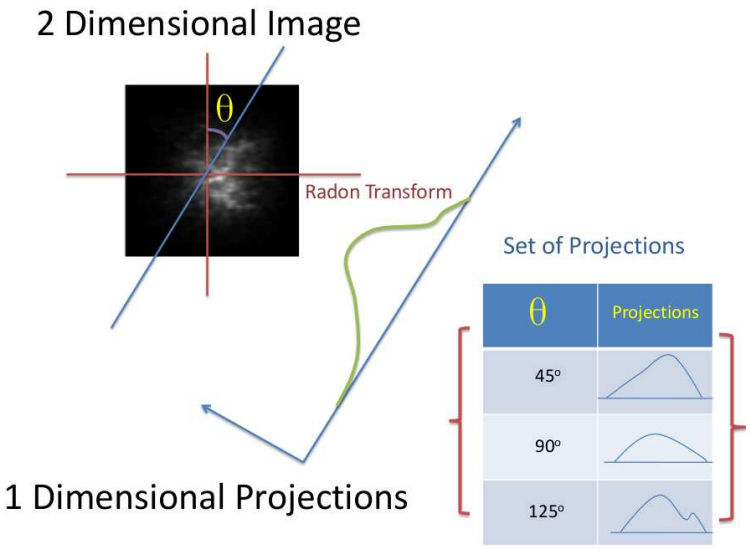

Figure 4.3: A two dimensionsl speckle image and its sample one dimensional projections obtained at different angles using Radon Transform.

based image retrieval takes less computational time and also requires less memory at the expense of reconstruction quality. In the TSM algorithm we combine Triple correlation and Radon transform techniques to develop a robust and fast algorithm to retrieve images. The steps in the developed algorithm is as follows

1. Radon Transform each 2 dimensional speckle frame in to set of projections $I_1, I_2, I_3..etc$ as shown in Figure 4.3

2. Find the averaged bispectrum $\langle \hat{I}^{(3)}(u_1, u_2)\rangle$for each projection over all frames.

3. Retrieve the Fourier phase $\phi(u)$ of the object projection from the averaged bispectrum using recursion formula used in equation 3.30.

4. Retrieve the Fourier amplitude of the object projection from the averaged power spectrum $\langle \hat{I}^{(2)}(u_1, u_2)\rangle$.

5. Combine the Fourier phase and amplitude to recreate the true object projections.

6. Inverse Radon transform the retrieved projections to obtain the object image.

4.4 Numerical Simulations

We have carried out extensive numerical simulations of tomographic speckle imaging reconstruction of aperture masking images. The basic parameters of the simulations are same as used in the earlier example with Direct Bispectrum Algorithm discussed in Section 3.5.2. The parameters and aperture used are shown respectively in Table 3.1 and Figure 3.6. The results with TSM algorithm are shown in Figure 4.4 and Figure 4.5. Figure 4.4 shows the results with a binary star and Figure 4.5 shows the reconstruction results with an extended object.

We have quantified the reconstruction quality using 2-dimensional correlation coefficient c which measures the correlation between the reconstructed image and the cophased image in the absence of atmospheric turbulence. The correlation coefficient, c is computed according to the following equation

$$c = \frac{\sum_m \sum_n (A_{mn} - \bar{A})(B_{mn} - \bar{B})}{\sqrt{(\sum_m \sum_n (A_{mn} - \bar{A})^2)(\sum_m \sum_n (B_{mn} - \bar{B})^2)}} \tag{4.9}$$

where A and B are the cophased and reconstructed images respectively with size $m \times n$. The corrosponding correlation coefficients of the reconstructions are given in Table 4.1.

As it is visible from the reconstructed images, the tomographic speckle imaging algorithm has been found to obtain good reconstructions of the object configurations. But since the reconstructions rely on one dimensional projections from the image and the reconstructed projections are used to retrieve the object image, the resulting images have artifacts due to the projection operations which results in a lower c value. But when we increase the number of projections used in radon transformation of image, the quality of reconstruction increases and there are visibly less projection artifacts in recovered image which results in a better c value. The reconstruction quality

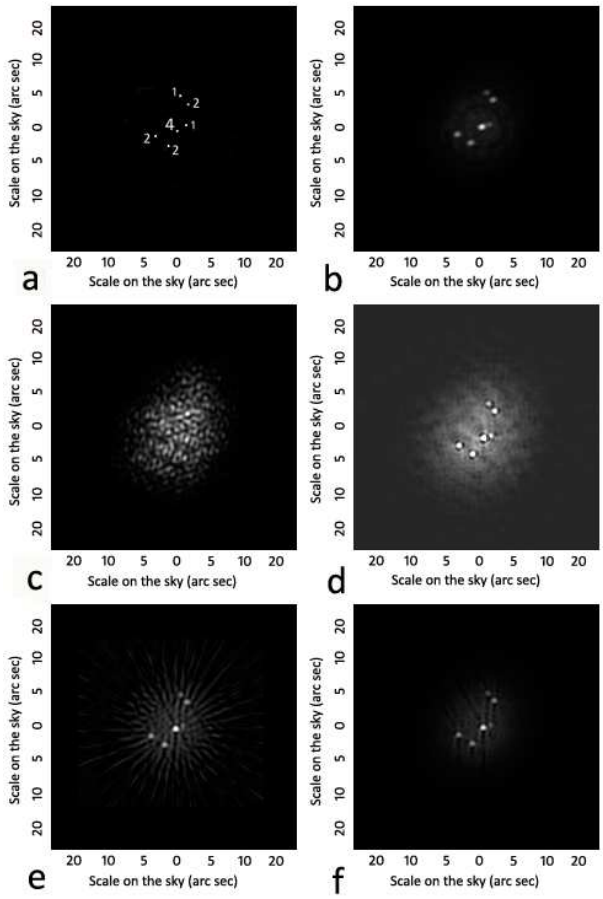

Figure 4.4: The image recovery results from the tomographic speckle imaging algorithm of a 6 star group using a 17 hole aperture mask: The aperture consists of randomly arranged 10 cm holes inside 1 m radius disk, a) the 6 star object distribution used in the simulation with the corresponding brightness ratio, b) The cophased image from the aperture masked mirror, c) The simulated speckle image of the object by imaging through turbulence, d) The recovered image using Direct Bispectrum with 100 frames, e) The recovered image using tomographic speckle masking from 18 projections with 100 frame and f) the recovered image using tomographic speckle masking from 180 projections with 100 frames.

is still not comparable to the direct bispectrum algorithm as seen from the results and the c values given in the Table 4.1. But tomographic speckle imaging offers a very high computational advantage over direct bispectrum imaging. With lesser number of projections the computational time and memory requirements reduces very significantly. Thus it required to find a trade

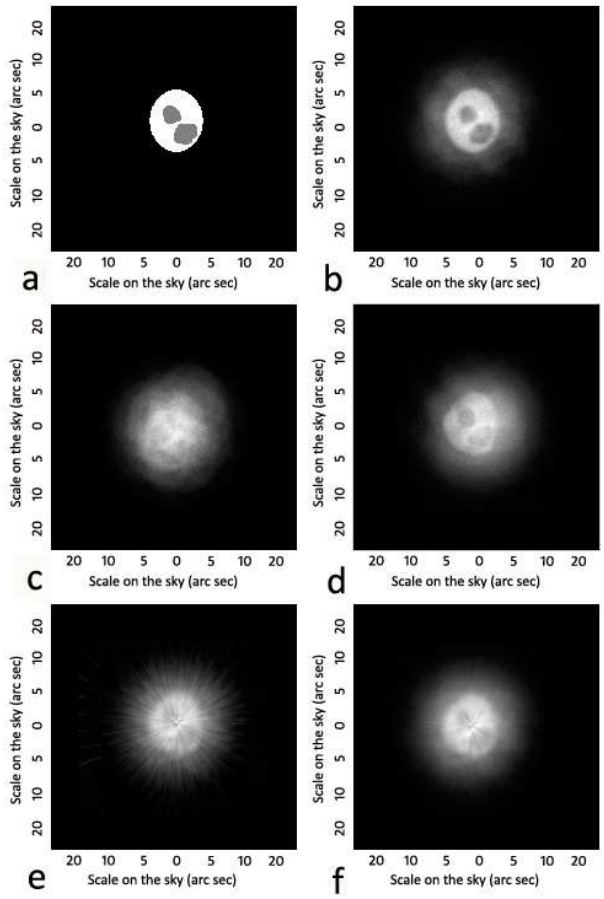

Figure 4.5: The image recovery results from the tomographic speckle imaging algorithm of an extended planet object group using a 17 hole aperture mask: The aperture consists of randomly arranged 10 cm holes inside 1 m radius disk, a) the 6 star object distribution used in the simulation with the corresponding brightness ratio, b) The cophased image from the aperture masked mirror, c) The simulated speckle image of the object by imaging through turbulence, d) The recovered image using Direct Bispectrum with 100 frames, e) The recovered image using tomographic speckle masking from 18 projections with 100 frames and f) the recovered image using tomographic speckle masking from 180 projections with 100 frames.

off between computational time and recovery requirements for larger sized images and more number of frames.

	Direct Bispectrum	Tomographic Code 180 Projections	Tomographic Code 18 Projections
Computational Time	1 hr 21 mins	15 mins	2 mins
Size Limit for Frames	200 x 200 pixels	10^4 x 10^4 pixels	10^4 x 10^4 pixels
c for 6-star Group	0.94	0.83	.94
c for Extended Object	0.96	0.92	.95

Table 4.1: Comparison of computational requirements and reconstruction quality parameter, c of direct bispectrum and tomographic algorithms. The values are calculated based on MATLAB 32-bit used in a 32-bit Windows system with 4 GB of RAM.

4.5 Laboratory Simulations

The experimental setup for the simulation of aperture masking is shown in Figure 4.6. A binary star was simulated using two laser sources. The setup consisted of two 5mw laser sources which were collimated using a lens, phase screen, aperture mask and an imaging lens which focuses on the detector. The laser sources used are 5mW red lasers at 633 nm. The lasers were arranged such that they subtend an angle of 20 arc second in the detector plane. The phase screen is made from spraying glycerin over a glass surface. Several phase screens with different atmospheric coherence lengths were prepared as part of the experiment. The results of the reconstructions using TSM algorithm on the speckle frames of the artificial binary star are shown in Figure 4.7. The speckle images obtained from the experiment had an average of 1000 counts/frame and 100 such frames were processed by the Tomographic Speckle Masking Code to obtain the reconstructed image. One of the speckle image is shown in Figure 4.7.b. The results of the reconstructions using TSM algorithm on the speckle frames of the artificial binary star are shown in Figure 4.7.c. The reconstruction resolved the binary stars with the correct separation. This laboratory experiment clearly demonstrates the performance of tomographic algorithm with aperture masking.

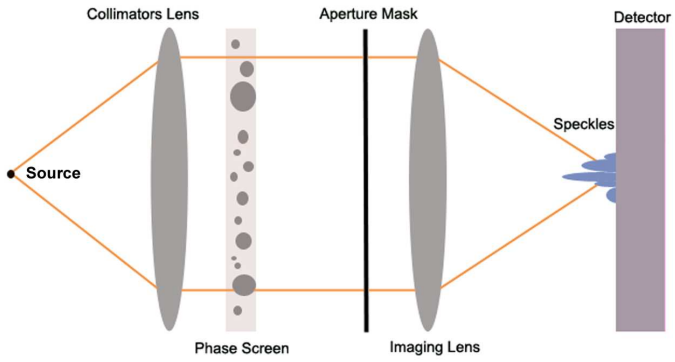

Figure 4.6: Laboratory setup for simulation of aperture masking in presence of atmospheric turbulence. Laser source is collimated using a lens, and the collimated beam passes through the phase screen and aperture mask of 20 random holes. The beam then passes through an imaging lens to form a speckle image in the detector.

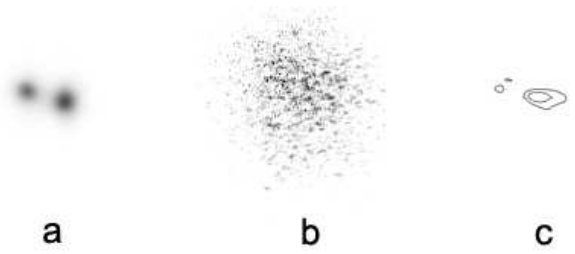

Figure 4.7: Reconstruction from laboratory simulations of speckle imaging: a) image of the artificial binary star from the experiment with out using turbulence phase screen, b) speckle image of binary star imaged with a Kolmogrov phase screen in laboratory and c) reconstructed image from tomographic speckle masking from 100 speckle frames.

4.6 Results with Real Speckle Images

The developed algorithm was applied on images of β Coronae Borealis (HR5747) taken on 16 and 17 March 1990 from the 2.34 meter Vainu Bappu Telescope (VBT) in Kavalur using a speckle camera system developed by Saha *et al.* (1997), the description of which was given in earlier Section 3.5.1. The results are shown in Figure 4.8. The binary star was earlier resolved using Blind Iterative Deconvolution (BID) (Saha & Venkatakrishnan, 1997 Saha and Venkatakrishnan (1997)) and the separation was found to be 0.20 arc-

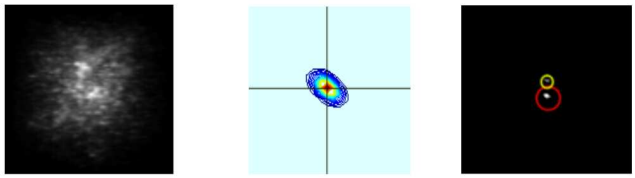

Figure 4.8: Tomographic image reconstruction of speckle images of β Coronae Borealis (HR5747): a) one of the speckle images of HR5747, b) the bispectrum of a one dimensional projection of the speckle image and c) the reconstructed image using TSM Algorithm.

second and magnitude difference of 1.65. The results of tomographic speckle masking on the same speckle images gave results show a separation of 0.21 arc seconds in figure. The difference of separation values with BID and TSM may be attributed to the fact that tomographic speckle masking utilized 8 frames of the binary star as compared to a single frame used in blind iterative deconvolution technique.

4.7 Conclusions

We have successfully developed two algorithms based on triple correlation technique to process atmospherically degraded astronomical images. One uses the direct bispectrum technique and the other is the tomographic speckle masking algorithm, that uses radon transformation. In this chapter we discussed about the tomographic algorithm. The developed tomographic speckle masking algorithm has been found to obtain good reconstructions with smaller evaluation time and memory requirements, compared to the direct bispectrum technique. Since the number of projections used for the radon transform can be varied, it is possible to obtain smaller evaluation times at the cost of reconstruction quality. The developed algorithm can be used with short exposure speckle frames to obtain astronomical images of high resolution. Bayesian and regularization techniques could be used to improve the reconstructions from the algorithm, and also enable it to be used with long baseline interferometric

data. Tomographic speckle imaging offers a unique way to implement very fast reconstruction algorithms based on triple correlation. It has been shown with the help of simulations and laboratory experiments that tomographic speckle masking code can be used with aperture masking interferometry to obtain very good reconstructions of stellar objects.

Chapter 5

Speckle Imaging with Hypertelescopes

5.1 Introduction

In high-resolution optical astronomy with interferometric arrays, producing better images will require more apertures for a denser sampling of the optical wave. As few as three apertures can suffice in principle to reconstruct images through "optical aperture synthesis" (Baldwin *et al.*, 1986), using earth rotation or baseline changes to sample the needed Fourier components of the object. But a better sensitivity can be reached with systems using more apertures simultaneously, even if these are smaller for a conserved collecting area. The gain arises from the coherent combination of light vibrations achievable with many apertures working simultaneously, as opposed to the "optical aperture synthesis" approach where interference fringes are recorded with fewer apertures, repeatedly with different baseline settings, and then combined in the computer, i.e. incoherently. N number of phased beams combined coherently with a simple Fizeau arrangement indeed produces a highly constructive interference, in the form of a peak which is N times more intense than the average side-lobes. Instead, successive exposures with subsets of the sub-apertures, even if they are enlarged to conserve the photon flux and moved

to improve the spatial frequency coverage, reduce the peak intensity and thus the dynamic range in the convolved image of a complex source (Labeyrie, 2007). Fizeau combination however becomes inefficient with highly diluted apertures, since the narrow interference peak appearing in the image of a point source, at the center of the much broader envelope diffracted by the subapertures, contains a small proportion of the energy. A way of retrieving most energy in the peak, for efficiently observing faint sources with many-aperture interferometers capable of rich direct imaging, has appeared in the form of the hypertelescope or "densified aperture "scheme (Labeyrie, 1996; Lardière *et al.*, 2007). Practical designs for large hypertelescopes, with a spherical geometry inspired from the Arecibo radio telescope (Altschuler, 2002), are under testing for terrestrial versions (Le Coroller *et al.*, 2004, 2012b; Enmark *et al.*, 2011; Labeyrie *et al.*, 2012b) and also studied for space versions (Labeyrie *et al.*, 2009, 2010). These future large direct imaging interferometers using many apertures will greatly benefit from adaptive optics systems for ultimate performance on faint sources, providing usable imaging with large exposure time. But even in the absence of adaptive phasing, high resolution imaging can be done in speckle mode. Speckle mode techniques like speckle interferometry (Labeyrie, 1970) and speckle masking (Weigelt, 1977; Lohmann *et al.*, 1983), heretofore successfully used with large monolithic telescopes, can also produce useful results with such interferometers.

We describe the numerical simulations done to understand the scope and explore the performance of speckle imaging techniques with this type of diluted aperture interferometers. We have built a numerical simulation code in MATLAB that simulates cophased and speckle mode imaging with diluted apertures in different configurations. The imaging performance of interferometers is much affected by their beam combination scheme, as analyzed in detail by Lardière *et al.* (2007). In our simulation we have adopted the pupil densification scheme (Labeyrie, 1996), also adopted for the Ubaye Hypertelescope Project currently undergoing preliminary testing in the Southern Alps (Labeyrie *et al.*, 2012b). Pupil densification concentrates the diffracted

energy in the central part of the PSF without degrading the resolution. A detailed analysis of the PSF and imaging properties of these diluted aperture interferometers has been done by Patru *et al.* (2009) and Lardière *et al.* (2007). In this Chapter, our simulations extend these results to the case of randomly phased apertures exploited with speckle imaging, and also in the use of aperture rotation which enhances the quality of reconstructed images. We have also tried to find out the limiting magnitude for such a technique by comparing Signal to Noise Ratio (SNR) of reconstructions at different photon levels.

5.2 Numerical Simulations

According to the usual definition of hypertelescope imaging we consider a multi-aperture Fizeau interferometer equipped with a non-distorting pupil densifier i.e., one which does not distort the pattern of sub-aperture centers. This makes the interference function field-invariant, while the spread function depends on the star's position, through its diffraction factor. This variable spread function, hereafter called "pseudo spread function ", results in a pseudo-convolution process which describes the image formation on extended sources. For n_T identical sub-apertures with position vectors (u_k, v_k), the cophased Pseudo Spread Function Labeyrie (1996) is expressed as

$$I_{PSF}(x, y) = A(x, y) \times I_0(x, y), \tag{5.1}$$

where $A(x, y)$ is the diffraction function and the term on the right side, $I_0(x, y)$ is the Interference function given by,

$$I_0(x, y) = \left| \sum_{k=1}^{n_T} e^{-\frac{2\pi i}{\lambda}(xu_k + yv_k)} \right|^2 . \tag{5.2}$$

The interference function depends only on the array configuration while the diffraction function $A(x, y)$ depends on the beam combination scheme used Lardière *et al.* (2007). For our analysis we have considered $A(x, y)$ to be an Airy function corresponding to the densified subaperture diameter d_0. In

our simulation we are considering highly diluted arrays, approximated to array of δ-functions, in which pupil densification is so strong that the shift of the Airy envelope is negligible. In such a case the image formation of the hypertelescope can be defined by a Pseudo Convolution Equation

$$I(x, y) = A(x, y) \times (I_0(x, y) * O(x, y)) \,, \tag{5.3}$$

where $O(x, y)$ is the object intensity distribution. The pseudo convolution creates the Direct Imaging Field of the interferometer which is the diffraction function envelope corresponding to the densified subaperture. This modeling of hypertelescope imaging is similar to the study by Aime (2008). In order to

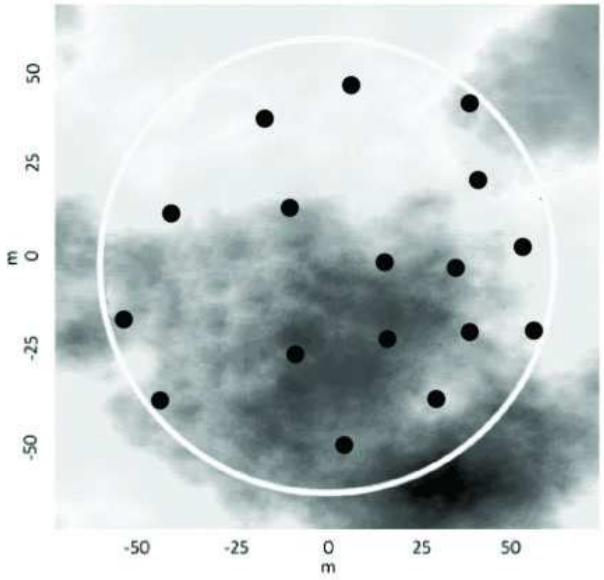

Figure 5.1: Random phase screen across the 17 mirror aperture used for the simulations, following a Kolmogorov distribution. The dots indicate positions of the subapertures in the fully diluted array.

simulate the seeing conditions we have generated Kolmogorov phase screens (see Figure 5.1) with different values of Fried's parameter. These screens move with different wind velocities which simulate seeing changes. In this we assume that the wavefront is coherent across an individual subaperture. This will be the case if one uses small mirrors ($< 10\ cm$) in a site with good seeing conditions, and hence only piston errors associated with each subaperture

was considered. The random atmospheric piston error $e^{i\phi_k}$ from the corresponding position of the sub-aperture in the phase screen is introduced into the interference function.

$$I_0(x,y) = \left| \sum_{k=1}^{n_T} e^{-\frac{2\pi i}{\lambda}(xu_k + yv_k)} . e^{i\phi_k} \right|^2 \tag{5.4}$$

This new speckle interference function is used in the pseudo-convolution equation (5.3) to simulate speckle observations. Some of the speckle images corresponding to sample objects used in the study are shown in Figure 5.2.

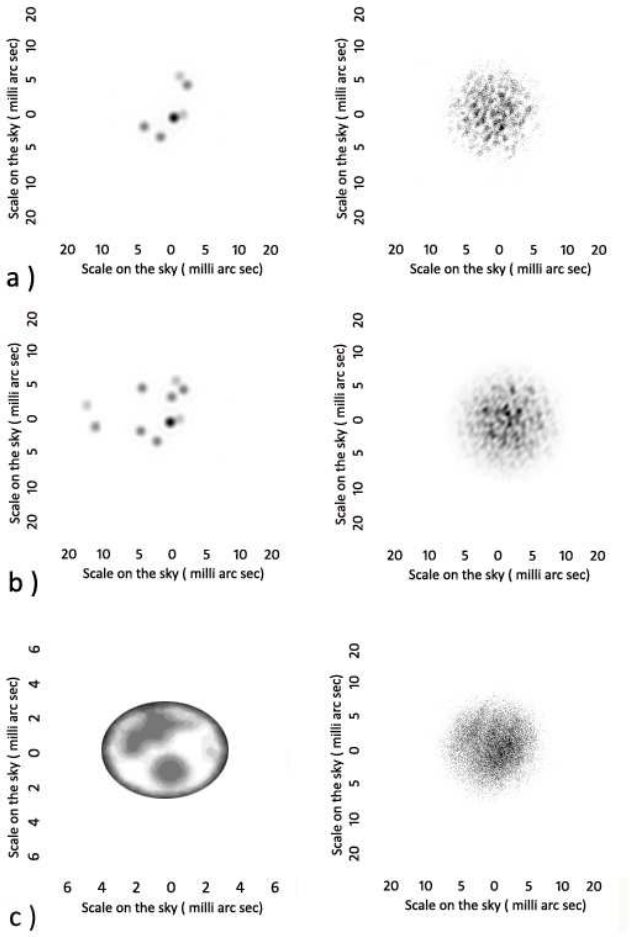

Figure 5.2: The object distributions used in the simulations (first column) along with their corresponding speckle frames (second column) as imaged by the 17 mirror array: a) six star group b) ten star group c) extended object. Speckle frames in average have 10000 photon events per each exposure.

5.2.1 Aperture Configuration

Though there are several aperture configurations under consideration for the big imaging interferometers, the one we studied was of randomly distributed mirrors with non-redundant baselines. The number of diluted apertures, n_T of 17 (Figure 5.1) and 50 were considered for this study. The details of aperture configuration used in the simulations are in Table 5.1. Details of the pupil

	17 mirror	50 mirror
Maximum Baseline	100 m	100 m
Minimum Baseline	21 m	12 m
Output Pupil Filling rate τ_o	0.2	0.5
Sub-aperture diameter	10 cm	10 cm

Table 5.1: Parameters associated with aperture configuration.

densification beam combination scheme used in the simulations are discussed in depth by Lardière *et al.* (2007) and Labeyrie (1996). The pupil densification of 17 mirror aperture is shown in Figure 5.3. Densification is constrained by the smallest baseline $S^{'}_{min}$ in the output pupil, since any further densification will cause subapertures to overlap. Thus in maximum densification, length of the smallest baseline in output pupil will be equal to the densified subaperture diameter, i.e. $S^{'}_{min} = d_o$. In our simulation for all the array configurations we have taken densified diameter of each diluted subaperture d_o to be 1/10 of the largest baseline in the output pupil. Output pupil which is partially filled creates a speckle halo surrounding the central peak in cophased case. The dominance of this halo is dependent on the output pupil filling rate (τ_o). The parameters associated with numerical simulation are shown in Table 5.2.

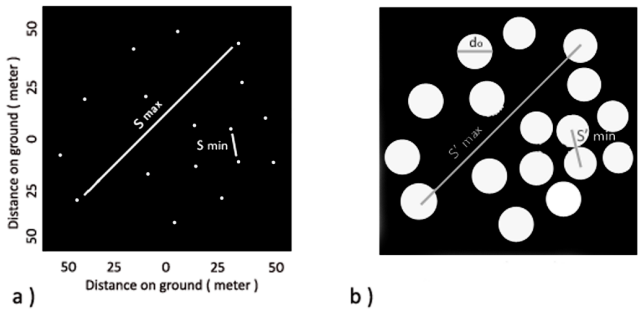

Figure 5.3: Pupil densification of the aperture configuration used in the simulations. a) The input pupil of a diluted random 17 mirror array. b) The exit pupil after densification

Frames used in speckle masking	500
Earth Rotation time simulated	8 h
Plate scale for each frame	0.2 milli arc sec /pixel
Wavelength	550 nm
Bandwidth	88 Å
Fried Parameter	0.1 m
Wind Velocity	10 m/s
Latitude of the place	$+60^0$
Declination of the source	$+90^0$

Table 5.2: Parameters used in the simulation of hypertelescope imaging in the presence of atmospheric turbulence

5.2.2 Speckle Imaging Algorithms

For the speckle images generated from numerical simulation of hypertelescopes, techniques like speckle interferometry and bispectrum technique were applied to reconstruct the object distribution. The speckle interferometry code was written in MATLAB and produces the Fourier amplitude information and autocorrelation of the object distribution. In speckle interferometry, the average power spectrum $\sum|I(u,v)|^2$ is found out from the speckle frames

and object Fourier amplitude information is extracted from it. The computed Fourier amplitude information is used in speckle masking. Though a computationally efficient tomographic speckle masking (TSM) code Surya and Saha (2014), has also been developed, we have for the current study used the direct bispectrum code which gives a better quality of reconstruction because it uses the four dimensional bispectrum. The direct bispectrum code can process 200 x 200 pixels images of 300 frames in 15 minutes in a i7 Intel computer with 8 GB of RAM. The unit amplitude phasor method, used in algorithms by Sridharan (2000) Sridharan (2000), is used in the code for phase reconstruction. The details of the reconstruction code is explained in Chapter 3. The code uses direct computation of the 4-dimensional bispectrum $I^{(3)}(u, v, u^{'}, v^{'})$ which poses severe constraints on the computer memory. The 4-D bispectrum is computed and averaged out for all the speckle frames. The Fourier phase is retrieved from the bispectrum using the techniques explained in Section 2.2, and is combined with Fourier amplitude from speckle interferometry to reconstruct the object.

5.2.3 Earth Rotation Aperture Synthesis

The sparse filling of the entrance aperture, although enhanced in the densified exit pupil, affects the performance of the speckle imaging reconstruction. But part of it is retrieved if the entrance aperture, as seen from the observed star, can be modified or rotated during an observation. This happens naturally for interferometers of fixed ground elements due to earth's rotation. Earth Rotation Aperture Synthesis is a common technique frequently exploited in radio interferometry to increase the coverage of the frequency plane by an interferometric array. With the help of simulations, we have tried to study the possible techniques of using aperture rotation through night with diluted aperture hypertelescope systems. Reinheimer *et al.* (1993, 1997) had earlier studied the use of aperture rotation with speckle masking for studies of LBT and VLTI interferometers in multi speckle mode. We have detailed our own

multi-speckle simulations in Chapter 2 and Chapter 3. In this Chapter we will study the use of such techniques with long baseline hypertelescope arrays.

Using speckle frames from different time of the night averaged power spectrum, $\sum_i |I(u,v,t_i)|^2$, provides a better u-v coverage and thus a better estimate of the Fourier modulus to be used in reconstruction. When speckle frames from different time of the night were used, the time dependent bispectrum, $I^{(3)}(u,v,u^{'},v^{'},t_i)$, of each frame was computed and averaged. From the averaged bispectrum, $\sum_i I^{(3)}(u,v,u^{'},v^{'},t_i)$, the image of the object was reconstructed. The averaged bispectrum contains the u-v coverage as sampled through the night by earth rotation and hence provides a better reconstruction of object phase.

5.3 Results

The numerical simulations provide a clear picture of how speckle masking can be used together with hypertelescope imaging utilizing aperture rotation to yield high resolution images of stellar objects. The bispectrum code was utilised to reconstruct images from the speckle images simulated from the diluted hypertelescope. We have quantified the reconstruction quality using correlation coefficient c which measures the correlation between the reconstructed image and the cophased image in the absence of atmospheric turbulence. The correlation coefficient, c is computed according to the equation 4.9 discussed in Chapter 4. Such quantification of reconstruction gives us the ability to compare the reconstructions with different parameters.

5.3.1 Reconstruction results with sextuple star and extended objects

We have simulated sequences of short exposures, shorter than the lifetime of "seeing", and each exploiting the full set of sub-apertures. The parameters associated with this simulation are shown in Table 5.1 and Table 5.2. Two

	Aperture Rotation	17 mirror	50 mirror
Sextuple Star	No	.60	.71
	Yes	.77	.78
Extended Object	No	0.5	0.90
	Yes	0.88	0.92

Table 5.3: The values of correlation coefficient c corresponding to the reconstruction of sextuple star and extended object from the speckle images with 17 mirror and 50 mirror array.

different sequencing regimes were simulated,

- a) Dense sequences, with 1000 short exposures made in a matter of minutes while the slow Earth rotation causes a negligible rotation of the meta-aperture with respect to celestial North;
- b) Night-long sequences, where Earth rotation becomes significant and exploitable for aperture-synthesis.

The speckle images from the simulations were processed by the bispectrum technique to obtain reconstructions. The results of these simulations are shown in Figure 5.4 and 5.5. When available, long sequences thus exploited improve the result quality, especially if there are a small number of sub-apertures. The correlation coefficient c between reconstructed image and the corrosponding cophased image for both the objects with different arrays are shown in Table 5.3.

5.3.2 Improvement of Reconstruction with Aperture Rotation

The improvement of signal reconstruction in speckle masking using aperture rotation is clearly demonstrated in Figure 5.6. The object used is a star cluster

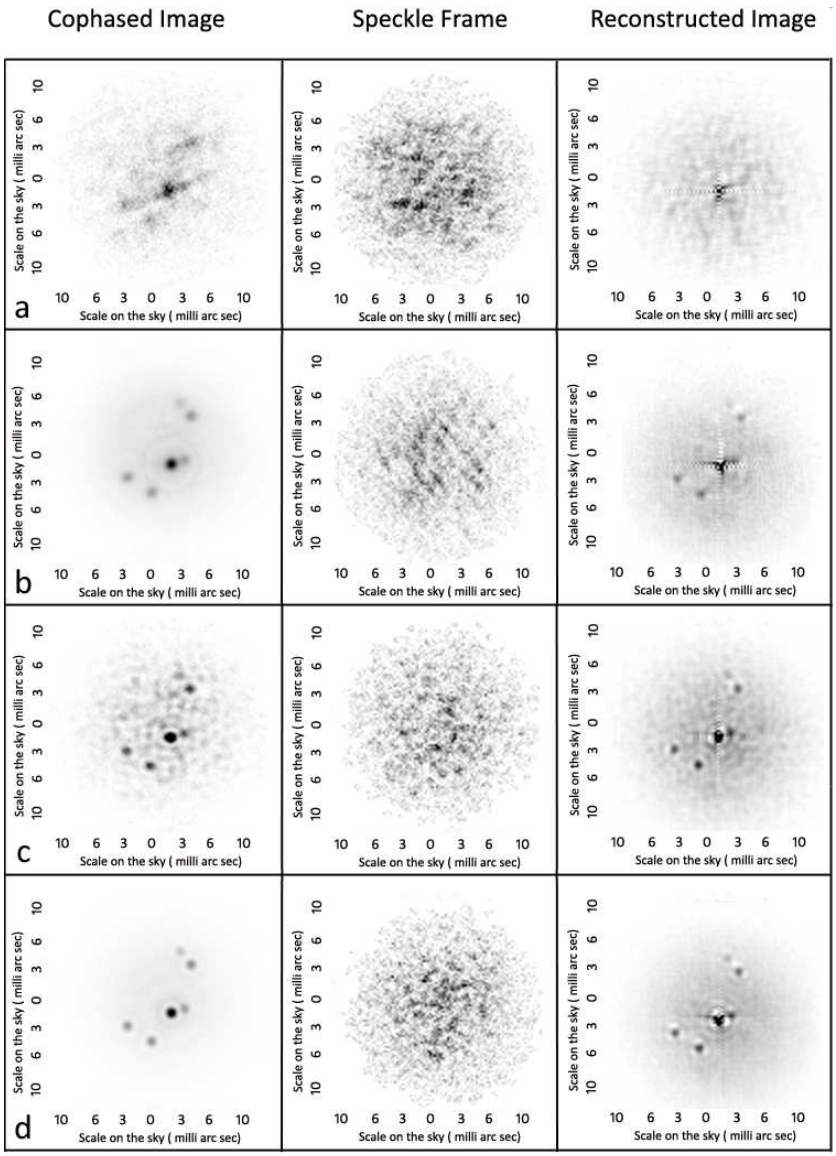

Figure 5.4: Speckle imaging results for a six star cluster from turbulence degraded interferograms from a) 17 mirror aperture without aperture rotation, b) 17 mirror aperture with rotation through the night for 8 hrs, c) 50 mirror aperture without rotation and d) 50 mirror aperture with aperture rotation through night for 8 hrs. Each simulated exposure on average had 10,000 photon events.

with 10 stars (Figure 5.2.b). The aperture used is a 17 mirror array with rotation synthesis corrsponding to 1 hour, 3 hour and 8 hour. The respective correlation coefficient for each of the reconstructions is shown in Table 5.4. We have correlated the reconstructed image here with the true object image. The improvement in c shows the improvement of the reconstruction with

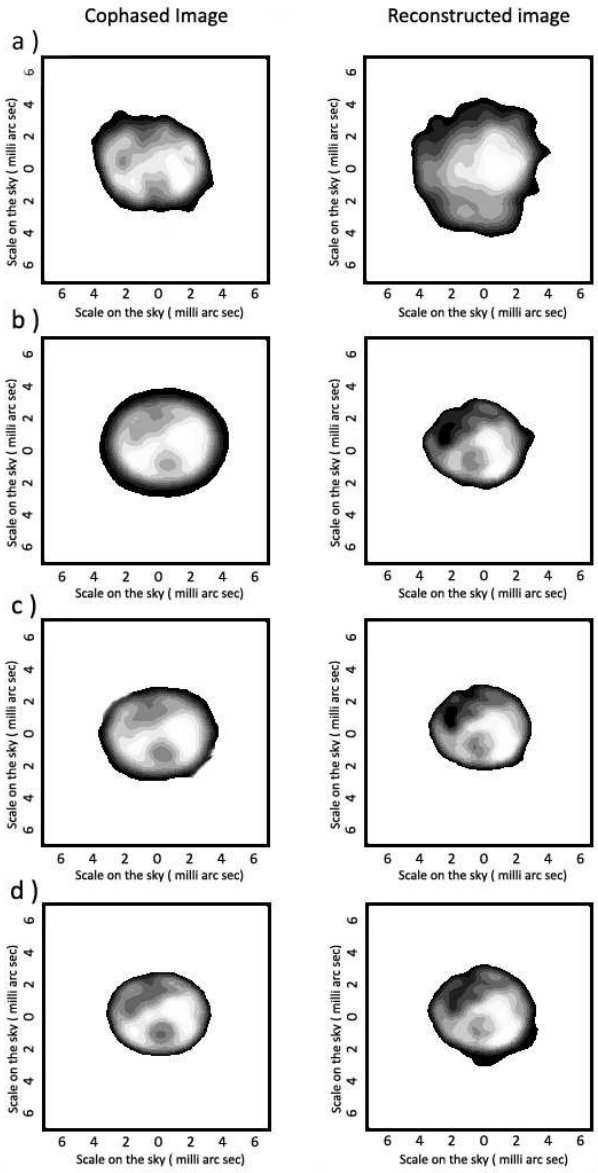

Figure 5.5: Speckle imaging results for an extended object from turbulence degraded interferograms from a) 17 mirror aperture without aperture rotation, b) 17 mirror aperture with rotation through the night for 8 hrs, c) 50 mirror aperture without rotation and d) 50 mirror aperture with aperture rotation through night for 8 hrs. Each simulated exposure on average had 10,000 photon events.

better spatial frequency coverage. It is also curious to note the field of view limitation due to pupil densification as also seen from the Figure 5.6. Only 8 stars out of the 10, which are inside the Direct Imaging Field are seen from the reconstructed image.

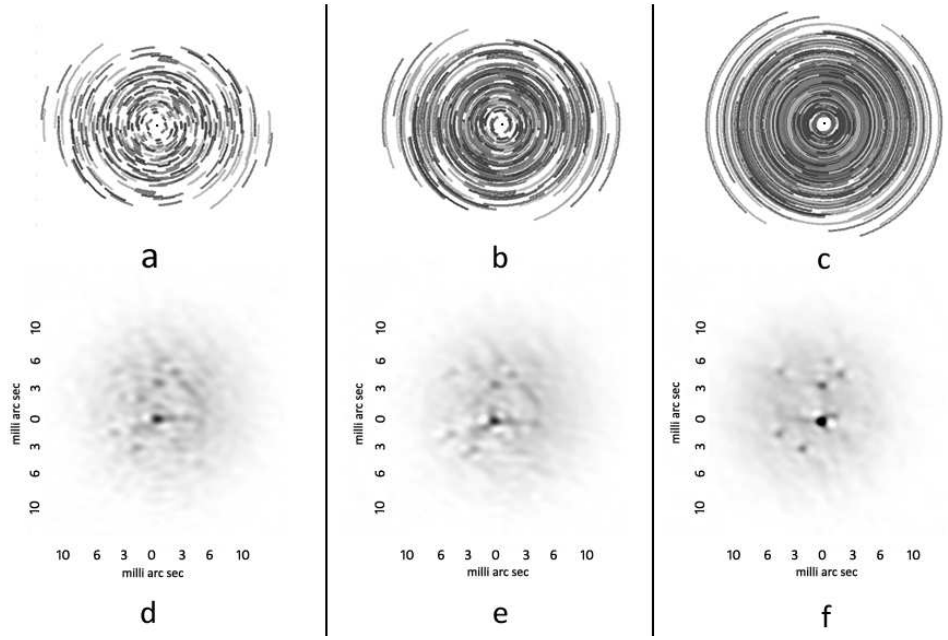

Figure 5.6: Improvement of reconstructed image of star cluster with ten stars (Figure 5.2.b), utilizing aperture rotation through night. a) u-v coverage of 17 mirror array over 1 hr of observation b) u-v coverage of 17 mirror array over 3 hr of observation c) u-v coverage of 17 mirror array over 8 hr of observation. d,e and f are the corresponding reconstructed images obtained by speckle imaging in each case. The latitude of the site was taken as 60^0 North and the declination of the star cluster is considered to be 90^0. The images where reconstructed from 500 speckle frames each with an average of 10,000 photon counts.

	3 hour	6 hour	8 hour
Correlation coefficient c	0.49	0.52	0.62

Table 5.4: The correlation coefficient values corresponding to the reconstruction of the star cluster with increasing hours of observation to utilize aperture rotation. The array used is of 17 sub-apertures.

5.3.3 Limiting Magnitude

We wanted to compute the limiting magnitude of objects retrievable through such a technique. For this we have simulated imaging of two objects, a binary star and a resolved star with spots. Both the objects were imaged assuming

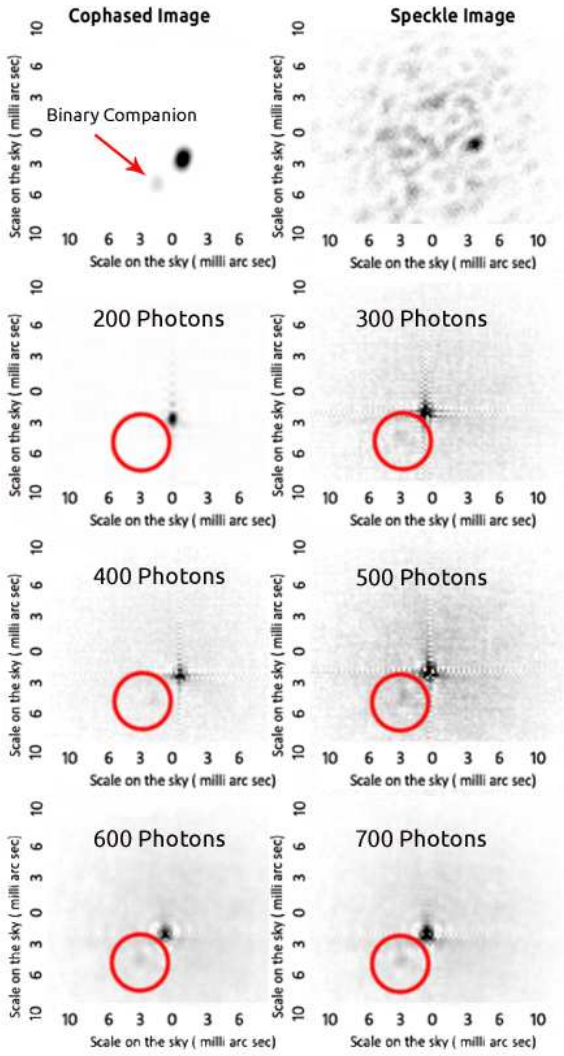

Figure 5.7: Reconstruction of a Binary Star with Brightness ratio 1000:1 at different magnitudes. The aperture used is an array of 50 mirrors with 7 hours of earth roatation aperture synthesis, which increases the spatial frequency coverage. (Top row) The ideal cophased image and speckle image of the binary star. (Bottom three rows) The reconstructed images using the bispectrum technique with the corrosponding photon counts. The region inside the red circle is used to compute the SNR.

different magnitudes progressively and the Signal to Noise Ratio was computed for each recontruction. Since the photon levels of speckle images used for reconstructions to compute limiting magnitude were very low, we have used another measure to compute the Signal to Noise Ratio instead of the

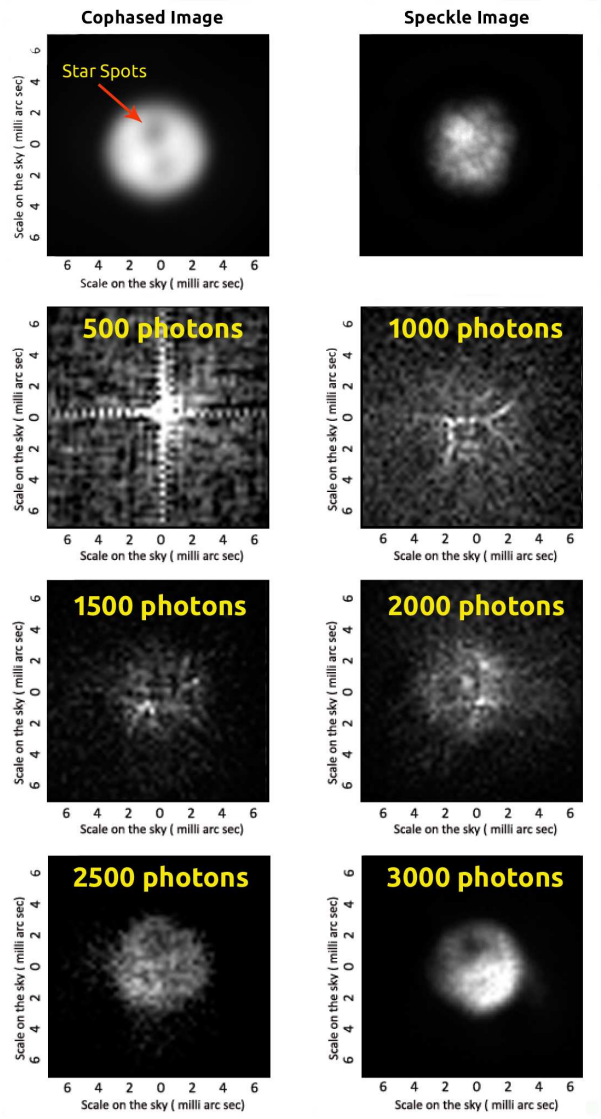

Figure 5.8: Reconstructions of a resolved star with spots at different magnitudes. The aperture used is an array of 50 mirrors with 7 hours of earth roatation aperture synthesis, which increases the spatial frequency coverage. (Top row) The ideal cophased image and speckle image of the resolved star. (Bottom three rows) The reconstructed images using the bispectrum technique with the corrosponding photon counts.

correlation coefficient. The SNR for the binary star was computed as the contrast of the fainter star in the background halo of noise.

$$SNR = \frac{\mu_{star}}{\sigma_{background}} \tag{5.5}$$

where μ_{star} is the mean flux level from the pixel positions corresponding to the star and $\sigma_{background}$ the standard deviation of the average background noise. The average noise was computed in the encircled area in the Figure 5.7. For the star spots the contrast level of one of the spots was used as the measure of SNR. To calculate the SNR, 20 reconstructions were computed at each magnitude photon level. The resulting SNR plotted against the photon levels are shown in Figure 5.9 for both binary star and the resolved spotted star.

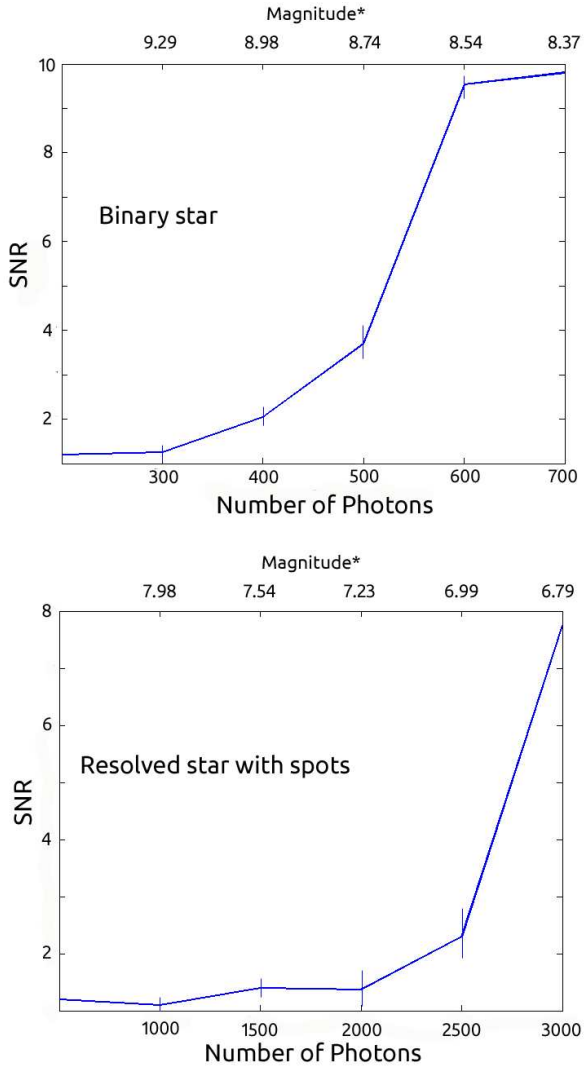

Figure 5.9: The SNR of the reconstructed images plotted against photon count in the speckle images for both Binary star and the resolved star with spots. The magnitude is calculated corresponding to the parameters used in the simulation as listed in table 5.1 and 5.2.

5.4 Simulation of imaging science targets with hypertelescope

As part of the study of imaging simulations for hypertelescope, we have also studied possible numerical simulations of observing certain specific science objects that could be of interest in high resolution. Active Galactic Nuclei (AGN), transiting exo-planets and binary stars could be a few of the major science targets. In this section we present these simulations.

5.4.1 Simulation of imaging Active Galactic Nuclei

We present simulated observations of clumpy dust structures surrounding Active Galactic Nuclei (AGN) using hypertelescopes. Hypertelescopes can achieve direct imaging at sub-milli-arc second resolution. Their theoretical imaging performance calculated and simulated is expected to exceed that of first generation interferometers. Observing AGN's and the dust tori around them could be a major science goal for such hypertelescopes. For our AGN

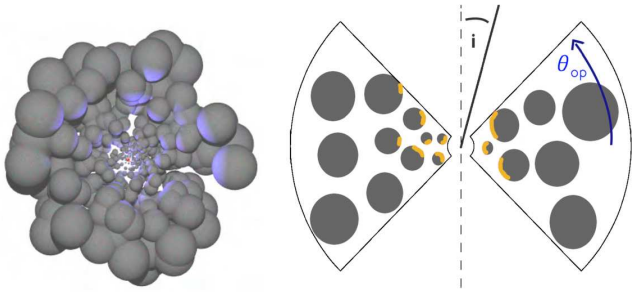

Figure 5.10: A schematic distribution of the dust clouds and AGN core model assumed in Schartmann *et al.* (2008) . (Left) The AGN core is the red dot at the center, while the pale blue regions show which clouds have direct lines of sight to the core and hence are heated. (Right) Clumpy torus model. Yellow regions indicate the directly illuminated surfaces of the clumps. i is the inclination angle, θ is the half opening angle of the torus. (Schartmann *et al.*, 2008)

performance simulations, we used the model of Schartmann *et al.* (2008) and Young *et al.* (2014) (Figure 5.10). In this scenario, the "dust torus", which

in the standard is assumed to be comprised of an assemblage of discrete clouds. i.e., it does not correspond to a smooth continuous distribution of dust. As a result some lines of sight to the more distant dust clouds may be obscured while not the others. The upshot of this is that the hottest dust, can exist both very close to and distant from the nuclear core. This leads to a much clumpier near-IR brightness distribution than a smooth dust torus in the model. We use an AGN model in pole-on and edge-on torus geometry similar to a study by Young *et al.* (2014). We have used the images from 3D radiative transfer code MC3D which gives the temperature and surface brightness distributions of the resulting heated dust distribution. For the AGN simulations, we chose to model both a pole-on and an edge-on model. The central AGN engine was assumed obscured for this edge-on case. For full details of the modeling the reader in encouraged to read Schartmann *et al.* (2008) and references therein. We have used IMAGIN, a simulation package developed by us to simulate hypertelescope observations and the image deconvolution. Atmosphere induced piston errors and additive noise are added to the images from MC3D code. The results of this simulation is shown in Figure 5.11.

5.4.2 Imaging exoplanet transits with Hypertelescope

In 1983 feasibility of formation flying interferometric space arrays were explored by many (Labeyrie et al., 1982a,b, 1984). A major science target for these space arrays was to image planets around nearby stars (exoplanets). Resolving an "exo-Earth" in sufficient detail will require an array size larger than 100 km also with coronographic abilities. Periodic eclipses of exoplanets over the resolved star disk can be observed with hypertelescopes. This is an easier way of imaging exoplanets without the use of coronographic techniques. Jupitar like planets which may eclipse its parent star may be 10 times smaller, thus covering 1 resel if star was resolved over 10 resels. The planet's darkness will be filled by the side lobes of the spread function, but

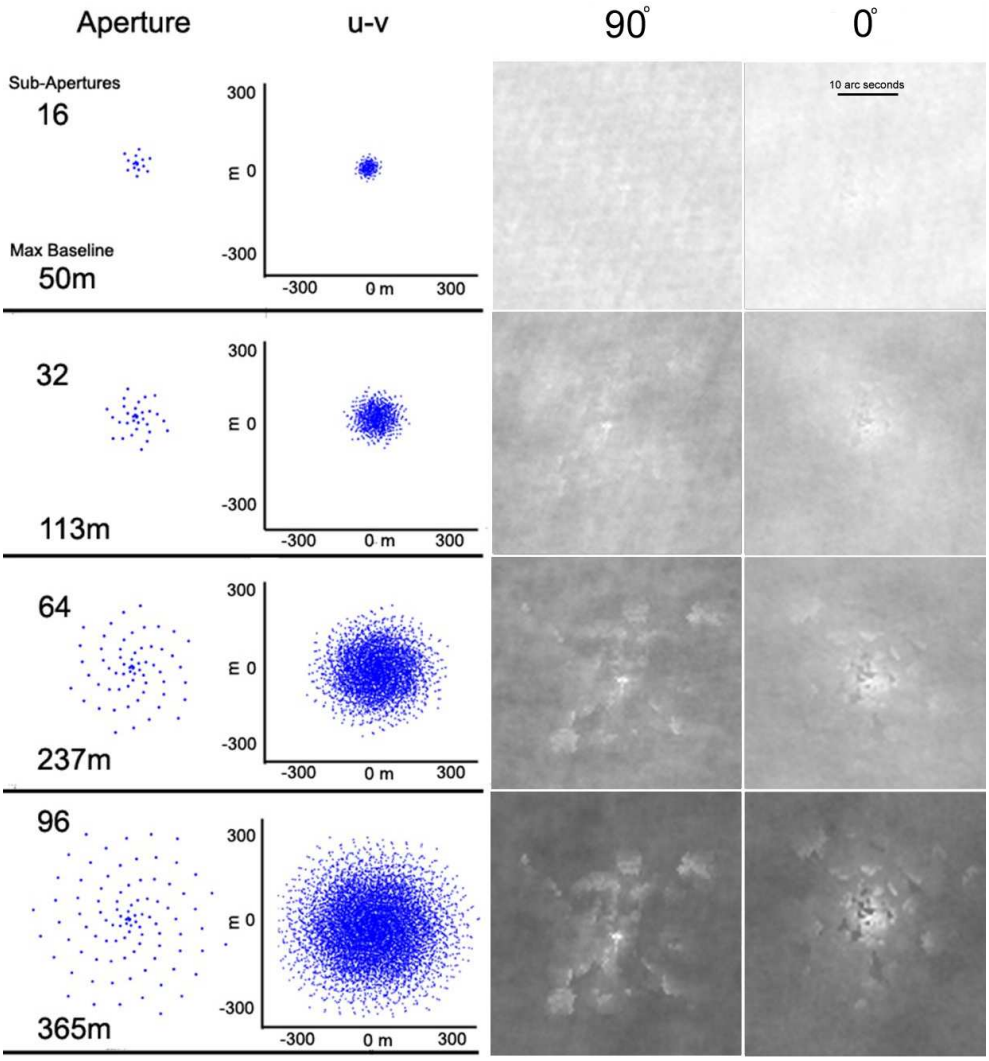

Figure 5.11: The reconstructed images of the dusty torus around the AGN. The aperture used for imaging and the corresponding u-v coverage is also shown. The 3rd column is of edge-on geometry model and 4th column is of the pole on geometry. (Surya et al., 2015)

sufficient contrast still remains to properly resolve it. Observations at several wavelengths will also give planets with information about planets extended atmosphere. Simulated images of exoplanet transits are shown in Figure 5.12 and Figure 5.13.

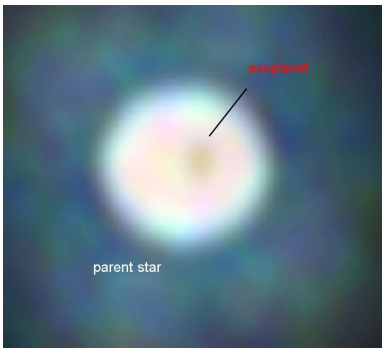

Figure 5.12: Exoplanet transit across a resolved star, as imaged by a 17 mirror cophased diluted Hypertelescope with maximum baseline of 100m. The star disk is 27 resels while the exoplanet is 3 resels in the image. The simulated image is a combination of 3 seperate images at different wavelengths.

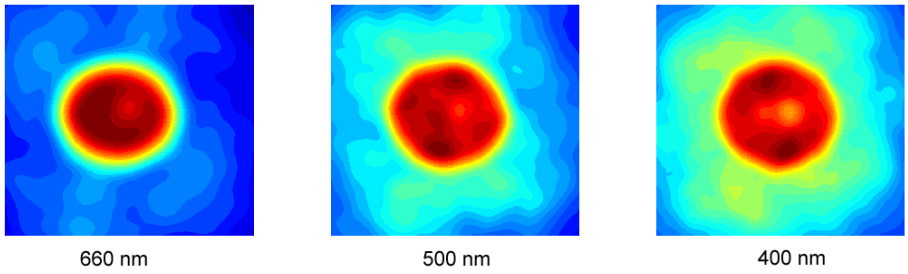

Figure 5.13: Simulated Hypertelescope Image of the Exoplanet Transit in different wavelengths.

5.4.3 Binary Stars and Small Clusters

Binary stars have been always an importent target for speckle interferometric techniques. Classical speckle interferometry itself can be used to gain a significant amount of information regarding binary systems. It can be used to find out the seperations between the binary systems. With the use of speckle masking the Fourier information that was extracted gives a more complete picture of the binary sytem, by giving information about the orientation. Such binary stars will be an importent science target with hypertelescopes. Multi wavelength observations of such targets can give very interesting insights in to these systems. An imaging simulation of observation of binary stars and a sextuple star with hypertelescope are shown in Figure 5.14

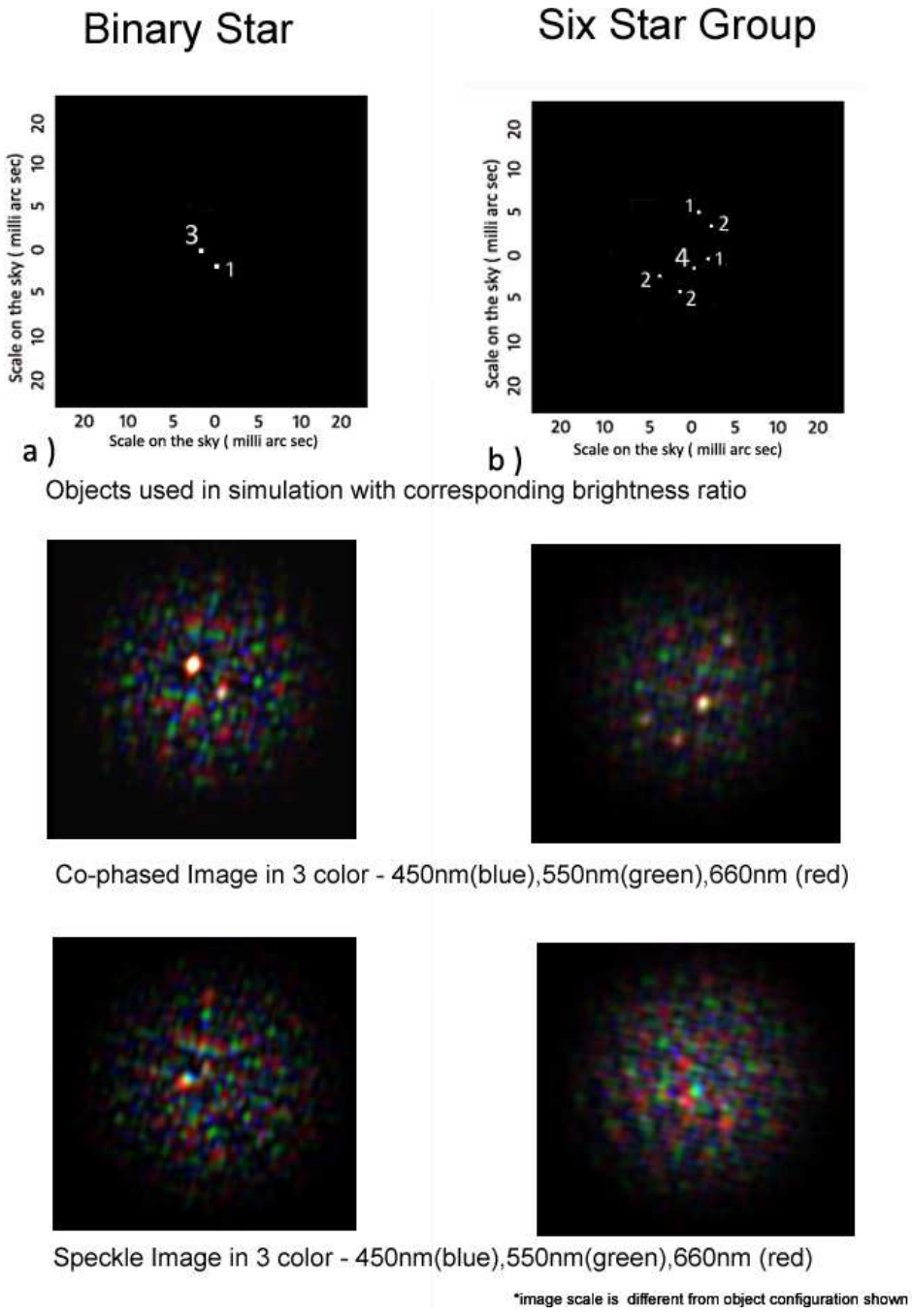

Figure 5.14: Simulated Hypertelescope Images of binary stars and star clusters.

5.5 Conclusions

The simulations have successfully shown that even in the absence of adaptive phasing, hypertelescope systems employing pupil densification can be used for direct imaging using speckle imaging techniques. It is shown that with utilizing the aperture rotation of the diluted array through night, reconstruction quality could be increased substantially. Other ways of changing the aperture pattern during observation may also be considered, and should similarly be expected to improve the imaging performance. Though as with cophased imaging, speckle imaging also is constrained by the field of view limitations in a hypertelescope. The use of speckle imaging for future Earth-based hypertelescopes Labeyrie *et al.* (2012a) can be of interest for faint sources which cannot be phased in the absence of adaptive optics, or because of the absence of a sufficiently bright guide star. With the parameters of hypertelescope used in the simulation we have obtained a good SNR for the speckle technique at a magnitude of 8-9 for a simple binary star and 6-7 for a resolved star with spots. The improvement in limiting magnitude of the technique with different amounts of pupil densification need to be studied further. Also the technique could give better results with deconvolution algorithms and pupil re-dilution as studied by Aime *et al.* (2012). While modified forms of adaptive optics have been proposed specifically for hypertelescopes Martinache (2004); Borkowski *et al.* (2005), it remains unclear at this stage whether suitable forms of a Laser Guide Star can also be operated for such instruments Nuñez *et al.* (2014). If not, Earth-based hypertelescopes will have to use speckle-imaging on faint sources, which should provide useful results, according to our simulation results, although with lesser performance than in phased conditions. For space hypertelescopes, phasing is expected to be much easier Labeyrie *et al.* (2009, 2010). Although the huge sizes considered, 100 km for an Exo-Earth Imager and 100,000 km for a Neutron Star Imager, can make them sensitive to new forms of seeing such as “gravitational seeing”.

Chapter 6

Summary and Future Work

6.1 Introduction

In the field of high resolution tremendous advancements have been made. Interferometric methods have shown great promise and delivered in multiple fronts. The current interferometers are limited by the number of baselines and thus use aperture synthesis to obtain useful results with visibility measurements and closure of phase. Such model based approach has paid dividend in obtaining very useful results. An important step forward in optical interferometry would be to use diluted aperture interferometers to image in high resolution. Such optical interferometers increase the resolution with same amount of light collection area as a single aperture telescope. And the manufacturing and construction cost would be similar to a single aperture even with the large baselines. A major problem that these diluted interferometers could face is to compensate the turbulence related effects from the atmosphere. The adaptive optics technology for these diluted telescopes are still under investigation. Image reconstruction algorithms have contributed in the field of optical interferometry. For single aperture telescopes the reconstruction algorithms based on triple correlation has provided with very fruitful results. In this thesis we have tried to establish and verify use the traditional triple correlation based reconstructions in diluted aperture interferometers, aperture masking and multi speckle long baseline interferometry.

6.2 Summary

We started by giving introduction to the importance of phase and how atmospheric turbulence affects the phase of the wavefronts, creating speckle patterns and destroying our ability to obtain diffraction limited images. Our aim in this thesis have been to develop image reconstruction techniques related to optical interferometers. In this scenario it was important to realistically simulate the affects of atmospheric turbulence. We discuss in detail the model used by us to simulate atmospheric turbulence using the basic principles of Kolmogorov Turbulence model. We also discuss the important aspects of our simulation like, the simulation of earth rotation aperture synthesis, beam combination modes, multispeckles etc. These studies allows us to simulate different modes of optical interferometry with different configurations. In this phase of study we have also analyzed in detail how advantageous the all-in-one beam combination is over the use of pair-wise combination currently used in most interferometers. We layout a study of the signal advantage we obtain at low light levels through all-in-one beam combination in cophased and non-cophased speckle mode.

The image reconstruction technique used in this thesis is the triple correlation based reconstruction. It has great potential since it allows the reconstruction of phase information. The theory of triple correlation is studied and its application to developing a direct bispectrum algorithm is discussed. The algorithm has been used with real speckle images, aperture masking simulations and multispeckle simulations. The software based on the algorithm is able to reconstruct the objects in each of the three scenarios.

A major drawback of the direct bispectrum algorithm has been the computational time and memory requirements. A tomographic algorithm based on radon transform has been developed which significantly reduces the time of processing since the computations are reduced to 1-dimensional signals. We have compared the direct bispectrum and tomographic speckle masking algorithm to find that the TSM algorithm gives similar results at faster time.

A significant part of the study in this thesis is dedicated to hypertelescopes which are diluted aperture optical interferometers which can produce high resolution images. These telescopes use small mirrors setup in arecibo kind of mountain valley with the beams combined in the gondola above. The technique of pupil densification allows them to be useful in imaging fainter stars by reducing energy getting dissipated in to side halo of the PSF. This thesis discusses the principles behind hypertelescope in detail and also lays out the numerical simulations to simulate the images from such a system. Speckle imaging with hypertelescopes, is a new technique that has been developed in this thesis. Development of adaptive optics systems for large diluted telescopes like hypertelescopes will be very challenging. it has been verified by numerical simulations that the use of speckle imaging with hypertelescopes can offer a viable observational method for such systems in the absence of adaptive cophasing.

6.3 Future Prospects

6.3.1 Bispectrum algorithm to work on OIFITS data from long baseline interferometers.

The developed algorithms in the thesis works with direct imaging interferometers. Current interferometers, as discussed in earlier sections, take visibility and closure of phase measurements instead of real images. The image reconstruction algorithms that work with long baseline interferometry data use regularization techniques to infer the object distribution from the measured visibilities and closure of phases. Such techniques that work on VLTI and CHARA data have contributed immensely in the science cirumstellar enviorment around stars (Meilland *et al.*, 2007a,b) and stellar surfaces (Tuthill *et al.*, 1997, 1999). It would be interesting to use regularization based techniques with the direct bispectrum algorithm. This would enable us to work with data from the current interferometers. The format for the data from

long baseline interferometers has already been standardized in to a FITS file format. This format is called OI-FITS. A possible future direction of work with the current algorithm could be enabling it to work with OI-FITS data. Baeysian techniques like simulated annealing, maximum entropy etc could be utilized to make it better.

6.3.2 Laboratory simulations of pupil densification

Optical Interferometers use large arrays with telescopes separated by hundreds of meters and achieves imaging at very high angular resolution. Yet if optical interferometry has to make significant contributions to astronomy it has to demonstrate ability to image fainter stellar objects with higher contrast. However the science capabilities of the current generation of interferometric instruments and the proposed ones are strongly limited by sensitivity and dynamic range of observations. The modern optical interferometers need to employ new technologies in optics and photonics to achieve better sensitivity to observe fainter objects and better dynamic range for high contrast imaging. Pupil remapping techniques like pupil densification (Labeyrie, 1996) have developed as a key technology to improve these characteristics of optical interferometers. Together with coronographic techniques (Ricci *et al.*, 2010), which blocks the direct light from the star to detect nearby objects or structures, it can be used for exo-planet detection, imaging of circumstellar disks and other high dynamic range applications in astronomy. Pupil densification is the scheme of concentrating the diffracted energy in to the central part of the PSF. This increases the ability of the system to detect more fainter sources from the background noise. Modelling these new technologies and characterizing their performance for near infrared optical interferometry will be an interesting future work. Experimental simulations could involve building small prototypes of pupil densification using single mode optical fibres (Patru *et al.*, 2008) or micro lens array (Gillet *et al.*, 2003). Once such prototypes are modeled their characteristics can be studied in detail. Inte-

grated photonics research has already brought very interesting technologies in the field of Optical Interferometry by developing of on-chip pupil remapping techniques (Jovanovic *et al.*, 2012). It still needs to be studied how pupil densification can be implemented through on-chip techniques.

6.3.3 The 57m Hypertelescope in La Moutière

To understand broadly the capabilities and to realize the technological improvements to setup a large diluted hypertelescope a prototype version is under development in Vallon de la Mouti‘ere at the limit of the Parc National du Mercantour (2100-2300m altitude) in the southern Alps. The valley is only accessible during the summers and under challenging circumstances the team led by Prof. Antoine Labeyrie have been tirelessly trying to built a diluted aperture interferometer in the valley. The priliminary baseline being developed is 57 m to be expanded later by adding more mirrors. The discrete

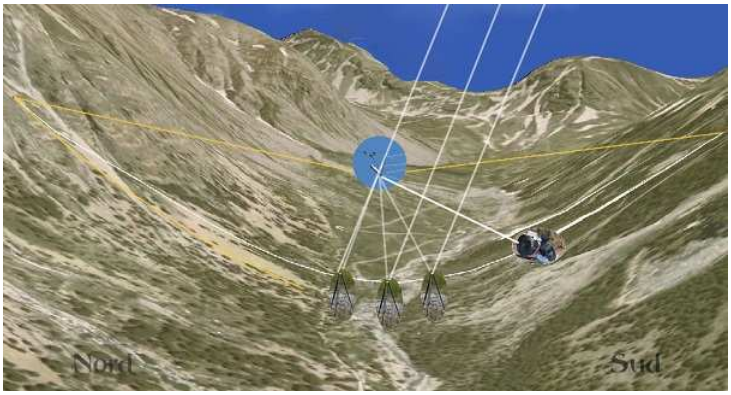

Figure 6.1: The optical scheme planned in the prototype at Moutiere valley. The light from the star is reflected on to the gondola by the mirrors in the valley, and then the image is observed indirectly through a coude setup. (Labeyrie *et al.*, 2012b)

elements of the diluted primary are primarily arranged in spherical locus in the valley. A spherical corrector is used to correct the spherical aberration at the focal gondola which also houses the detector. The focal gondola is hanging 100 m above the valley. Once the initial fringes are obtained, next

step would be to attain observational ability using speckle imaging. The developed algorithms can be used with the developed prototype to obtain some interesting results. Figure 6.1 and Figure 6.2 shows the basic structure of the setup being developed.

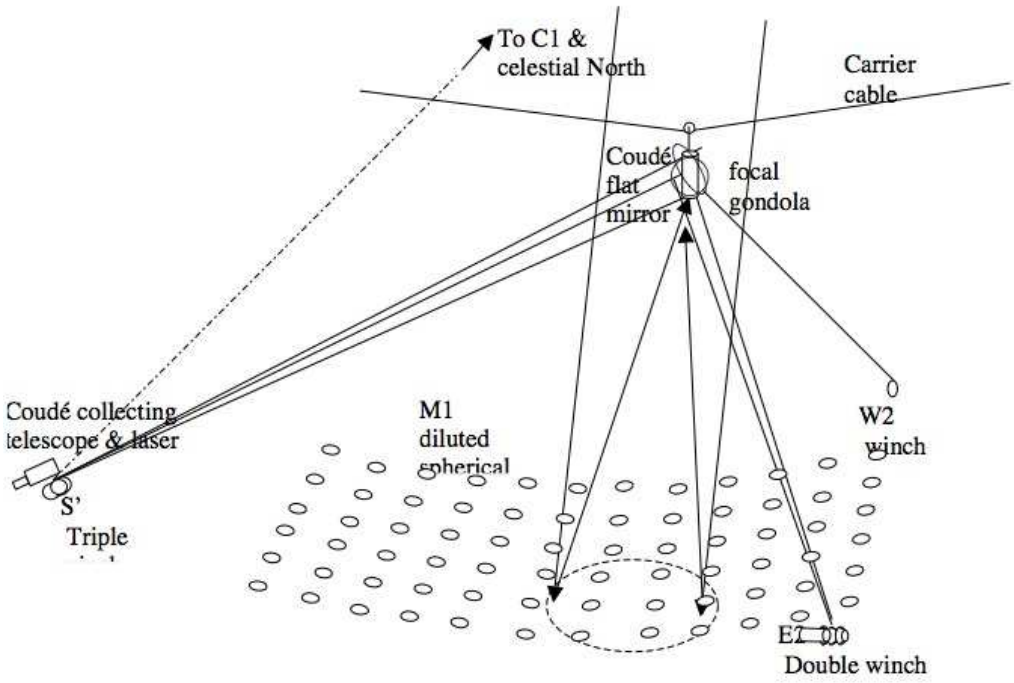

Figure 6.2: Driving system built at Ubaye. The gondola is suspended 100 m above ground at a 800 m meridian traversing cable, via a rolling pulley, with oblique wires defining its x,y,z position. The cables attachment points in the cliffs on both valley sides are approximately aligned with C1, the center of curvature of the primary dilute mirror, so that it can pendulate to allow the East-West motion of the gondola. The angle of its chainette sag at the gondola provides a spring-like lifting force which tensions the driving wires. These are controlled by ground winches, computer driven, located at the East side, the West side and the South side at the polar projection of C1. The motors at all three points, spaced about 200m apart, are synchronized by innovative wireless links. The gondola motion is equatorial and allows a Coude focus to be projected toward the South winch. The power need for the winches is minimized by tensioning the wires with counterweights. All the system use solar energy relayed by batteries during the night. (Labeyrie *et al.*, 2012b)

6.3.4 The Extremely Large Hypertelescope

The development at Vallon de la Moutière will give enough impetus to move towards the development of larger versions which can have baselines upto 1200m. The Arecibo like structure of these interferometers does not require large mount or dome which is a major cost contributer in 30m TMT(Thirty Meter Telescope) and the planned 40m ELT(European Large Telescope). For the same cost, an "Extremely Large Hyper Telescope" (ELHyT) may therefore have a larger collecting area. It may thus in principle reach higher limiting magnitudes, both for seeing-limited and, if equipped with a Laser Guide Star and adaptive phasing, for high-resolution imaging with gain as the size ratio, i.e. about 30 with respect to a 40m ELT. One of the key advantages of such telescopes are that they can be grown progressively like a radio array and also setup with multiple gondolas tracking different sources. Array apodization and coronography can further increase the potential of such arrays by increasing the dynamic range of imaging thus being useful to image exoplanet transits and in resolving stellar chromospheres. Extremely Large HyperTelescope can achieve a large gain in spatial resolution, direct-imaging performance and in interferometric limiting magnitude with Laser Guide Star. This will open broad science niches, including possibly deep field cosmology. Embryonic version can rapidly grow to full size but the design is highly site-dependent and thus an early selection will be needed

6.4 Conclusion

The thesis discusses the development of two image reconstruction algorithms to be used with direct images from optical interferometers. Direct bispectrum algorithm uses a computationally intensive but efficient technique to reconstruct object information from speckle images. Tomographic speckle masking algorithm has been developed to offer a computationally efficient method to reconstruct images from speckle data. Both these algorithms were tested with numerical simulations, real data and experimental simulations. Numeri-

cal simulations of different optical interferometric techniques have been built to understand the possibility of reconstruction using these methods. A part of the thesis concentrates on usability of these algorithms with diluted aperture interferometers which use pupil densification. It is seen from the simulations that the developed algorithms can be used with these diluted interferometers to obtain useful results.

Publications

Refereed Journal Articles

- Speckle Imaging with Hypertelescope
  Arun Surya; Swapan K.Saha; Antoine Labeyrie
  Monthly Notices of Royal Astronomical Society (September 1, 2014) 443 (1): 852-859.

- Computationally efficient method for retrieval of atmospherically distorted astronomical images
  Journal of Optics (December, 2014), Volume 43, Issue 4, pp 317-324.

Refereed Conference Papers

- Concept study of an Extremely Large Hyper Telescope (ELHyT) with 1200m sparse aperture for direct imaging at 100 micro-arcsecond resolution
  Antoine Labeyrie ; Denis Mourard ; Fatme Allouche ; Rijuparna Chakraborthy; Julien Dejonghe ; Arun Surya ; Yves Bresson ; Claude Aime ; David Mary ;Alexis Carlotti
  Proc. SPIE 8445, Optical and Infrared Interferometry III, 844512 (September 12, 2012).

- Construction of a 57m hypertelescope in the Southern Alps
  A Labeyrie ; F. Allouche ; D. Mourard ; F. Bolgar ; R. Chakraborty ; J. Maillot ;N. Palitzyne ; J. R. Poletti ; J.-P. Rochaix ; R. Prud'homme

; A. Rondi ; M. Roussel ; A. Surya

Proc. SPIE 8445, Optical and Infrared Interferometry III, 844511 (September 12, 2012).

Other Conference Papers

- Imaging Exoplanet Transits with Hypertelescopes

  A.Surya , S.K.Saha and A.Labeyrie

  Optical Society of India Symposium XXXVI: International Conference on Contemporary Trends in Optics and Optoelectronics 2011.

- Limiting magnitude of Hypertelescopes

  A.Surya and S.K. Saha

  31st ASI Meeting, ASI Conference Series, 2013, Vol. 9, pp 137.

Bibliography

Ables, J.G.: 1974, Maximum Entropy Spectral Analysis. *Astron. Astrophys. Suppl.* **15**, 383.

Aime, C.: 2008, Imaging with hypertelescopes: a simple modal approach. *Astron. Astrophys.* **483**, 361 – 364.

Aime, C., Lantéri, H., Diet, M., Carlotti, A.: 2012, Strategies for the deconvolution of hypertelescope images. *Astron. Astrophys.* **543**, A42.

Altschuler, D.R.: 2002, The National Astronomy and Ionosphere Center's (NAIC) Arecibo Observatory in Puerto Rico. In: Stanimirovic, S., Altschuler, D., Goldsmith, P., Salter, C. (eds.) *Single-Dish Radio Astronomy: Techniques and Applications*, *Astronomical Society of the Pacific Conference Series* **278**, 1 – 24.

Anderson, J.A.: 1920, Application of Michelson's interferometer method to the measurement of close double stars. *Astrophys. J.* **51**, 263 – 275.

Babcock, H.W.: 1953, The Possibility of Compensating Astronomical Seeing. PASP **65**, 229.

Baldwin, J.E., Haniff, C.A., Mackay, C.D., Warner, P.J.: 1986, Closure phase in high-resolution optical imaging. Nature **320**, 595 – 597.

Baron, F., Cotton, W.D., Lawson, P.R., Ridgway, S.T., Aarnio, A., Monnier, J.D., Hofmann, K.-H., Schertl, D., Weigelt, G., Thiébaut, E., Soulez, F., Mary, D., Millour, F., Vannier, M., Young, J., Elias, N.M., Schmitt, H.R., Rengaswamy, S.: 2012, The 2012 interferometric imaging beauty contest.

In: *Society of Photo-Optical Instrumentation Engineers (SPIE) Conference Series*, *Society of Photo-Optical Instrumentation Engineers (SPIE) Conference Series* **8445**, 1.

Borkowski, V., Labeyrie, A., Martinache, F., Peterson, D.: 2005, Sensitivity of a "dispersed-speckles" piston sensor for multi-aperture interferometers and hypertelescopes. *Astron. Astrophys.* **429**, 747 – 753.

Brillinger, D.R.: 1975, *Time Series: Data Analysis and Theory.*

Buscher, D.F.: 1994, Direct maximum-entropy image reconstruction from the bispectrum. In: Robertson, J.G., Tango, W.J. (eds.) *Very High Angular Resolution Imaging*, *IAU Symposium* **158**, 91.

Chinnappan, V., Saha, S.K., Faseehana: 1991, Intensified CCD camera based remote guiding unit for VBT and observation of speckles with ICCD. *Kodaikanal Observatory Bulletins* **11**, 87 – 92.

Enmark, A., Andersen, T., Owner-Petersen, M., Chakraborty, R., Labeyrie, A.: 2011, Integrated model of the carlina telescope. In: *???* **8336**, 83360J – 83360J-14.

F. Vakili, E. Aristidi, L. Abe, B. Lopez: 2004, Interferometric Remapped Array Nulling. *Astron. Astrophys. Suppl.* **421**(1), 147 – 156. doi:10.1051/0004-6361:20034277.

Fizeau, A.H.: 1867,. *C.R.Acad,Sci. (Paris)* **66**, 934.

FRIED, D.L.: 1966, Optical resolution through a randomly inhomogeneous medium for very long and very short exposures. *J. Opt. Soc. Am.* **56**(10), 1372 – 1379.

Frieden, B.R.: 1972, Restoring with maximum likelihood and maximum entropy. *J. Opt. Soc. Am.* **62**(4), 511 – 518.

García-Lorenzo, B., Eff-Darwich, A., Fuensalida, J.J., Castro-Almazán, J.: 2011, Adaptive optics parameters connection to wind speed at the Teide Observatory: corrigendum. *Mon. Not. R. Astron. Soc.* **414**, 801 – 809.

Gentry, B.M., Chen, H., Li, S.X., Mathur, S., Dobler, J., Hasselbrack, W., Comer, J.: 2004, Wind Profiles Obtained with a Molecular Direct Detection Doppler LIDAR during IHOP_2002. In: Pappalardo, G., Amodeo, A. (eds.) *22nd Internation Laser Radar Conference (ILRC 2004)*, *ESA Special Publication* **561**, 731.

Gezari, D.Y., Labeyrie, A., Stachnik, R.V.: 1972, Speckle Interferometry: Diffraction-Limited Measurements of Nine Stars with the 200-INCH Telescope. *Astrophys. J. Lett.* **173**, L1.

Gillet, S., Riaud, P., Lardière, O., Dejonghe, J., Schmitt, J., Arnold, L., Boccaletti, A., Horville, D., Labeyrie, A.: 2003, Imaging capabilities of hypertelescopes with a pair of micro-lens arrays. *Astron. Astrophys.* **400**, 393 – 396.

Glindemann, A.: 2011, *Principles of Stellar Interferometry.*

Goodman, J.W.: 2005, *Introduction to Fourier optics.*

Hanbury Brown, R.: 1956, A Test of a New Type of Stellar Interferometer on Sirius. Nature **178**, 1046 – 1048.

Hanbury Brown, R., Davis, J., Allen, L.R.: 1974, The angular diameters of 32 stars. *Mon. Not. R. Astron. Soc.* **167**, 121 – 136.

Haniff, C.A., Mackay, C.D., Titterington, D.J., Sivia, D., Baldwin, J.E.: 1987, The first images from optical aperture synthesis. Nature **328**, 694 – 696.

Hofmann, K.-H., Weigelt, G.: 1993, Iterative image reconstruction from the bispectrum. *Astron. Astrophys.* **278**, 328 – 339.

Högbom, J.A.: 1974, Aperture Synthesis with a Non-Regular Distribution of Interferometer Baselines. *Astron. Astrophys. Suppl.* **15**, 417.

Jennison, R.C.: 1958, A phase sensitive interferometer technique for the measurement of the Fourier transforms of spatial brightness distributions of small angular extent. *Mon. Not. R. Astron. Soc.* **118**, 276.

Jovanovic, N., Tuthill, P.G., Norris, B., Gross, S., Stewart, P., Charles, N., Lacour, S., Ams, M., Lawrence, J.S., Lehmann, A., Niel, C., Robertson, J.G., Marshall, G.D., Ireland, M., Fuerbach, A., Withford, M.J.: 2012, Starlight demonstration of the Dragonfly instrument: an integrated photonic pupil-remapping interferometer for high-contrast imaging. *Mon. Not. R. Astron. Soc.* **427**, 806 – 815.

Khintchine, A.: 1934, Korrelationstheorie der stationären stochastischen prozesse. *Mathematische Annalen* **109**(1), 604 – 615.

Knox, K.T., Thompson, B.J.: 1974, Recovery of images from atmospherically degraded short-exposure photographs. *Astrophys. J. Lett* **193**, L45 – L48.

Kolmogorov, A.: 1941, The Local Structure of Turbulence in Incompressible Viscous Fluid for Very Large Reynolds' Numbers. *Akademiia Nauk SSSR Doklady* **30**, 301 – 305.

Kolmogorov, A.N.: 1991, Dissipation of energy in the locally isotropic turbulence. **434**(1890), 15 – 17.

Labeyrie, A.: 1970, Attainment of Diffraction Limited Resolution in Large Telescopes by Fourier Analysing Speckle Patterns in Star Images. *Astron. Astrophys.* **6**, 85.

Labeyrie, A.: 1975, Interference fringes obtained on VEGA with two optical telescopes. *Astrophys. J. Lett* **196**, L71 – L75.

Labeyrie, A.: 1978, Stellar interferometry methods. ARA&A **16**, 77 – 102.

Labeyrie, A.: 1982, Detection of extra-solar planets. In: Brahic, A. (ed.) *Formation of Planetary Systems*, 883.

Labeyrie, A.: 1996, Resolved imaging of extra-solar planets with future 10-100km optical interferometric arrays. *Astron. Astrophys. Suppl.* **118**, 517 – 524.

Labeyrie, A.: 2007, Comparison of ELTs, interferometers and hypertelescopes for deep field imaging and coronagraphy. *Comptes Rendus Physique* **8**, 426 – 437.

Labeyrie, A., Schumacher, G., Savaria, E.: 1982a, FLUTE or TRIO - Different approaches to optical arrays in space. *Advances in Space Research* **2**, 11 – 22.

Labeyrie, A., Schumacher, G., Dugue, M., Thom, C..

Labeyrie, A., Bonneau, D., Stachnik, R.V., Gezari, D.Y.: 1974, Speckle Interferometry. III. High-Resolution Measurements of Twelve Close Binary Systems. *Astrophys. J. Lett* **194**, L147.

Labeyrie, A., Kibblewhite, J., de Graauw, T., Noordam, J., Weigelt, G., Roussel, H.: 1982b, Coherent arrays of separate optical telescopes in space project TRIO. In: Biraud, F. (ed.) *Very long baseline interferometry techniques*, 477 – 488.

Labeyrie, A., Authier, B., Boit, J.L., de Graauw, T., Kibblewhite, E., Koechlin, L., Rabout, P., Weigelt, G.: 1984, PM. 08 Trio: A Kilometric Optical Array Controlled by Solar Sails. In: *Bulletin of the American Astronomical Society*, *Bulletin of the American Astronomical Society* **16**, 828.

Labeyrie, A., Le Coroller, H., Dejonghe, J., Lardière, O., Aime, C., Dohlen, K., Mourard, D., Lyon, R., Carpenter, K.G.: 2009, Luciola hypertelescope space observatory: versatile, upgradable high-resolution imaging, from stars to deep-field cosmology. *Experimental Astronomy* **23**, 463 – 490.

Labeyrie, A., Coroller, H.L., Residori, S., Bortolozzo, U., Huignard, J., Riaud, P.: 2010, Resolved Imaging of Extra-Solar Photosynthesis Patches with a

"Laser Driven Hypertelescope Flotilla". In: Coudé du Foresto, V., Gelino, D.M., Ribas, I. (eds.) *Pathways Towards Habitable Planets*, *Astronomical Society of the Pacific Conference Series* **430**, 239.

Labeyrie, A., Mourard, D., Allouche, F., Chakraborthy, R., Dejonghe, J., Surya, A., Bresson, Y., Aime, C., Mary, D., Carlotti, A.: 2012a, Concept study of an Extremely Large Hyper Telescope (ELHyT) with 1200m sparse aperture for direct imaging at 100 micro-arcsecond resolution. In: *Society of Photo-Optical Instrumentation Engineers (SPIE) Conference Series*, *Society of Photo-Optical Instrumentation Engineers (SPIE) Conference Series* **8445**.

Labeyrie, A., Allouche, F., Mourard, D., Bolgar, F., Chakraborty, R., Maillot, J., Palitzyne, N., Poletti, J.R., Rochaix, J.-P., Prud'homme, R., Rondi, A., Roussel, M., Surya, A.: 2012b, Construction of a 57m hypertelescope in the Southern Alps. In: *Society of Photo-Optical Instrumentation Engineers (SPIE) Conference Series*, *Society of Photo-Optical Instrumentation Engineers (SPIE) Conference Series* **8445**.

Lane, R.G., Glindemann, A., Dainty, J.C.: 1992, Simulation of a Kolmogorov phase screen. *Waves in Random Media* **2**, 209 – 224.

Lardière, O., Martinache, F., Patru, F.: 2007, Direct imaging with highly diluted apertures - I. Field-of-view limitations. *Mon. Not. R. Astron. Soc.* **375**, 977 – 988.

Lawson, P.R., Cotton, W.D., Hummel, C.A., Monnier, J.D., Zhao, M., Young, J.S., Thorsteinsson, H., Meimon, S.C., Mugnier, L.M., Le Besnerais, G., Thiebaut, E.M., Tuthill, P.G.: 2004, An interferometry imaging beauty contest. In: Traub, W.A. (ed.) *New Frontiers in Stellar Interferometry*, *Society of Photo-Optical Instrumentation Engineers (SPIE) Conference Series* **5491**, 886.

Le Coroller, H., Dejonghe, J., Arpesella, C., Vernet, D., Labeyrie, A.: 2004, Tests with a Carlina-type hypertelescope prototype. I. Demonstration of

star tracking and fringe acquisition with a balloon-suspended focal camera. *Astron. Astrophys.* **426**, 721 – 728.

Le Coroller, H., Dejonghe, J., Regal, X., Sottile, R., Mourard, D., Ricci, D., Lardiere, O., Le Vansuu, A., Boer, M., De Becker, M., Clausse, J.-M., Guillaume, C., Meunier, J.P.: 2012a, Tests with a Carlina-type diluted telescope. Primary coherencing. *Astron. Astrophys.* **539**, A59.

Le Coroller, H., Dejonghe, J., Regal, X., Sottile, R., Mourard, D., Ricci, D., Lardiere, O., Le Vansuu, A., Boer, M., De Becker, M., Clausse, J.-M., Guillaume, C., Meunier, J.P.: 2012b, Tests with a Carlina-type diluted telescope. Primary coherencing. *Astron. Astrophys.* **539**, A59.

Le Coroller, H., Dejonghe, J., Hespeels, F., Arnold, L., Andersen, T., Deram, P., Ricci, D., Berio, P., Blazit, A., Clausse, J.-M., Guillaume, C., Meunier, J.P., Regal, X., Sottile, R.: 2015, The Carlina-type diluted telescope. Stellar fringes on Deneb. *Astron. Astrophys.* **573**, A117.

Lohmann, A.W., Weigelt, G., Wirnitzer, B.: 1983, Speckle masking in astronomy - Triple correlation theory and applications. Appl. Opt. **22**, 4028 – 4037.

Lohmann, A.W., Wirnitzer, B.: 1984, Triple correlations. *Proceedings of the IEEE* **72**(7), 889 – 901.

Martinache, F.: 2004, Global wavefront sensing for interferometers and mosaic telescopes: the dispersed speckles principle. *Journal of Optics A: Pure and Applied Optics* **6**, 216 – 220.

Meilland, A., Millour, F., Stee, P., Domiciano de Souza, A., Petrov, R.G., Mourard, D., Jankov, S., Robbe-Dubois, S., Spang, A., Aristidi, E., Antonelli, P., Beckmann, U., Bresson, Y., Chelli, A., Dugué, M., Duvert, G., Gennari, S., Glück, L., Kern, P., Lagarde, S., Le Coarer, E., Lisi, F., Malbet, F., Perraut, K., Puget, P., Rantakyrö, F., Roussel, A., Tatulli, E., Weigelt, G., Zins, G., Accardo, M., Acke, B., Agabi, K., Altariba, E.,

Arezki, B., Baffa, C., Behrend, J., Blöcker, T., Bonhomme, S., Busoni, S., Cassaing, F., Clausse, J.-M., Colin, J., Connot, C., Delboulbé, A., Driebe, T., Feautrier, P., Ferruzzi, D., Forveille, T., Fossat, E., Foy, R., Fraix-Burnet, D., Gallardo, A., Giani, E., Gil, C., Glentzlin, A., Heiden, M., Heininger, M., Hernandez Utrera, O., Hofmann, K.-H., Kamm, D., Kiekebusch, M., Kraus, S., Le Contel, D., Le Contel, J.-M., Lesourd, T., Lopez, B., Lopez, M., Magnard, Y., Marconi, A., Mars, G., Martinot-Lagarde, G., Mathias, P., Mège, P., Monin, J.-L., Mouillet, D., Nussbaum, E., Ohnaka, K., Pacheco, J., Perrier, C., Rabbia, Y., Rebattu, S., Reynaud, F., Richichi, A., Robini, A., Sacchettini, M., Schertl, D., Schöller, M., Solscheid, W., Stefanini, P., Tallon, M., Tallon-Bosc, I., Tasso, D., Testi, L., Vakili, F., von der Lühe, O., Valtier, J.-C., Vannier, M., Ventura, N.: 2007a, An asymmetry detected in the disk of ¡ASTROBJ¿κ Canis Majoris¡/ASTROBJ¿ with AMBER/VLTI. *Astron. Astrophys.* **464**, 73 – 79.

Meilland, A., Stee, P., Vannier, M., Millour, F., Domiciano de Souza, A., Malbet, F., Martayan, C., Paresce, F., Petrov, R.G., Richichi, A., Spang, A.: 2007b, First direct detection of a Keplerian rotating disk around the Be star α Arae using AMBER/VLTI. *Astron. Astrophys.* **464**, 59 – 71.

Meimon, S., Mugnier, L.M., Besnerais, G.L.: 2009, Self-calibration approach for optical long-baseline interferometry imaging. *J. Opt. Soc. Am. A* **26**(1), 108 – 120.

Menut, J.-L., Valat, B., Lopez, B., Schmider, F.-X., Vakili, F., Jankov, S., Bresson, Y., Lagarde, S., Petrov, R.G., Domiciano, A., Mosoni, L., Danchi, W.C.: 2008, An Alternative Approach for Imaging in Optical Interferometry. *Astrophys. J.* **686**, 1514 – 1522.

Michelson, A.A., Pease, F.G.: 1921, Measurement of the diameter of alpha Orionis with the interferometer. *Astrophys. J.* **53**, 249 – 259.

Michelson, A.A.: 1890, On the application of interference methods to astronomical measurements. *Phil.Mag* **30**, 1 – 21.

Michelson, A.A.: 1891, Measurement of Jupiter's satellites by interference. *Nature* **45**, 160 – 161.

Nakajima, T.: 2001, Sensitivity of a Ground-based Infrared Interferometer for Aperture Synthesis Imaging. PASP **113**, 1289 – 1299.

Nuñez, P.D., Labeyrie, A., Riaud, P.: 2014, Towards laser guide stars for multi-aperture interferometry: an application to the hypertelescope. *Mon. Not. R. Astron. Soc.* **439**, 1787 – 1795.

Oppenheim, A.V., Lim, J.S.: 1981, The importance of phase in signals. *Proceedings of the IEEE* **69**(5), 529 – 541.

Parenti, R.R., Sasiela, R.J.: 1994, Laser-guide-star systems for astronomical applications. *J. Opt. Soc. Am. A* **11**(1), 288 – 309.

Patru, F., Mourard, D., Clausse, J.-M., Delage, L., Reynaud, F., Dubreuil, M., Bonneau, D., Bosio, S., Bresson, Y., Hugues, Y., Lardière, O., Roussel, A.: 2008, First results from a laboratory hypertelescope using single-mode fibers. *Astron. Astrophys.* **477**, 345 – 352.

Patru, F., Tarmoul, N., Mourard, D., Lardière, O.: 2009, Direct imaging with highly diluted apertures - II. Properties of the point spread function of a hypertelescope. *Mon. Not. R. Astron. Soc.* **395**, 2363 – 2372.

Pease, F.G.: 1931,. *Ergebnisse der Exakten Naturwissenschaften* **10**, 84.

Pedretti, E., Labeyrie, A., Arnold, L., Thureau, N., Lardiere, O., Boccaletti, A., Riaud, P.: 2000, First images on the sky from a hyper telescope. *Astron. Astrophys. Suppl.* **147**, 285 – 290.

Ponsonby, J.E.B.: 1973, An entropy measure for partially polarized radiation and itsapplication to estimating radio sky polarization distributions from incomplete4aperture synthesis' data by the maximum entropy method. *Mon. Not. R. Astron. Soc.* **163**, 369.

Prasad, S., Kulkarni, S.R.: 1989, Noise in optical synthesis Images. Pt. 1. Ideal Michelson interferometer. *Journal of the Optical Society of America A* **6**, 1702 – 1714.

Radon, J.: 1986, On the determination of functions from their integral values along certain manifolds. *Medical Imaging, IEEE Transactions on* **5**(4), 170 – 176.

Reinheimer, T., Hofmann, K.-H., Weigelt, G.: 1993, Interferometric imaging with arrays of large optical telescopes in the multi-speckle mode. *Astron. Astrophys.* **279**, 322 – 334.

Reinheimer, T., Hofmann, K.-H., Scholler, M., Weigelt, G.: 1997, Speckle masking interferometry with the Large Binocular Telescope. *Astron. Astrophys. Suppl.* **121**, 191 – 199.

Ricci, D., Le Coroller, H., Labeyrie, A., Piron, P.: 2010, Simulations of coronagraphy with a dynamic hologram for the direct detection of exo-planets. In: *Society of Photo-Optical Instrumentation Engineers (SPIE) Conference Series*, *Society of Photo-Optical Instrumentation Engineers (SPIE) Conference Series* **7731**, 4.

Roddier, F.: 1979, The effects of atmospheric turbulence on the formation of visible and infrared images. *Journal of Optics* **10**(6), 299.

Roddier, F.: 1980, New trends in stellar speckle interferometry. In: *???* **0243**, 83 – 87.

Roddier, F.: 1981, Atmospheric limitations to high angular resolution imaging. In: Ulrich, M.H., Kjaer, K. (eds.) *Scientific Importance of High Angular Resolution at Infrared and Optical Wavelengths*, 5 – 22.

Roddier, F.: 1986, Triple correlation as a phase closure technique. *Optics Communications* **60**, 145 – 148.

Roddier, F.: 1987, Redundant versus nonredundant beam recombination in an aperture synthesis with coherent optical arrays. *Journal of the Optical Society of America A* **4**, 1396 – 1401.

Roddier, F., Lena, P.: 1984a, Long-baseline Michelson interferometry with large ground-based telescopes operating at optical wavelengths. I - General formalism: Interferometry at visible wavelengths. *Journal of Optics* **15**, 171 – 182.

Roddier, F., Lena, P.: 1984b, Long-baseline Michelson interferometry with large ground-based telescopes operating at optical wavelengths. II - Interferometry at infrared wavelengths. *Journal of Optics* **15**, 363 – 374.

Roddier, F., Ridgway, S.T.: 1999, Filling Factor and Signal-to-Noise Ratios in Optical Interferometric Arrays. PASP **111**, 990 – 996.

Roddier, F., Gilli, J.M., Lund, G.: 1982a, On the origin of speckle boiling and its effects in stellar speckle interferometry. *Journal of Optics* **13**(5), 263.

Roddier, F., Gilli, J.M., Vernin, J.: 1982b, On the isoplanatic patch size in stellar speckle interferometry. *Journal of Optics* **13**(2), 63.

Roddier, F.: 1986, Pupil plane versus image plane in michelson stellar interferometry. *J. Opt. Soc. Am. A* **3**(12), 2160 – 2166.

Roopashree, M.B., Vyas, A., Raghavendra Prasad, B.: 2010, Multilayered temporally evolving phase screens based on statistical interpolation. In: *Society of Photo-Optical Instrumentation Engineers (SPIE) Conference Series*, *Society of Photo-Optical Instrumentation Engineers (SPIE) Conference Series* **7736**, 3.

Ryle, M., Vonberg, D.D.: 1946, Solar Radiation on 175 Mc./s. Nature **158**, 339 – 340.

Saha, S.K.: 1999, Speckle interferometry. *Indian Journal of Physics Section B* **73**, 553 – 577.

Saha, S.K.: 2002, Modern optical astronomy: technology and impact of interferometry. *Reviews of Modern Physics* **74**, 551 – 600.

Saha, S.K.: 2011, *Aperture Synthesis*.

Saha, S.K.: 2015, *High Resolution Imaging: Detectors and Applications*.

Saha, S.K., Chinnappan, V.: 1999, Night time variation of Fried's parameter at VBT, Kavalur. *Bulletin of the Astronomical Society of India* **27**, 327.

Saha, S.K., Venkatakrishnan, P.: 1997, Blind iterative deconvolution of binary star images. *Bulletin of the Astronomical Society of India* **25**, 329.

Saha, S.K., Jayarajan, A.P., Sudheendra, G., Chandra, A.U.: 1997, Performance of a speckle interferometer. *Bulletin of the Astronomical Society of India* **25**, 379.

Saha, S.K., Sudheendra, G., Chandra, A.U., Chinnappan, V.: 1999, Development of a Speckle Interferometer and the Measurement of Fried's Parameter (ro) at the Telescope Site. *Experimental Astronomy* **9**, 39 – 49.

Saha, S.K.: 2007, *Diffraction-Limited Imaging with Large and Moderate Telescopes*.

Schartmann, M., Meisenheimer, K., Camenzind, M., Wolf, S., Tristram, K.R.W., Henning, T.: 2008, Three-dimensional radiative transfer models of clumpy tori in Seyfert galaxies. *Astron. Astrophys.* **482**, 67 – 80.

Schwartzschild, K.: 1891,. *Astr. Nachrichten* **139**, 3335.

Sridharan, R.: 2000, Techniques for achieving higher spatial resolution. PhD thesis, Indian Institute of Astrophysics.

Stéphan, M.: 1874,. *Comptes Rendus* **78**, 1008.

Surya, A., Saha, S.K., Labeyrie, A.: 2014, Speckle imaging with hypertelescopes. *Mon. Not. R. Astron. Soc.* **443**, 852 – 859.

Surya, A., Saha, S.: 2014, Computationally efficient method for retrieval of atmospherically distorted astronomical images. *Journal of Optics*, 1 – 8.

Thiébaut, E.: 2008, Mira: an effective imaging algorithm for optical interferometry.

Thompson, A.R., Moran, J.M., Swenson, G.W. Jr.: 2001, *Interferometry and Synthesis in Radio Astronomy, 2nd Edition.*

Tuthill, P.G., Haniff, C.A., Baldwin, J.E.: 1997, Hotspots on late-type supergiants. *Mon. Not. R. Astron. Soc.* **285**, 529 – 539.

Tuthill, P.G., Haniff, C.A., Baldwin, J.E.: 1999, Surface imaging of long-period variable stars. *Mon. Not. R. Astron. Soc.* **306**, 353 – 360.

Van Cittert, P.H.: 1934, Die wahrscheinliche schwingungsverteilung in einer von einer lichtquelle direkt oder mittels einer linse beleuchteten ebene. *Physica* **1**(1–6), 201 – 210.

Weigelt, G.P.: 1977, Modified astronomical speckle interferometry 'speckle masking'. *Optics Communications* **21**, 55 – 59.

Wiener, N.: 1930, Generalized harmonic analysis. *Acta Mathematica* **55**(1), 117 – 258.

Young, J.S., Creech-Eakman, M.J., Haniff, C.A., Buscher, D.F., Schartmann, M., Chiavassa, A., Elvis, M.: 2014, Simulated MROI Imaging of AGN Dust Tori and Stellar Surfaces. In: Creech-Eakman, M.J., Guzik, J.A., Stencel, R.E. (eds.) *Resolving The Future Of Astronomy With Long-Baseline Interferometry, Astronomical Society of the Pacific Conference Series* **487**, 289.

Zernike, F.: 1938, The concept of degree of coherence and its application to optical problems. *Physica* **5**(8), 785 – 795.